Title
Actin filaments and networks under force: A computational study

Author
Wang, Evan Bo

Publication Date
2014

Peer reviewed|Thesis/dissertation

Actin filaments and networks under force: A computational study

by

Evan Bo Wang

A dissertation submitted in partial satisfaction of the
requirements for the degree of
Doctor of Philosophy

in

Chemistry

in the

Graduate Division

of the

University of California, Berkeley

Committee in charge:

Professor Phillip Geissler, Chair
Professor Berend Smit
Professor Daniel Fletcher

Spring 2014

Actin filaments and networks under force: A computational study

Abstract

Actin filaments and networks under force: A computational study

by

Evan Bo Wang

Doctor of Philosophy in Chemistry

University of California, Berkeley

Professor Phillip Geissler, Chair

Rich understanding of a complex system can often emerge from simple but carefully constructed models. With an appropriate model, we can ask questions about how tuning the parameters of the model or modifying the constraints of the system changes the system behavior. My research involves applying such an approach to actin, an essential biopolymer in the cell. In this work, we explore how forces affect actin at the filament and network length scales.

In the first part, we investigate how different forces modulate the interaction between actin filaments and actin-binding proteins. One such protein complex, Arp2/3, can cause filaments to form branches. Experiments indicate that branches preferentially form on the convex side of bent filaments. Using a coarse-grained model discretized at the monomer pair level, we show that binding is dependent upon a high local curvature fluctuation of the filament. The results indicate that actin can sense and respond to mechanical environmental cues to regulate the binding of Arp2/3. We further believe such a picture can serve as a useful framework for studying the effects of force on the binding and function of other proteins. In a follow-up project, we derive analytical expressions for the nanoscale curvature distribution of a worm-like chain and membrane as a function of applied tension. These expressions can be used to understand the force dependence of protein binding on actin filaments and membranes within a biological context.

In the second part, we focus on actin network elasticity. Specifically, we explore how actin networks respond to large external forces. However, the theoretical toolkit for such a task is incomplete. First we develop a constant-stress framework to apply large forces on soft but strongly nonlinear materials. Additionally, we create a toy model of a soft elastic solid with a nonlinear elastic response on which we test our constant-stress method. Finally, we utilize the constant-stress method and a coarse-grained model for short, semiflexible chains to explore actin network elasticity under compression. We consistently observe stress softening under compression, which we analyze from a single filament perspective and using normal mode analysis.

For my parents

Contents

List of Figures

List of Symbols and Abbreviations

κ	local curvature
κ_0	macroscopic curvature
κ_{th}	threshold curvature
L	contour length
l_p	persistence length
Δs	discretization length
$\gamma_{network}$	network strain
ω	angular frequency

ABP	actin binding proteins
ADF	actin depolymerizing factor
ADP	adenosine monophosphate
AFM	atomic force microscope
ANCOVA	analysis of covariance
ANOVA	analysis of variance
Arp2/3	actin related proteins 2 and 3
ARPC	actin related protein complex
ATP	adenosine triphosphate
BSA	bovine serum albumin
CI	confidence interval
F-actin	filamentous-actin
G-actin	globular-actin
GTP	guanosine triphosphate
NPF	nucleation-promoting factor
SEM	standard error of the mean
WLC	worm-like chain

Acknowledgments

First of all, I would like to thank my Ph.D. advisor, Professor Phillip Geissler, for his invaluable guidance and support throughout my graduate career. His probing questions and scientific insights shaped my graduate research and how I approach scientific problems. His love for science and teaching was a continual inspiration for me as a graduate researcher and instructor.

I am very fortunate to have many close experimental and theoretical collaborators in my work. In particular, I would like to thank Viviana Risca and Julian Weichsel for countless hours of brainstorming and discussion. I benefited tremendously from their experience, knowledge, and friendship. I also thank Professor Daniel Fletcher for his valuable inputs in every one of my projects. His experience and expertise has undoubtedly helped to steer my research in the right direction.

The friendships I have made while being at Berkeley have been a constant source of fun, advice, and balance in my life. I relish going into the city, exploring new restaurants, watching sports, and numerous lunches with Dan Goldman, Claudia Avalos, Anthony Fu, Terry Chang, Maya Sen, Pim Dangkulwanich, and others.

My undergraduate advisor Professor Carol Parish has remained a close friend over the years, continually giving me advice and encouragement on my studies. My decision to pursue theory and computation in my graduate studies stemmed from my wonderful experiences in her research lab.

During my time here, I have met numerous people who have generously shared their knowledge and scientific experience with me. These discussions have aided my research profoundly, including a much deeper understanding of experimental procedures and result. In particular, I thank Dave Richmond, Peter Bieling, Michael Vahey, Scott Hansen, Tai-De Li, Matt Bakalar, and Pamela Jreij.

I sincerely thank everyone in the Geissler lab for their support and friendship, including Carl Rogers, Anna Schneider, Chris Ryan, Sucheol Shin, Michael Grunwald, Todd Gingrich, Patrick Schaffer, Laura Armstrong, Julian Weichsel, Suri Vaikuntanathan, John Haberstroh, and Katie Klymko. David Sivak was incredibly patient in answering many of my questions. Lisa Littlejohn has been a constant source of help and kindness, allowing me to focus on my research.

I would like to thank my dissertation committee members, Professors Berend Smit and Daniel Fletcher, for their valuable time and advice.

I have been lucky to be supported by the National Defense Science & Engineering Graduate (NDSEG) Fellowship and Lawrence Berkeley National Laboratory during my studies.

Finally, I owe a deep debt of gratitude to my parents Gary Wang and Jenny Yuan. The values they instilled in me and their unwavering love and support throughout my life are behind every choice I make. To say that I could not have made it this far without them is a huge understatement.

Chapter 1

Introduction

Actin is an ubiquitous and highly conserved protein in cells, playing central roles in a wide variety of cellular function such as cell motility, shape modification, and the transportation of cellular cargo. These diverse roles reveal a very complex and intricate piece of molecular machinery whose structure and properties are highly sensitive to its surrounding conditions and environmental cues. In order to perform its various roles, actin interacts closely with a large number of helper proteins.

Actin was first discovered in 1942 by biochemists Szent-Györgyi and Straub when they demonstrated that, in the presence of ATP, myosin and actin produced muscle contraction [120, 117]. Soon after the initial discovery, Schaub showed that actin exists in both monomeric form (globular actin or G-actin) and polymeric form (filamentous actin or F-actin) [118].

Because of actin's complex behavior, disparate roles, and wide range of properties and interactions across different length scales, it is inevitable that a multitude of tools are necessary to piece together even a small part of the actin puzzle. In this work, we develop and apply various theoretical models and methods, aided by experimental evidence, to understand the biophysical and mechanical properties of actin at the single filament and network levels.

1.1 Monomeric and polymeric actin structure

Actin is one of the most abundant proteins in eukaryotic cells, comprising 10% of the total protein content in muscle cells and 1-5% in non-muscle cells [67]. Actin is also highly conserved in evolution. One idea is that because actin interacts with 100 - 200 different actin binding proteins (ABPs), any variation in sequence and structure will likely be detrimental to one or more of these interactions. A more recent explanation points to the cooperative and allosteric properties of actin as factors constraining its evolutionary variability [36].

Fig. 1.1 shows actin at various length scales. Monomeric actin is a $\sim$42 kDa protein made up of 375 amino acids, with a diameter of approximately 5.4 nm. At physiological conditions,

G-actin monomers polymerize in a double-helical fashion to form F-actin (Fig. 1.1 b and c). Because each actin monomer is structurally asymmetric, the resulting F-actin also exhibits structural polarity with a plus (barbed) end and a minus (pointed) end. Monomers can be added and removed at either end. However, both the addition and subtraction processes occur faster at the barbed end than at the pointed end [91]. In general, above critical free monomer concentrations, growth occurs at the barbed end.

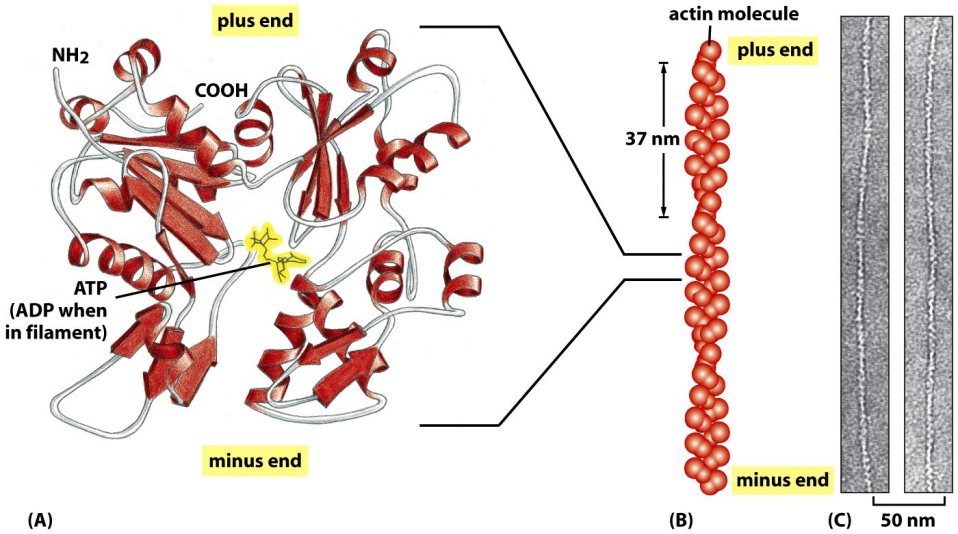

Figure 1.1: **Monomeric and polymeric actin.** (a) The building blocks of polymeric actin are G-actin monomers. Each actin monomer has a molecular weight of ∼42 kDa and is approximately 5.4 nm in diameter. (b) Actin monomers assemble together in a double helix to form F-actin. F-actin has a diameter of 8.4 nm but exists in a wide range of lengths in cells. Polymeric actin is polar, with a plus and a minus end, which means that the kinetics of assembly and disassembly occurs at different rates at the two ends. (c) Actin filaments seen using electron microscopy. Figure adapted from [2].

1.2 Single filament properties

Single actin filaments exhibit significant thermal bending fluctuations that are essential to the mechanical properties of actin filaments and networks. The scale of bending flexibility is defined by the persistence length (l_p), which is the length scale at which tangent vectors along the contour of a filament become decorrelated. Actin has a persistence length on the order of ∼10 μm [57, 43].

There are three classes of polymers in polymer theory. Flexible polymers are defined by having a persistence length much less than their contour length. For these polymers, entropy dominates their elastic properties because stretching them decreases the number of

degenerate states and the corresponding conformational entropy. On the other extreme, stiff polymers have a persistence length that is much smaller than its contour length. Because these chains bend very little, their elasticity is dominated by the enthalpy of their constituent monomers and distances relative to each other. Actin filaments, with a persistence length that is comparable in magnitude to their contour length, belong in a class of polymers called semiflexible polymers. These polymers exhibit significant bending fluctuations and their material properties are governed by a mixture of entropic and enthapic contributions.

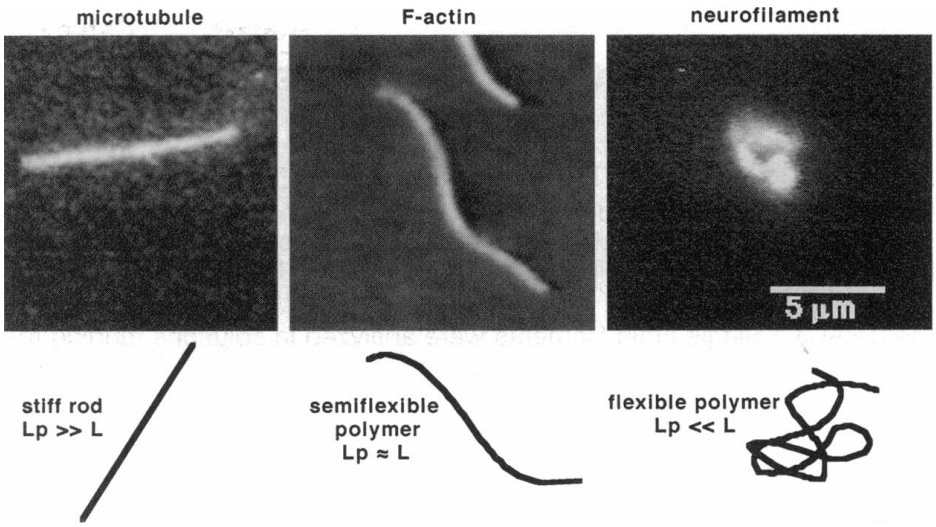

Figure 1.2: **Classes of polymers.** In polymer theory, the three classes of polymers are flexible polymers, stiff rods, and semiflexible polymers. Flexible polymers such as neurofilaments have a persistence length much greater than the contour length and are often found as coils. Stiff rods such as microtubules have a persistence length much smaller than the contour length and appear very stiff. For semiflexible polymers such as actin, the persistence length is on the order of the contour length. These polymers exhibit significant bending fluctuations and their material properties are governed by a mixture of entropic and enthapic contributions. Figure adapted from [60].

In addition to bending motions, actin filaments also undergo twisting motions. Experiments have found that actin filaments have a twist distribution centered between 166° and 167° per monomer, although interactions with the actin binding protein cofilin can shift this distribution downward by 5° [115, 78]. The torsional elasticity is captured by the torsional rigidity. For actin, there are several estimates for this value ranging from 0.23–8.0 $\times 10^{-26}$ Nm^2 [125, 96].

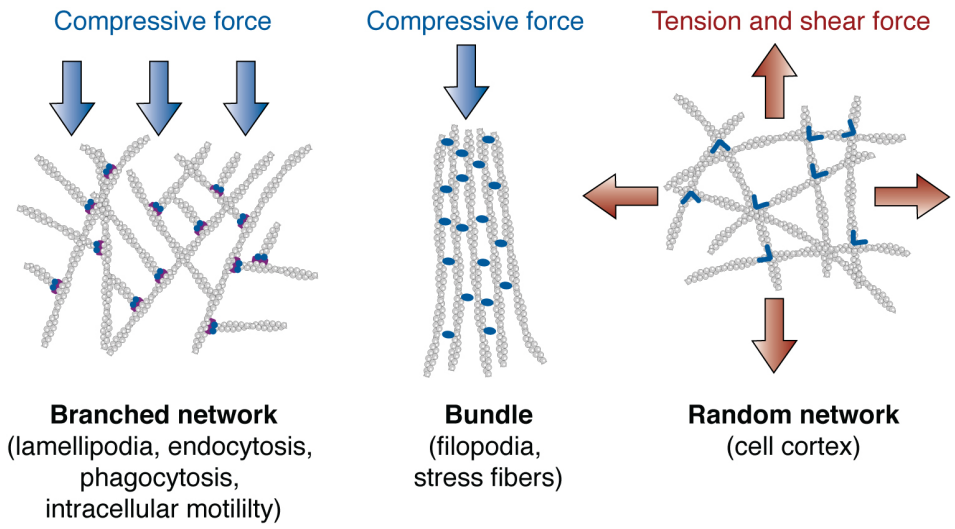

Figure 1.3: **Architectures of actin networks.** Depending on where you look in the cell, you can find actin in different architectures, interacting with different actin binding proteins, and subjected to different kinds of forces. Three very prominent and different networks are the branched networks near the tip of the lamellipodia, tight bundles in filopodia and stress fibers, and random networks in the cell cortex. Figure made by Viviana Risca.

1.3 Architecture of actin networks

The architecture of actin networks is varied in different parts of the cell. This structural heterogeneity is intimately tied to the function of actin in each part of the cell, thus allowing actin to play a wide variety of roles and respond to different kinds of forces [32]. Fig. 1.3 shows three different actin network structures found within the cell.

1.3.1 Branched network

By mass, actin is the major component in the lamellipodia, a thin, mesh-like region near the edge of the cell. Near the tip of the lamellipodia and close to the plasma membrane (also called the leading edge of the cell), the assembly of actin filaments pushes on the membrane, allowing cells to craw [93]. The architecture of the actin network at the leading edge is a branched network, also called a dentritic network. In this region, actin filaments can branch, and essential in this process are proteins known as actin-related proteins 2 and 3 (Arp2/3), with five additional associated proteins ARPC 1-5. Together, these proteins are more commonly referred to as the Arp2/3 complex. Upon activation by a nucleation promoting factor (NPF), Arp2/3 can nucleate new "daughter" filaments from pre-existing "mother" filaments by attaching itself to the mother filament. The daughter filament connects to the mother filament at a 70° angle, and the resulting structure has a characteristic Y-shape [44].

1.3.2 Bundle network

Tightly bundled and unbranched actin networks are found in stress fibers and filopodia. In stress fibers, the actin binding protein α-actinin crosslinks nearly filaments into bundles [123]. The molecular protein myosin II can walk on these bundles, enabling them to contract. In filopodia, parallel actin filaments crosslinked by fascin proteins protrude from the cell, allowing cells to explore their environment and respond to various extracellular mechanical and chemical signals [39, 73].

1.3.3 Random network

Under the plasma membrane of animal cells, we find actin in a random or non-aligned network that aids the cell in maintaining its shape [107]. In this network architecture, nearby filaments are crosslinked by the relatively flexible actin binding protein filamin, which links filaments that are approximately orthogonal to each other [2].

1.4 Research approach

In the previous sections, we have introduced actin's various roles, structures, and dynamics in the cell. These diverse behaviors and architectures stem from a very complex and intricate piece of molecular machinery.

How do we begin to probe such a complicated protein? Because of the sheer size of actin filaments and networks, we cannot simulate every atom or component in the entire system. And although every part of a biological system is important to some extent and contributes to its overall behavior, not every component of the feature space is necessary to answer a specific question. If we are probing a system's behavior at a certain length scale, details at much smaller length scales can often be reduced and simplified. The main goal in the model building process is to select a level of abstraction or representation that is appropriate for answering a particular question. Making judicious choices about what to include and what to leave out can mean the difference between obtaining a result in a day, a month, or never being able to answer a question at all. In our work, we develop and modify simplified (coarse-grained) models of the actin filament and network that nonetheless capture the relevant behavior that we are trying to understand.

With a model that describes the pertinent behavior of the system, we can ask questions about how tuning the parameters of the model or modifying the constraints of the system changes the system behavior. The implementation takes form in various flavors of Monte Carlo simulations. From analyzing differences in resulting distributions in the protein conformation or behavior, we start to gain an understanding of what kinds of factors affect the behavior of the protein and what are the underlying explanations to questions we are asking.

1.5 Overview

One of the most important roles for actin is to provide structural integrity to the cell, preventing the cell from collapsing under force. Depending on where one looks in the cell, different proteins and mechanisms contribute to this role. Despite many years of both experimental and theoretical research, there are still many open questions and undiscovered mechanisms. The central theme of this work is to explore the effect of force on actin to better understand how single filaments and networks adapt to their changing mechanical environment. The chapters in this work are separated into two parts by the length scales we are probing, which also dictate the resolution of the simulation models we utilize. In part I (chapters 2–4), we explore how force affects actin at the single filament level, with applications to protein binding. In part II (chapters 5–6), we investigate the elastic properties of actin at the network level.

In chapter 2, we introduce a coarse-grained model for single actin filaments that can resolve curvature fluctuations at the nanoscale. We utilize this model in chapters 3 and 4.

In chapter 3, we examine the regulation of Arp2/3 binding by actin itself in a collaboration with Viviana Risca and coworkers in the group of Daniel Fletcher from the Department of Bioengineering at the University of California, Berkeley. My experimental collaborators found that Arp2/3-nucleated branches preferentially form on the convex side of bent filaments. Using Monte Carlo simulations of a worm-like chain representation of actin, we developed a fluctuation-gating model in which binding of the Arp2/3 complex to the side of an actin filament only occurs when the filament undergoes a rare fluctuation that induces high local curvature over a length scale on the order of the 10 nm footprint of the Arp2/3 complex. In the context of the cell, near the plasma membrane, compressive forces of the membrane oppose the force generated by the growing actin filaments, resulting in filament bending away from the force. However, this causes the cell to be structurally weaker. Our results indicate that new branches are more likely to form in the direction facing the force, restoring the structural integrity of the cell. Furthermore, our model shows that actin itself is a mechanosensor and can actively respond to mechanical environmental cues to regulate the binding of ABPs, in this case Arp2/3.

The fluctuation-gating model can serve as a useful framework for studying the effects of tensile force on the binding and function of other proteins with cytoskeletal filaments or membranes. In order to identify the details of these mechanisms, it is necessary to characterize the distribution of curvature fluctuations as a function of external force or spatial constraints. However, this is very difficult to measure experimentally. In chapter 4, we derive analytical expressions for the nanometer-scale curvature distribution of a worm-like chain and membrane as a function of applied tension. Our results will be applicable to any model that presupposes a role of local curvature in the association of proteins with semiflexible polymers such as actin and DNA, as well as membranes such as the plasma membrane and endosomes.

In the last two chapters, we extend our study to examine how actin networks respond to large external forces. However, the theoretical toolkit for tackling such a problem is not yet

complete. Although strain fluctuation methods first developed by Parrinello and Rahman [86] can be used to apply stress to and measure the elastic properties of systems with a linear stress-strain response, there is currently no computational method to accurately apply stress to nonlinearly elastic materials. In chapter 5, we develop a constant-stress method to apply large forces on soft materials in order to probe the nonlinear stress-strain behavior of actin gels. Additionally, we develop a toy model of a soft elastic solid with a nonlinear elastic response to test our constant-stress method.

In chapter 6, we utilize the constant-stress method and a coarse-grained model for short, semiflexible chains to probe actin network elasticity under compression, a biologically important phenomenon. We found that for a variety of network structures and features, the networks exhibited stress softening behavior. From a single filament perspective, network compression gives rise to a bimodal distribution of segment lengths composed of bent and unbent filaments, with no evidence for filament stretching. Additionally, we use normal mode analysis to identify network soft regions and obtain a rough estimate of the relative linear elastic modulus among various networks. These results can motivate and aid the interpretation of new experiments in this area.

Part I

Single filament level

Chapter 2

Coarse-grained model of actin at the single filament level

A main component of this work is to reduce a complex system into simplified simulation models, selecting a level of representation that is appropriate for the question at hand. In this chapter, we describe the coarse-grained model we use to probe the properties of single actin filaments, in particular nanoscale curvature fluctuations. We utilize this model in chapters 3 and 4.

2.1 Worm-like chain model

Theoretically, semiflexible polymers such as actin are well described by the worm-like chain model, also known as the Kratky-Porod model [64, 34]. The energy of a WLC described by the space curve $\mathbf{r}(s)$ and parameterized by arc length s is

$$E = \frac{k_B T\, l_p}{2} \int_0^L ds \left| \frac{\partial^2 \mathbf{r}(s)}{\partial s^2} \right|^2 , \tag{2.1}$$

where L is the contour length and l_p is the persistence length. In the model, the energy penalty for bending scales quadratically with the local curvature $\kappa(s)$, defined as

$$\kappa(s) = \left| \frac{\partial^2 \mathbf{r}(s)}{\partial s^2} \right| = \left| \frac{\partial \mathbf{t}(s)}{\partial s} \right| , \tag{2.2}$$

where $\mathbf{t}(s) = \partial \mathbf{r}(s)/\partial s$ is the unit tangent vector. One property of the WLC model is that the tangent-tangent correlation function decays exponentially

$$\langle \mathbf{t}(s) \cdot \mathbf{t}(s') \rangle = \exp\left(\frac{-|s - s'|}{l_p} \right) . \tag{2.3}$$

This function can be integrated to obtain the mean squared end-to-end distance of a worm-like chain [106]

$$\begin{aligned}\langle R^2 \rangle &= \int_0^L \int_0^L \exp\left(\frac{-|s-s'|}{l_p}\right) ds\, ds' \\ &= 2L\, l_p - 2\, l_p^2 \left(1 - \exp\left(-\frac{L}{l_p}\right)\right).\end{aligned} \tag{2.4}$$

2.2 Discretized worm-like chain

For purposes of simulation, we utilize a discretized version of the WLC model made up of a linear sequence of beads, each separated from adjacent beads by a fixed length. For example, a chain with contour length L and a discretization length Δs would be represented by $L/\Delta s + 1$ bead positions $\mathbf{r}_i$, or viewed in another way, a list of bond vectors connecting adjacent beads $\mathbf{b}_i = \mathbf{r}_{i+1} - \mathbf{r}_i$. The bond vectors relate to the the unit tangent vectors $\hat{\mathbf{t}}_i$ as

$$\mathbf{b}_i = \hat{\mathbf{t}}_i\, \Delta s. \tag{2.5}$$

The energy of a discretized WLC is

$$E = k_B T \sum_i^{L/\Delta s} \frac{l_p}{2} \kappa_i^2 \Delta s = k_B T \sum_i^{L/\Delta s} \frac{l_p}{\Delta s}(1 - \cos\theta_i), \tag{2.6}$$

where $\kappa_i = \hat{\mathbf{t}}_{i+1} - \hat{\mathbf{t}}_i$ and $\theta_i = \cos^{-1}\left(\hat{\mathbf{t}}_{i+1} \cdot \hat{\mathbf{t}}_i\right)$. A schematic of a discretized WLC is shown in Fig. 2.1.

2.3 Coarse-graining resolution

In order to understand the complex interactions and mechanisms that contribute to actin behavior at the single filament level, it is necessary to model actin filaments at a resolution most appropriate for the problem. For the problem described in chapter 3, each bead of the WLC represents a pair of actin monomers (Fig. 2.2). We choose this discretization length scale because it allows us to calculate curvature at a length scale most comparable to the binding footprint of Arp2/3. The discretization length Δs is set to 5.4 nm, representing the distance between the centers of two adjacent actin monomer pairs.

2.4 Monte Carlo procedure

With a model and corresponding energetics, we can sample the conformational fluctuations of the model using the Metropolis implementation of Monte Carlo. To ensure the correct

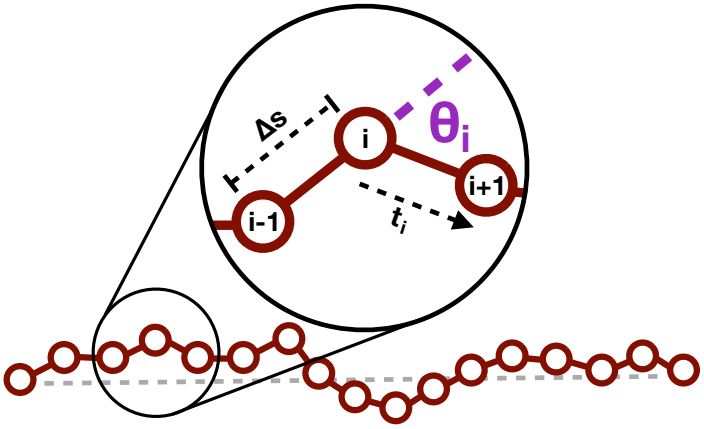

Figure 2.1: **Model for actin filaments.** In the schematic, actin is represented as a chain of non-interacting and inextensible position vectors representing actin monomer pairs. $\mathbf{r}_i$ and $\hat{\mathbf{t}}_i$ represent the position and tangent vectors at position i, respectively. Δs is the discretization length and θ_i is the local bending angle at position i.

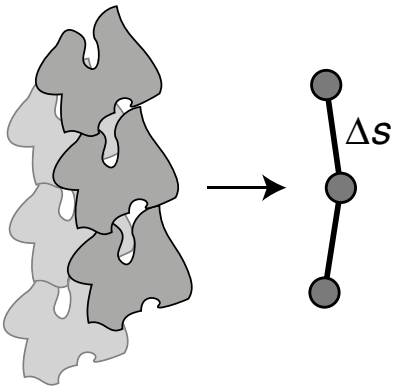

Figure 2.2: **Coarse-graining resolution.** Each particle of model (right) stands for two actin monomers in the filament (left), with $\Delta s = 5.4$ nm, representing the distance between the centers of two adjacent actin monomer pairs.

sampling, we propose trial moves to the chain and accept these moves according to the Metropolis acceptance criteria [79],

$$P_{acc} = \begin{cases} e^{-\Delta E/k_B T} & \text{if} \quad \Delta E > 0 \\ 1 & \text{if} \quad \Delta E \leq 0 \end{cases} \tag{2.7}$$

where P_{acc} is the probability of accepting a proposed configuration, ΔE is the change in energy of the system going from one configuration to another, k_B is Boltzmann's constant, and T is the system temperature.

2.4.1 Monte Carlo moves

For an efficient and ergodic sampling of the conformational space, we use a combination of free rotation and crankshaft moves [126], shown in Fig. 6.9.

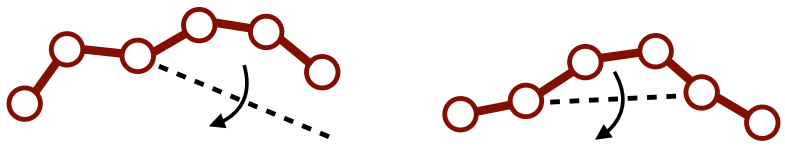

(a) (b)

Figure 2.3: **Monte Carlo moves.** We use a combination of (a) free rotation and (b) crankshaft Monte Carlo moves.

In a free rotation move (Fig. 6.9a), a random particle from the chain is selected. Then the particles on one side of the selected particle are rotated by an random angle around a random axis passing through the selected particle. In a crankshaft move (Fig. 6.9b), two different particles are selected at random from the chain. Then, the particles in between are rotated by a random angle around the line segment that connects the two selected particles. The random angles are drawn from a uniform distribution, with a maximum threshold unique to each move such that the acceptance rate for each move is approximately 40%.

Chapter 3

Actin filament curvature biases branching direction

The work described in this chapter was performed in collaboration with Viviana Risca, Ovijit Chaudhuri, Jia Jun Chia, and Professor Daniel Fletcher. All experiments were performed by Viviana Risca. It is used with permission and was previously published as:

V. Risca, E. Wang, O. Chaudhuri, J. Chia, P. Geissler and D. Fletcher. "Actin filament curvature biases branching direction", *PNAS*. 2012, 109, 2913-2918.

Mechanical cues affect many important biological processes in metazoan cells, such as migration, proliferation, and differentiation. Such cues are thought to be detected by specialized mechanosensing molecules linked to the cytoskeleton, an intracellular network of protein filaments that provide mechanical rigidity to the cell and drive cellular shape change. The most abundant such filament, actin, forms branched networks nucleated by the Arp 2/3 complex that support or induce membrane protrusions and display adaptive behavior in response to compressive forces. Here we show that filamentous actin serves in a mechanosensitive capacity itself, by biasing the location of actin branch nucleation in response to filament bending. Using an *in vitro* assay to measure branching from curved sections of immobilized actin filaments, we observed preferential branch formation by the Arp2/3 complex on the convex face of the curved filament. To explain this behavior, we propose a fluctuation gating model in which filament binding or branch nucleation by Arp2/3 occur only when a sufficiently large, transient, local curvature fluctuation causes a favorable conformational change in the filament, and we show with Monte Carlo simulations that this model can quantitatively account for our experimental data. We also show how the branching bias can reinforce actin networks in response to compressive forces. These results demonstrate how filament curvature can alter the interaction of cytoskeletal filaments with regulatory proteins, suggesting that direct mechanotransduction by actin may serve as a general mechanism for organizing the cytoskeleton in response to force.

3.1 Introduction

Mechanical forces from a metazoan cell's environment are transduced into biochemical signals during many biological processes, such as the differentiation, proliferation, and migration of cells, to regulate processes ranging from cytoskeletal remodeling to gene expression [29]. Mechanotransduction has been thought to occur primarily via specialized mechanosensing molecules, which stretch or unfold in response to applied forces [129, 53], whereas the filament networks that make up the bulk of the cytoskeleton have been studied primarily as materials, whose mechanical properties determine how they transmit or absorb forces [58, 32]. We asked whether F-actin, a major part of the cytoskeleton, can act as a mechanosensor in its own right.

The actin cytoskeleton consists of an organized network of filaments that bear both tensile and compressive forces and largely determine the shape and rigidity of metazoan cells [32]. Growth of one specialized cytoskeletal structure, the branched actin network [46, 93, 133], produces forces that act on cellular membranes to help them protrude or change shape [42, 71, 85, 95] and plays an important role in cell motility, the trafficking of cellular membranes including endocytosis, and the motility of intracellular pathogens [31, 48]. When this protrusive growth is opposed by resistance from the surrounding cytoskeleton or plasma membrane, the actin network compresses, and filaments in the network bend [16, 41, 62, 66]. *In vitro* studies have shown that compressive forces applied to branched networks cannot only reversibly deform them [16] but can also alter their density [113] and growth velocity [71, 85], suggesting that their architecture may respond actively to mechanical forces. Although the binding of many ABPs to the side of an actin filament has been characterized [77] and, in some cases, shown to depend on the filament's twist [20, 35] or its bound nucleotide [68, 83], the response of most F-actin-ABP interactions to filament bending is unknown [32]. The only such response that has been documented is an increased frequency of severing by actophorin or its homolog actin depolymerizing factor (ADF)/cofilin at highly curved sections of actin filaments [68, 76].

Bending of F-actin is particularly relevant to its interaction with the Arp2/3 complex because of the complex's central regulatory and structural roles in the formation of branched actin networks [46]. Upon activation by two molecules of NPF localized at or near a membrane, the Arp2/3 complex nucleates a new, "daughter" filament from the side of a preexisting "mother" filament, forming a Y-shaped branch that serves as the basic structural unit of these networks [92, 84, 122] (Fig. 3.1). Importantly, the Arp2/3 binding site on F-actin spans three actin monomers along F-actin's long-pitch helix, suggesting that its binding may be affected by changes in both monomer conformation and intermonomer distance induced by bending stresses [23].

The mechanism of Arp2/3 branch nucleation (Fig. 3.1) is understood to involve conformational changes in the Arp2/3 complex induced by the binding of NPFs [92, 84, 122, 23, 45]. Additional conformational changes in both the Arp2/3 complex and several monomers in the mother filament probably occur upon the binding of the ternary complex of NPFs, Arp2/3, and G-actin to the mother filament or during a subsequent activation step that is necessary

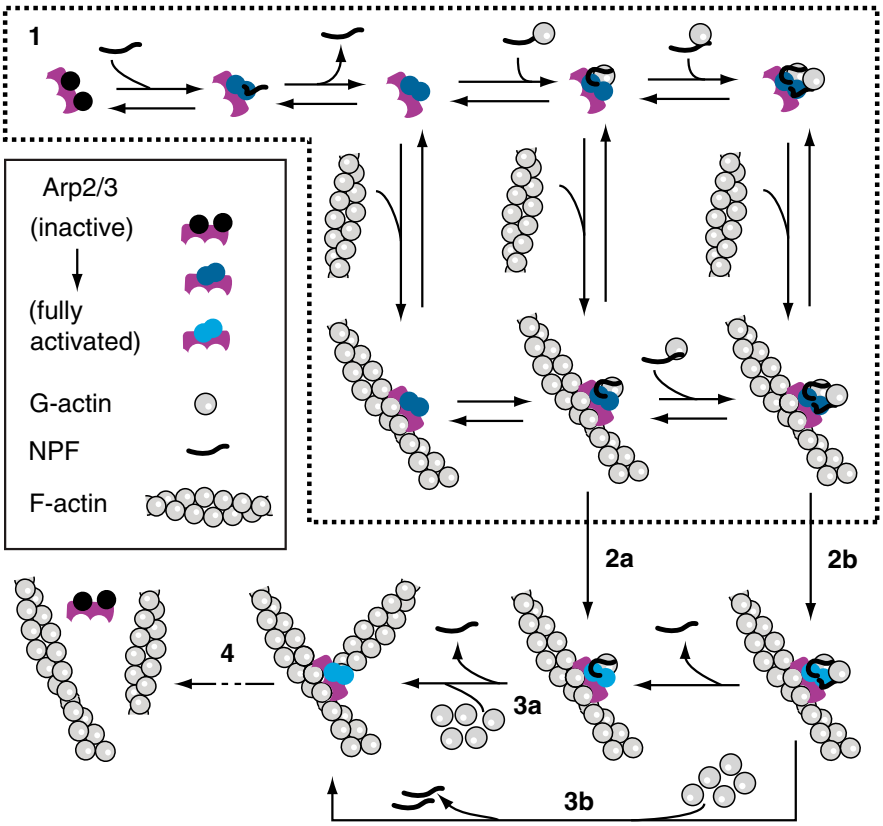

Figure 3.1: **Arp2/3 branch nucleation pathway.** Arp2/3 branch nucleation occurs via a complex pathway [8, 84, 92, 122]. (1) The Arp2/3 complex (violet and shades of blue), one or two molecules of nucleation-promoting factor (NPF, black curve), and one or two G-actin monomers (gray), assemble on a preexisting F-actin "mother" filament (gray). Interaction with the NPF causes a conformational change in the inactive Arp2/3 complex (violet and black) that partially activates it, bringing Arp2 and Arp3 into a conformation similar to a short-pitch helix actin dimer (violet and dark blue). There are multiple pathways for assembly of this complex, and the extent to which different pathways are populated in vivo remains to be elucidated. (2a and 2b) The mother filament bound Arp2/3 complex then undergoes a further conformational change that fully activates the Arp2/3 complex (violet and light blue) for nucleation of a new actin filament as a branch on the mother filament. (3a and 3b) This new filament then elongates as more actin monomers bind to its free barbed end, and the NPF dissociates soon after nucleation. (4) After several minutes, the two filaments dissociate in a process called debranching.

to allow branch nucleation [92, 8], because the bound NPFs appear to partially overlap the F-actin binding surface of the Arp2/3 complex [25]. Once formed, the branch can then survive for minutes *in vitro* before dissociating (a process called "debranching") [69]. The rate of debranching has been shown to depend on the nucleotide bound to the mother filament (ATP, ADP-Pi or ADP) [69], and on the presence of the actin stabilizing drug phalloidin [24, 70]. Branch nucleation appears to happen most readily on actin in the ATP-bound state [56], although it is not yet fully determined whether this is due to enhanced nucleation or stability against fast debranching. Experiments that used saturating amounts of phosphate to stabilize actin in the ADP-Pi-bound state showed a rate of barbed end creation similar to that on unstabilized actin [69]. The regulation of both branch nucleation and branch stability by direct mechanical factors has not yet been studied. We asked whether filament bending by externally imposed geometric constraints plays a regulatory role at any point in this actin branch nucleation pathway.

3.2 Experimental results

3.2.1 Surface-based branching assay reveals that actin filament curvature biases branching direction.

To examine whether and how the bending of filaments affects their interaction with the Arp2/3 complex, we imaged branch nucleation from fluorescently labeled F-actin that was preimmobilized on a surface before incubation with Arp2/3 complex, an NPF, and monomeric actin (G-actin) (Fig. 3.2 a-c). From the total of 403 images (Fig. 3.2d) acquired in five independent experiments, we measured the distribution of curvature along the immobilized mother filaments [135] (Fig. 3.2 e-h). Curvature varied smoothly as observed by fluorescence microscopy and could be measured on filaments spanning at least 3 μm, with a spatial resolution of approximately 1.1 μm. We were able to infer the location of Arp2/3 complex binding on the mother filament, with a spatial resolution of approximately 500 nm, from the location and direction of the short and stiff actin branches it nucleated, which were imaged separately from mother filaments using a two-color fluorescent labeling strategy [24, 56]. Filament curvature at branch points and the direction of branch growth (Fig. 3.2c) determined the sign of the curvature value assigned to each branch. Branches on the convex side of the filament curve were assigned negative curvature, and branches on the concave side were assigned positive curvature.

Interestingly, we observed that branches were more likely to be found on the convex surface of a curved filament than on the concave surface. We compared the distribution of curvatures measured at equally spaced points 182-nm apart along a total of 27.4 mm of mother filaments where branches could have formed (Fig. 3.3a), to the distribution of curvatures observed at 10,443 branch points, where branches actually formed (Fig. 3.3b). If branch density were independent of mother filament curvature, the two distributions would be identical after normalization. Instead, we found that the distributions were different

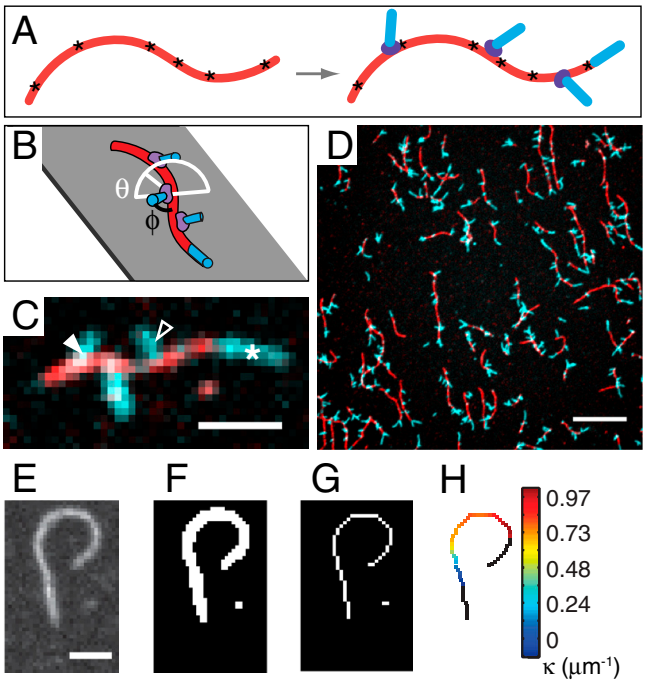

Figure 3.2: **Branching from curved filaments *in vitro*** (a) Mother filaments (red) immobilized via biotin-streptavidin tethers (asterisks) before nucleation of branches (cyan blue) by Arp2/3 complex (violet). (b) Actin branches grow at a branch angle $\varphi \sim 70°$ to the mother filament (black line) with an azimuthal angle θ from 0° to 180° (white line). (c) Fluorescence image of actin growth at mother filament ends (white asterisk) and on branches on concave (open arrowhead) and convex (filled arrowhead) sides of mother filament curves. (Scale bar: 2 μm.) (d) Sample field of view. (Scale bar: 10 μm.) (e-g) Filament image thresholded and skeletonized to an 8-connected digital curve. (Scale bar: 2 μm.) (h) Mother filament curvature measured with the tangent angle method.

(Fig. 3.3c) and calculated their ratio, which we call the relative branch density (Fig. 3.3d).

The relative branch density increased with negative curvature, indicating that extensional strain on the Arp2/3-binding surface of F-actin makes branch nucleation more likely, whereas compressional strain makes it less likely (Fig. 3.3d). We quantified the trend with a weighted least-squares linear fit to the relative branch density calculated from a subset of mother filament curvature samples selected randomly, one per filament to strictly satisfy the assumptions underlying linear regression. The weights were the number of samples of mother filament curvature in each curvature bin. The relative linear branch density decreased with a slope of -33% per μm^{-1} of curvature [95% CI: (-40, -26%), $R^2 = 0.56$]. Thus, the probability of finding a branch on the convex side of a filament with a curvature of 1 μm^{-1} is 99% higher than finding it on the concave side. Linear regression against the full dataset containing multiple curvature measurements from each mother filament yielded similar results.

To quantify the effect of filament bending on total linear branch density, we carried out the same analysis as above with unsigned branch curvatures (Fig. 3.3 e and f) and found that the likelihood of branching per unit length shows a weak dependence on curvature (Fig. 3.3 g and h) with a slope of 13% per μm^{-1} [95% CI: (3.3, 23%)]. However, the linear fit does not describe the unsigned curvature data very well ($R^2 = 0.17$), and the size of the deviation from a flat curve is comparable to the size of systematic errors in digital curvature estimation. In addition, fitting the data with a higher-order polynomial did not significantly improve the fit ($p = 0.06$, ANOVA). We conclude that total linear branch density depends weakly on absolute curvature, and we focus on studying the predominant effect of mother filament curvature on branch direction.

To confirm that the existence of a branching bias due to curvature was robust to the analysis method, we applied an alternative spline-based curvature estimation algorithm [135, 9]. The exact value of the slope depended on the curvature estimation method, but the observation of branch direction bias due to curvature [-14% per μm^{-1} of curvature, 95% CI: (-17, -10%)] was unchanged. We also checked how our estimate of bias in the direction of branching was affected by changes in image magnification and found only a weak effect ($p = 0.076$).

As biochemical controls, we verified that our results do not depend on the mode of actin labeling ($p = 0.69$). We also tested whether stabilizing the mother filament in the ADP-Pi-bound state by adding 25 mM phosphate affected the observed branching bias and did not observe an effect ($p = 0.998$), nor did we observe a significant change in slope due to phalloidin stabilization of F-actin ($p = 0.10$).

3.2.2 The observed bias in branch direction is not caused by debranching

Mother filament curvature may influence one or several of the steps in the branch nucleation pathway. Because we imaged the end products of this branching pathway, we could not address the effect of mother filament curvature on Arp2/3 binding separately from branch nucleation. To address the role of debranching, we incubated samples in which branching had occurred for 2 min for an additional 33 min in the absence of Arp2/3 complex. We did not observe debranching during the additional incubation time (Fig. 3.4a), even with a high concentration of blocking protein (2 mg/mL BSA) included in solution to prevent nonspecific adsorption of branches onto the coverslip surface. To quantify branch density and its dependence on curvature, we incubated different samples for either 50 s or 15 min before stabilization with phalloidin. In these experiments, the branch density decreased, but not to a statistically significant extent (Fig. 3.4b), and there was not a statistically significant difference in the slope of the relative branch density as a function of curvature (Fig. 3.4c). These results indicate that mother filament curvature primarily acts on branch nucleation.

It is also possible that curvature acts on the stability of very short branches that were proposed by Mahaffy and Pollard to dissociate before microscopy-based methods can detect

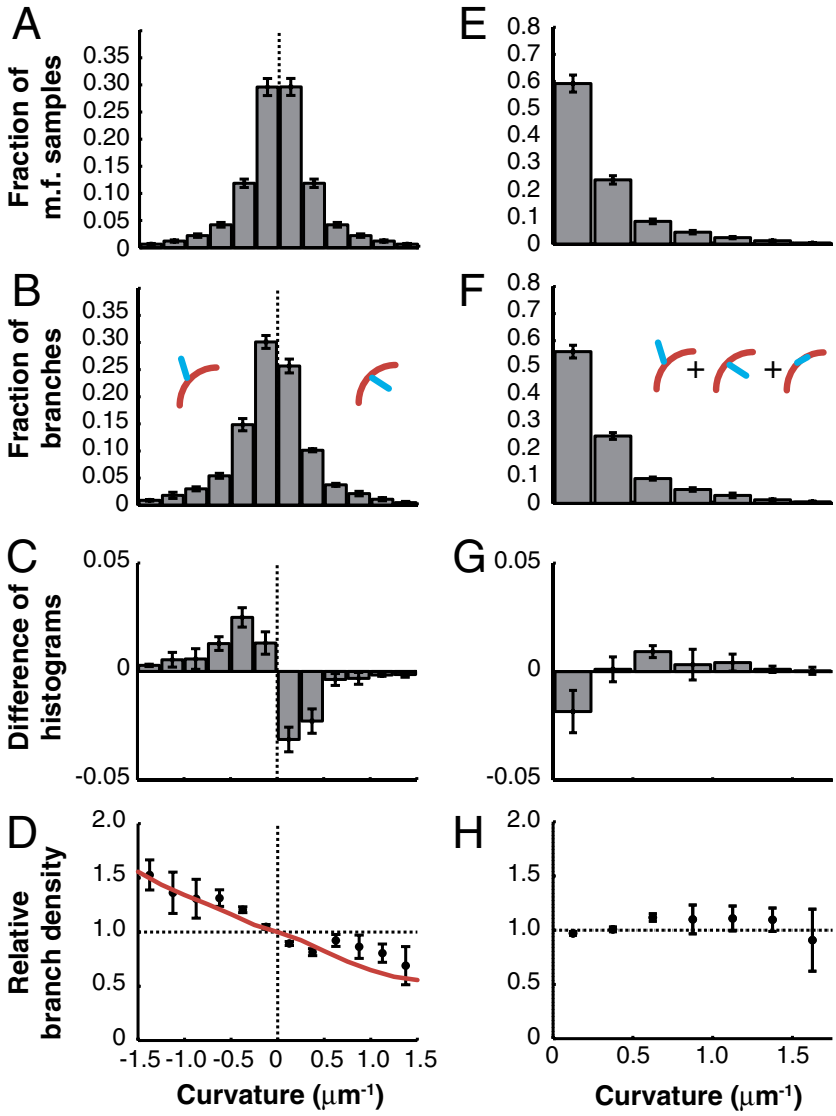

Figure 3.3: **Filament curvature biases branching direction.** (a) Mother filament curvature distribution and (b) the distribution of mother filament curvature at branch points measured with the tangent angle method. (c) The difference and (d) the ratio of the histograms in b and a. The latter is called the relative branch density. The red curve represents the best fit (by least squares) by the fluctuation gating model with a 5 μm^{-1} threshold curvature. c, d, g, and h were normalized using a simulated control. (e-h) The unsigned curvature distributions corresponding to a-d. Error bars: SEM, $n = 5$ independent experiments.

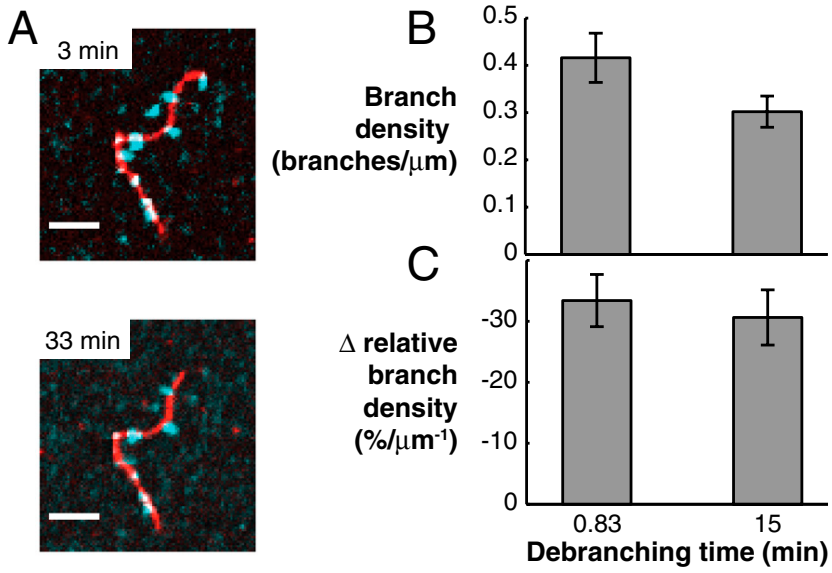

Figure 3.4: **Branch stability does not affect branching bias.** (a) Actin branches (cyan blue) grown from unstabilized mother filaments (red) and incubated in buffer with unlabeled actin but without phalloidin stabilization for times shown exhibited little to no debranching when the same sample was imaged at the two time points. (Scale bars: 5 μm.). (b and c) To obtain enough images for curvature analysis, identical but separate samples were prepared with incubation times of 0.83 or 15 min. in KMEI buffer with unlabeled actin before stabilization with phalloidin and imaging. (b) We found a decrease in overall branch density between short and long incubation samples, but it was not statistically significant ($p = 0.12$, Welch's t test, $n = 4$). (c) There was no significant difference in the slope of relative branch density with respect to curvature. Error bars: SEM.

them [69]. However, the lack of dependence on phosphate added at a concentration similar to that used by Mahaffy and Pollard suggests that curvature most likely acts on nucleation rather than dissociation. Overall, we do not exclude the possibility that curvature may affect fast debranching that we do not detect, but we favor the interpretation that curvature primarily affects branch nucleation. Itchetovkin et al. observed an enhanced branch density on filaments stabilized in the ATP-bound state [56], suggesting that the presence of ATP may have an effect on the nucleation process and may also affect sensitivity to curvature. However in our experiments, freshly polymerized actin containing ATP was only present on filament ends, where curvature could not be accurately measured.

3.3 Simulation model

3.3.1 Bridging lengthscale differences

Because the length scale relevant to Arp2/3 binding and branch nucleation is 5-10 nm, well below the length scale at which fluorescence microscopy can measure curvature and also below the micrometer length scale at which curvature can be externally imposed, we used Monte Carlo simulations of a discretized worm-like chain polymer to assess the nanometer-scale implications of the micrometer-scale curvature.

3.3.2 Coarse-grained model

The validity of the WLC model to F-actin elasticity has been demonstrated for filament curvatures as high as 5 μm^{-1} [26]. In our work, the WLC polymer, with the persistence length of actin ($l_p = 9$ μm) [57], was pinned to a plane with imposed curvature, κ_0, mimicking tethering of actin filaments to a plane surface in experiments (Fig. 3.5).

F-actin was coarse-grained as a discretized WLC polymer (details in chapter 2) composed of 5.4-nm-long bonds between particles, with a persistence length of 9 μm [57]. We restrict Monte Carlo moves to certain sections of the 1.25-μm-long filament, effectively pinning down the filament at six equally spaced points. The Monte Carlo moves consist of attempts to perform a crankshaft move (shown in Fig. 6.9b). Conformations are sampled with the Metropolis acceptance criterion.

Robustness analysis was performed to examine the effect of changing various simulation parameters on the distribution of local curvatures. The parameters considered were (i) length between adjacent particles, (ii) contour length of filament between tether points, (iii) "looseness," the ratio of end-to-end length to contour length between tether points, (iv) number of tethers, and (v) curvature resolution and the possible need to average curvature over neighboring angles. These test simulations revealed that only averaging over neighboring angles has a significant effect on curvature distributions. The final set of parameters employed for the simulations is 5.4 nm between adjacent particles, a contour length of 250 nm between tether points, the end-to-end length between tether points for a given contour length equal to the average end-to-end distance for a free WLC polymer of the same persistence length and contour length (Eq. 2.4).

Imposed curvatures were largely in a 2D plane because filaments were tethered to the coverslip surface and their stiffness limited out-of-plane bending of large amplitude. Filament ends and large loops that were not tethered were blurred during the 1-s exposures used, and were eliminated during image thresholding. To approximate the experimental conditions, the WLC filament was simulated in three dimensions, but tethered to a 2D plane and curvature was measured in 2D from the projection of the filaments' shape onto that plane, neglecting out-of-plane bending. For consistency, 2D projection was used for all curvature analysis of filament shape in experiments and simulations, as well as for determination of branch direction. The reported relative linear branch density also contained an internal control, as

branching from curved filament sections can be compared directly to branching from straight filament sections.

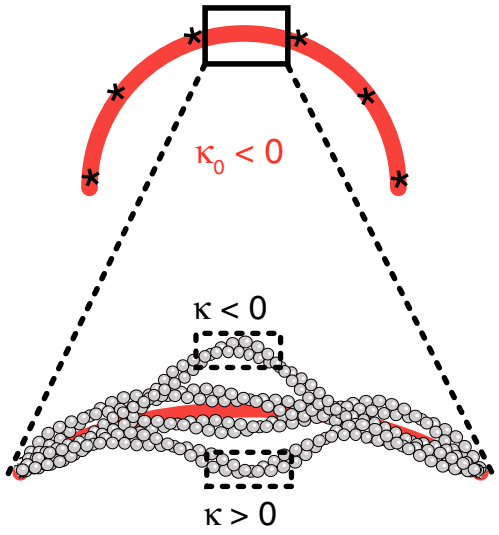

Figure 3.5: **Mimicking tethering of actin filaments.** Schematic of the WLC polymer tethered at six points (asterisks) to a curve with imposed curvature $\kappa_0 < 0$. Fluctuations with local curvature $\kappa < 0$ and $\kappa > 0$ are possible. Curvature was calculated from the section between the middle two tethered particles in order to avoid end effects.

3.4 Simulation results

3.4.1 Simulations reveal the nanoscale curvature fluctuations of constrained filaments

Despite being constrained to an average curvature of κ_0, the simulated filament exhibits large thermal fluctuations in nanometer-length-scale local curvature about that average. The breadth of the local curvature distribution is large in comparison to the range of experimentally accessible imposed curvatures. In Fig. 3.6, we show that for the side of a filament with convex average curvature of -1 μm^{-1}, locally concave fluctuations occur almost as often as locally convex ones. This small, 10% asymmetry is inconsistent with the larger, 99% asymmetry in branch density we observed between the two sides of filaments with -1 μm^{-1} average curvature (Fig. 3.3d). Strong differences between the sides of the filament with convex and concave average curvature only occur in the extreme tails of the corresponding curvature distributions. Therefore, we conclude that branching must be sensitive to local curvature fluctuations that are far from the average. In addition, because such extreme local

curvature fluctuations occur rarely, making the system slow to reach chemical equilibrium, we discuss the effect of curvature on branch nucleation by Arp2/3 in kinetic terms.

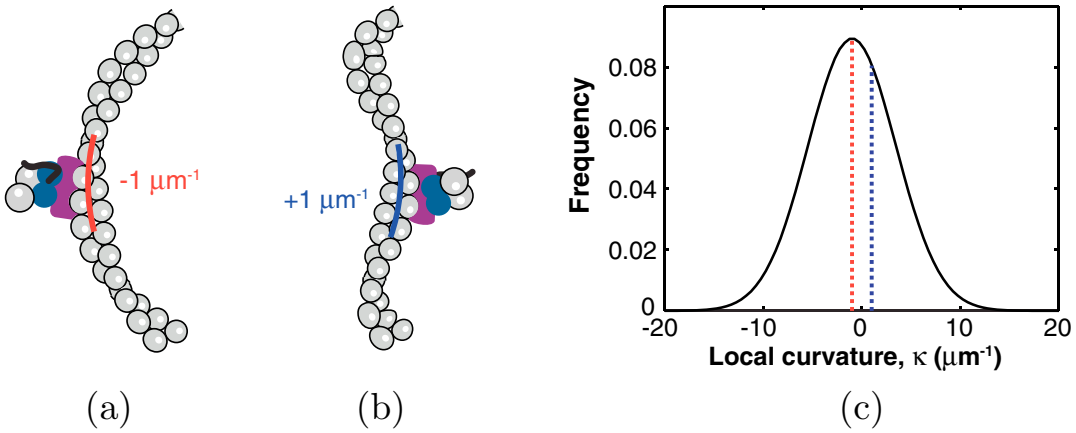

Figure 3.6: **Curvature fluctuations of a single constrained filament.** (a) Schematic representation of the imposed curvature (shown by red arc) of a segment of an actin filament, which is concave to the right in this case. (b) A shape fluctuation of the filament can transiently give rise to the same local curvature, but with opposite concavity (blue arc). A state in which the NPF- and G-actin-bound Arp2/3 complex is bound to the left side of the filament in *a* has the same energy as the ternary complex bound to the right side of the filament in *b*, because the microscopic curvature is locally the same. Therefore, the total probability of the Arp2/3 complex being bound to the right or left side of the filament depends only on the relative likelihood of states *a* and *b*. (c) Distribution of local curvatures on a simulated filament with imposed curvature κ_0 = -1 μm^{-1} (choosing the coordinate system arbitrarily). The average curvature does not fully describe the shape of the filament as encountered by the Arp2/3 complex. The likelihood of that location on the filament having the same local curvature as the imposed mean curvature (red line, state depicted in *a*) is only 10% larger than its likelihood having the curvature of opposite concavity, and hence opposite sign (blue line, state depicted in *b*). For comparison, the experimental results (Fig. 3.3) showed 99% more branching on the convex side than on the concave side.

3.4.2 A fluctuation gating model for branching by the Arp2/3 complex is consistent with the experimental data

Two lines of evidence support the hypothesis that curvature regulates branch nucleation kinetics. First, the Arp2/3 complex binds F-actin in solution with a slow on-rate, perhaps because it must wait for a favorable structural fluctuation of the filament [8]. Second, a structural model of the Arp2/3-actin branch shows a local distortion involving subdomain 2 of an actin monomer at the Arp2/3 binding site [23]. Extensional strain could weaken

longitudinal intermonomer contacts in F-actin, helping to stabilize a transition state with high local curvature and increasing the kinetic rate of either Arp2/3 binding or branch nucleation.

Based on this evidence, we developed a filament fluctuation gating model, conceptually similar to fluctuation-gated binding of ligands to proteins [74]. In our model, stable Arp2/3 ternary complex binding and branch nucleation occur only when the local curvature of the filament fluctuates beyond a threshold value κ (Fig. 3.7). A sharp threshold is chosen because in the extreme wings of the local curvature distribution, probability attenuates so rapidly that the only pertinent model parameter is the lowest curvature value where branching is greatly enhanced, in effect, κ_{th}. Thus, the probability that a branch forms on either side of the curved filament under our model is the net probability of respective curvature values in excess of $+\kappa_{th}$ or $-\kappa_{th}$ (Fig. 3.8a). Based on this idea, we can calculate a relative branch density using

$$P^{rel,-}_{branch}(\kappa_{th},\kappa_0) = \frac{P_{\kappa_0=\kappa_i}(\kappa < \kappa_{th})}{P_{\kappa_0=0}(\kappa < \kappa_{th})},\ P^{rel,+}_{branch}(\kappa_{th},\kappa_0) = \frac{P_{\kappa_0=\kappa_i}(\kappa > \kappa_{th})}{P_{\kappa_0=0}(\kappa > \kappa_{th})}, \tag{3.1}$$

where κ_{th} is the threshold curvature, κ_0 is the imposed curvature, and κ_i is a value for the imposed curvature $\neq 0$. The predictions generated from these results can then be compared directly with experimental results for the relative branch density (Fig. 3.3d). Our calculations assess how extreme the curvature threshold κ_{th} needs to be in order to account for the curvature preference we observe experimentally.

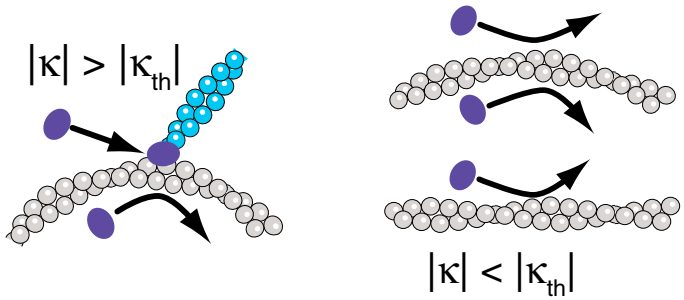

Figure 3.7: **Fluctuation gating model.** (a) The fluctuation gating model predicts a threshold convex local curvature beyond which stable binding and branching by the Arp2/3 complex (violet) can occur. (b) Below that threshold curvature, binding and branching do not occur.

With these simple assumptions, the fluctuation gating model captures the shape of the curvature-dependent branching bias and agrees quantitatively with our data over the entire experimental range for a value of $\kappa_{th} = 5\ \mu\text{m}^{-1}$ (red curve, Figs. 3.3d and 3.8b). These results are consistent with a mechanism in which F-actin bending fluctuations play a role

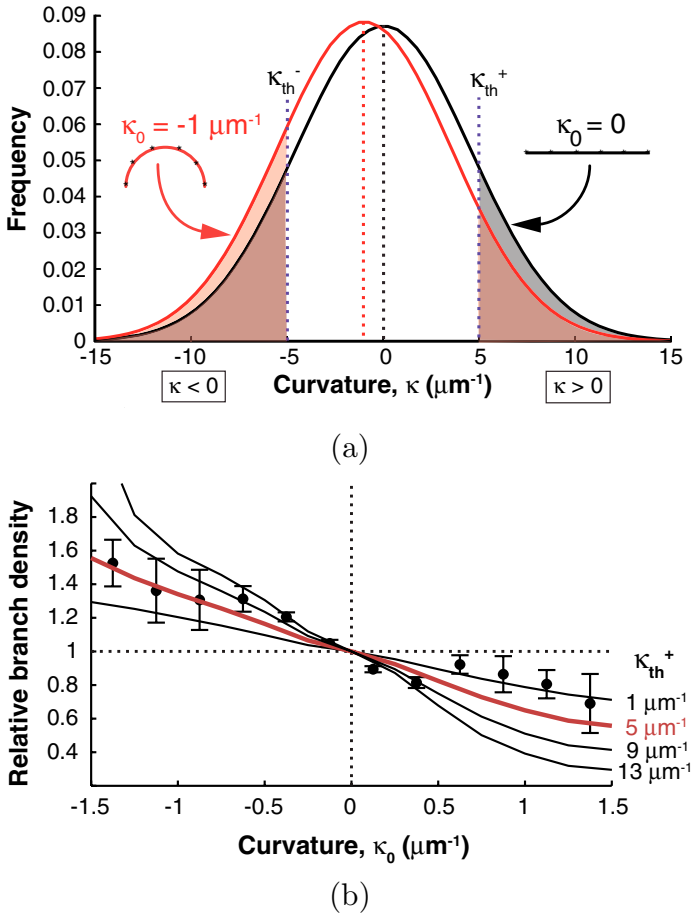

Figure 3.8: **Fluctuation gating model predictions.** (a) Distribution of local curvature fluctuations for a filament tethered to a straight (black) or curved (red) path. Shaded areas indicate probability of branching. (b) Relative branch density calculated from the ratio of the red- and black-shaded areas for several values of κ_{th} plotted with experimental data.

in regulating branch formation by the Arp2/3 complex, suggesting that branching can be regulated by alterations of bending fluctuations of filaments due to constraints on actin network architecture or by binding of other ABPs. However, because of its coarse-grained resolution, this model cannot make predictions about conformational changes of the actin monomer caused by bending in the Arp2/3 binding site on the scale of individual amino acid residues. This model is presented in the simplest form that is consistent with our data and experimental parameters, but it could be extended to include details about the dependence of branch direction on curvature based on future findings. For example, we currently have little data in the very high convex curvature regime, where the branch density may decrease as the curvature distorts the mother filament to such an extent that it can no longer accommodate branch nucleation.

3.4.3 Autocatalytic branching amplifies the branching bias

Directionally biased branching has important implications for branched actin assembly in vivo, where autocatalytic nucleation amplifies small effects [92, 14]. A large fraction of filaments in a branched actin network adopt an approximately 35° orientation [22], and the side of a bent filament experiencing extensional strain is the same side that typically faces the bending force. Excess growth on the convex side of the curved filament would therefore create more branches oriented toward the bending force, reinforcing the branched network (Fig. 3.9a). The excess of branches on the most convex side of the mother filament may also define a preferred plane for branching that coincides with the plane of filament curvature, possibly contributing to the flat and thin shape of lamellipodia. It would also lead to more filaments growing into the membrane-adjacent zone where new branches can be nucleated, increasing total branch density. We studied this effect with a different, stochastic simulation of branching in two dimensions (Fig. 3.9b) and found that, for a 15% bias toward the membrane, the total number of filaments is double that of the zero bias case after only 10 branch generations (Fig. 3.9b). Based on our experimental data (Fig. 3.3d), a 15% curvature bias corresponds to a radius of curvature of 2.3 μm and a bending energy of 0.6 k_BT per μm of ATP-bound filament [57]. This amount of curvature could result from a lateral force of 1 pN applied perpendicularly to the end of a 0.05 μm-long filament fixed at the other end [7], which reflects the average force per filament due to membrane tension and rigidity [1, 80] and the approximate length of free F-actin [119] at the leading edge of the cell. If the length of free F-actin is longer at the leading edge [127, 111], the filaments require even less force to bend. Therefore, even modest filament curvature that is caused by the normal force balance of branched actin growth against a membrane can generate a significant bias in the direction of actin branch nucleation.

3.5 Conclusions

We have shown that F-actin curvature regulates Arp2/3 complex activity, providing the cell with a distributed, filament-dependent mechanism for sensing and responding to the compressive stress on branched actin networks. Our results suggest the possibility that mechanical stress on cytoskeletal filaments can modulate how they interact with their binding partners. The actin filament takes on a diversity of structural states as it grows, interacts with binding proteins, encounters physical constraints, and fluctuates due to thermal motion [65, 104]. It is likely that other side-binding ABPs besides the Arp2/3 complex exhibit similar sensitivity to local actin curvature, providing a direct mechanism for altering organization of the actin cytoskeleton in response to force. For example, filament severing by the ADF/cofilin homolog actophorin occurs more readily at points of high curvature [68], consistent with a recently elucidated mechanism for severing by cofilin that depends on a mechanism that takes advantage of the mechanical instability at the border between two structural states of F-actin [76]. However, it is not yet known whether cofilin binding or the cooperativity

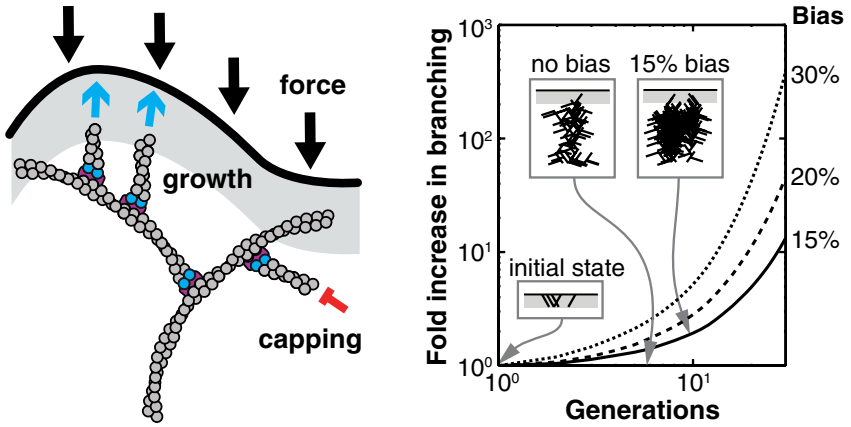

(a) (b)

Figure 3.9: **A bias in the direction of branching can increase the total amount of actin in a branched network.** (a) In a branched network, compressive forces bend filaments away from the membrane (black). Excess branching on the convex side of a bent filament creates more branches pointing toward the membrane, increasing the number of filaments pushing against the membrane (cyan blue arrows). Capping (red) can occur anywhere, but filaments can only branch in the branching zone (gray). (b) Results of a stochastic branching simulation in which rigid branches with angles of ±36° and -108° grow with a given bias (right column) toward the membrane. (*Insets*) Schematic snapshots of branching with 0% and 15% bias (gray, branching zone).

of cofilin binding is affected by local filament curvature, although it has been shown that its binding lowers the persistence length of actin [75] and that its binding is enhanced by tension on F-actin [50]. Nor have other proteins that modify the persistence length of actin, such as drebrin [109] or tropomyosin [57], been tested for sensitivity to F-actin curvature. The methods we have developed can be used as a platform to investigate the curvature dependence of other ABP-filament interactions and the role of actin filament bending in mechanotransduction and cytoskeletal reorganization.

Chapter 4

Curvature dependent force sensing

The work described in this chapter was performed in collaboration with Julian Weichsel, Viviana Risca, and Professor Daniel Fletcher.

Cytoskeletal filaments and the plasma membrane participate in a broad range of essential and disparate cellular processes. Their physical environment subjects them to a range of mechanical cues, including tensile forces. Results from chapter 3 and elsewhere in the literature suggest that changes in curvature fluctuations of filaments and membranes induced by such forces are likely to play an important role in regulating protein binding. A problem inherent in studying how forces affect protein binding is the large difference in length scale between the systems' micrometer-scale properties measured in experiment and the nanometer conformational changes that determine the interaction with proteins.

This nanometer-scale curvature of cytoskeletal filaments or the plasma membrane, however, is readily accessible for well established mesoscale models without requiring atomistic detail. In this chapter, we present a framework for accessing nanometer-scale curvature without simulation. More specifically, we derive analytical expressions for the nanometer-scale curvature distribution of a worm-like chain and membrane as a function of applied tension. These results agree well with curvature distributions calculated in Monte Carlo simulations of a discretized worm-like chain and a triangulated membrane sheet. We also discuss how these results can be used to understand the force dependence of protein binding to actin filaments and membranes within the biological context. Our findings are generally applicable to semiflexible polymers such as actin and DNA, as well as membranes such as the plasma membrane and endosomes.

4.1 Introduction

A central challenge in actin research is understanding how the actin network dynamics observable by light microscopy arise from molecular interactions [94]. This task is made more difficult by the fact that mechanical force, produced by extracellular sources and intracellular

myosin motors, acts on actin networks to constrain and modulate the biochemical reactions that govern their mechanical properties and dynamics [32, 53]. The transduction of force into biochemical signals has been extensively studied in the context of specialized mechanosensing molecules [129], but new evidence suggests that mechanosensitivity also rests in actin filaments themselves and in their interactions with regulatory proteins [36, 50, 110, 128]. Actin filaments have been demonstrated to be highly polymorphic [37, 108], and their conformation can be modulated both by ABPs [38] and by applied forces [36, 110]. Modulation of protein binding to actin by filament curvature [105] or applied force [50, 128] has also been demonstrated.

In membrane biophysics research, the relationship between protein binding and curvature has been much more extensively studied. It has been found that proteins can induce membrane curvature through scaffolding, helix-insertion, and crowding mechanisms [6, 114]. Additionally, many experiments have identified and characterized proteins that preferentially bind to highly curved membranes [10, 88]. Several characteristics of these proteins have been proposed to underlie such curvature sensing [3]. For example, proteins containing crescent-shaped BAR (BinAmphiphysinRvs) domains sense curvature by binding to membranes along the inner face of its arc. ALPS (Amphipathic Lipid Packing Sensor) motifs are intrinsically unstructured and have been shown to preferentially bind to lipid packing defects that are more probable on curved surfaces. Another aspect of membrane mechanics that may regulate protein binding is membrane tension. Although progress has been made regarding the effect of tension on cell polarity and motility [55, 5], it remains unclear how this might affect the protein binding by altering curvature fluctuations.

The complex relationship between macroscopic constraints and microscopic structure presents a problem in understanding how forces affect protein binding. Binding relies on the atomic-scale conformation and fluctuations, while forces affect biological systems at all length scales. One parameter that has the potential to bridge the disparate length scales of actin and membrane networks and proteins is curvature. In both cases, there is experimental evidence showing a clear dependence of protein binding on the curvature [105, 88]. Here, we derive and simulate the nanometer-scale curvature distribution of WLC (Sec. 4.2.1) and triangulated membrane sheet (Sec. 4.2.3) under tension. The expressions we derive for curvature distributions as a function of force are generally applicable to other semiflexible polymers that can be modeled by the WLC as well as different types of biological membranes.

4.2 Results

4.2.1 Curvature distribution of a WLC under tension

The energy of a free WLC is

$$E = k_B T \int_0^L \frac{l_p}{2} \kappa(s)^2 ds. \tag{4.1}$$

L is the contour length, l_p is the persistence length, s is the arc length, and κ is the local curvature, defined as

$$\kappa(s) = \left| \frac{\partial \mathbf{t}(s)}{\partial s} \right|, \tag{4.2}$$

where $\mathbf{t}(s) = \partial \mathbf{r}(s)/\partial s$ is the unit tangent vector along the contour of the chain. The curvature distribution for a single component (in the following called x or y) is Gaussian,

$$P(\kappa_x)d\kappa \propto e^{-\kappa_x^2/2\sigma_x^2}, \tag{4.3}$$

where σ_x^2 is the variance of a single Cartesian component of the curvature vector. For a free filament, the variance of this distribution is

$$\sigma_x^2 = \frac{1}{l_p \Delta s}. \tag{4.4}$$

We are more interested in the probability distribution for the magnitude of the total curvature, because the total curvature is useful as a parameter that can approximate the distortions of the WLC. The probability distribution for the total curvature is [101]

$$P(\kappa)d\kappa \propto \kappa e^{\frac{-\kappa^2}{2\sigma_x^2}} d\kappa. \tag{4.5}$$

The variance of the total curvature distribution is

$$\sigma^2 = 2\sigma_x^2 = \frac{2}{l_p \Delta s}. \tag{4.6}$$

It is important to note that the variance is finite only for $\Delta s \neq 0$. However, because our framework intended for accessing curvature on a length scale commensurate with that of protein binding (nanometer-scale), this condition will always be satisfied for biologically relevant problems. Under tension, the variance of the distribution changes. In order to derive an expression for this variance as a function of applied tension, we start with the Hamiltonian of a WLC under tension

$$E = k_B T \int_0^L \frac{l_p}{2} \kappa^2 ds - fz, \tag{4.7}$$

where f is the tensile force applied to the end-to-end axis of the chain (z axis).

Under moderate tension, the tangent vector of the chain fluctuates very little around the z axis, allowing us to make a small curvature approximation in which we approximate the overall curvature $\kappa \approx \kappa_\perp$ as a sum of the x and y component curvatures

$$\kappa \approx \kappa_\perp = \kappa_x + \kappa_y. \tag{4.8}$$

Using this approximation, we can rewrite the Hamiltonian as

$$E = \frac{1}{2} \int_0^L \left[k_B T \, l_p \left| \frac{\partial \mathbf{t}_\perp}{\partial s} \right|^2 + f \mathbf{t}_\perp^2 \right] ds - fL. \tag{4.9}$$

The tangent vector and its derivative can be decomposed in their respective Fourier series,

$$\mathbf{t}_\perp(s) = \frac{1}{L}\sum_q \hat{\mathbf{t}}_\perp(q)\, e^{iqs} \approx \int \frac{dq}{2\pi}\, \hat{\mathbf{t}}_\perp(q)\, e^{iqs} \tag{4.10}$$

$$\frac{\partial \mathbf{t}_\perp}{\partial s} = \frac{1}{L}\sum_q \hat{\mathbf{t}}_\perp(q)\, iq\, e^{iqs} \approx \int \frac{dq}{2\pi}\, \hat{\mathbf{t}}_\perp(q)\, iq\, e^{iqs}, \tag{4.11}$$

where the limits of integration are determined by the maximum and minimum wave vectors corresponding to a chain of contour length L and discretization Δs ($q_{max} = \pi/\Delta s$, $q_{min} = \pi/L$). Since the curvature is real-valued, the Fourier coefficients have the property that $\hat{\mathbf{t}}_\perp(-q) = \hat{\mathbf{t}}^*_\perp(q)$. Thus, the Fourier representation of the energy is

$$E = \frac{1}{2L}\sum_{\mathbf{q}} \left(k_B T\, l_p\, q^2 + f\right) |\hat{\mathbf{t}}_\perp(q)|^2 - fL, \tag{4.12}$$

Each Fourier mode has energy $k_BT/2$ by equipartition and we find that

$$\langle |\hat{\mathbf{t}}_\perp(q)|^2\rangle = 2\langle |\hat{\mathbf{t}}_x(q)|^2\rangle = \frac{2L}{l_p\, q^2 + f/k_BT}. \tag{4.13}$$

The variance of a single Cartesian component of the curvature vector is given by,

$$\begin{aligned}
\sigma_x^2 = \langle \left|\frac{\partial t_x}{\partial s}\right|^2 \rangle &= \langle \int \frac{dq}{2\pi} e^{iqs}(iq)\hat{\mathbf{t}}_x(q) \int \frac{dq'}{2\pi} e^{iq's}(iq')\hat{\mathbf{t}}_x(q')\rangle \\
&= \frac{1}{L}\int ds \int \frac{dq}{2\pi} e^{iqs}(iq)\hat{\mathbf{t}}_x(q) \int \frac{dq'}{2\pi} e^{iq's}(iq')\hat{\mathbf{t}}_x(q') \\
&= \frac{1}{L}\int \frac{dq}{2\pi} q^2 \langle |\hat{\mathbf{t}}_x(q)|^2\rangle \\
&= \int \frac{dq}{2\pi} \frac{q^2}{l_p\, q^2 + f/k_BT}.
\end{aligned} \tag{4.14}$$

The limits of integration are determined by the maximum and minimum wave vectors,

$$\begin{aligned}
\sigma_x^2 = \langle \left(\frac{\partial t_x}{\partial s}\right)^2 \rangle &= \int_{-\pi/\Delta s}^{-\pi/L} \frac{dq}{2\pi} \frac{q^2}{l_p\, q^2 + f/k_BT} + \int_{\pi/L}^{\pi/\Delta s} \frac{dq}{2\pi} \frac{q^2}{l_p\, q^2 + f/k_BT} \\
&\approx \int_{-\pi/\Delta s}^{\pi/\Delta s} \frac{dq}{2\pi} \frac{q^2}{l_p\, q^2 + f/k_BT} \quad \text{for large } L \\
&= \frac{1}{l_p \Delta s} - \frac{\sqrt{f/k_BT}}{2l_p^{3/2}}.
\end{aligned} \tag{4.15}$$

We compared this analytical result with Monte Carlo simulations of a WLC with discretization length Δs. For both the curvature distribution at fixed tensile force (Fig. 4.1 c and d)

and the variance of the curvature as a function of tension (Fig. 4.1f), we find good agreement between theory and simulation. It is important to note that in Fig. 4.1f, we are plotting the second moment of the total curvature distribution, which relates to the variance of distribution for each component as

$$\sigma^2 = 2\sigma_x^2 = 2\left(\frac{1}{l_p \Delta s} - \frac{\sqrt{f/k_B T}}{2 l_p^{3/2}}\right). \tag{4.16}$$

The snapshots in Fig. 4.1 a and b illustrate the effect of tension on the fluctuations at different length scales. Applying 30 pN of tension substantially changes the large wavelength fluctuations compared to that of a tensionless chain, but the effect on the smaller wavelengths fluctuations (zoomed-in view) on the contrary are very subtle. In Fig. 4.1e, we see how the curvature distribution changes as a function of tension. The range of forces was chosen to reflect the tensions to which actin filaments are subjected in the biological context, for instance in stress fibers, which are contractile elements present in many cell types, and in *in vitro* experiments. On the lower end of that range, 30 pN corresponds to the stall force of 7-10 myosin motors [30] and to the force applied to actin in an experiment measuring the impact of tension on cofilin binding [50]. The upper end of the range is based on measurements of the traction forces applied by single focal adhesions that couple to single stress fibers (approximately 4 nN) [4, 121] and on the number of actin filaments in a stress fiber or a similar contractile bundle (tens) [19].

4.2.2 Curvature distribution of a WLC under compression

We follow a very similar strategy to derive expressions for the curvature distribution of a WLC under compression. The variance of a single Cartesian component of the curvature vector is given by,

$$\sigma_x^2 = \langle \left(\frac{\partial t_x}{\partial s}\right)^2 \rangle = \frac{1}{l_p \Delta s} + \frac{\sqrt{f/k_B T}}{\pi l_p^{3/2}} \coth^{-1}\left[\frac{\pi \sqrt{l_p}}{L\sqrt{f/k_B T}}\right] \tag{4.17}$$

The inverse hyperbolic cotangent term becomes undefined at $f = l_p \pi^2 / L_c^2$, which is the buckling force. The accuracy of the analytical solution decreases rapidly for increasing compression force because the small angle approximation no longer holds at even modest forces. For a WLC with $L = 0.5$ μm and $l_p = 9$ μm, the buckling force is approximately 1.48 pN. The analytical solution is only accurate below ~ 0.5 pN, where the curvature distribution changes very little from that of the free filament.

4.2.3 Curvature distribution of a membrane under tension

Consider a nearly flat piece of membrane. Within the Monge gauge, the surface shape is parametrized by its height field $h \equiv h(\mathbf{r})$ with respect to its two dimensional reference plane

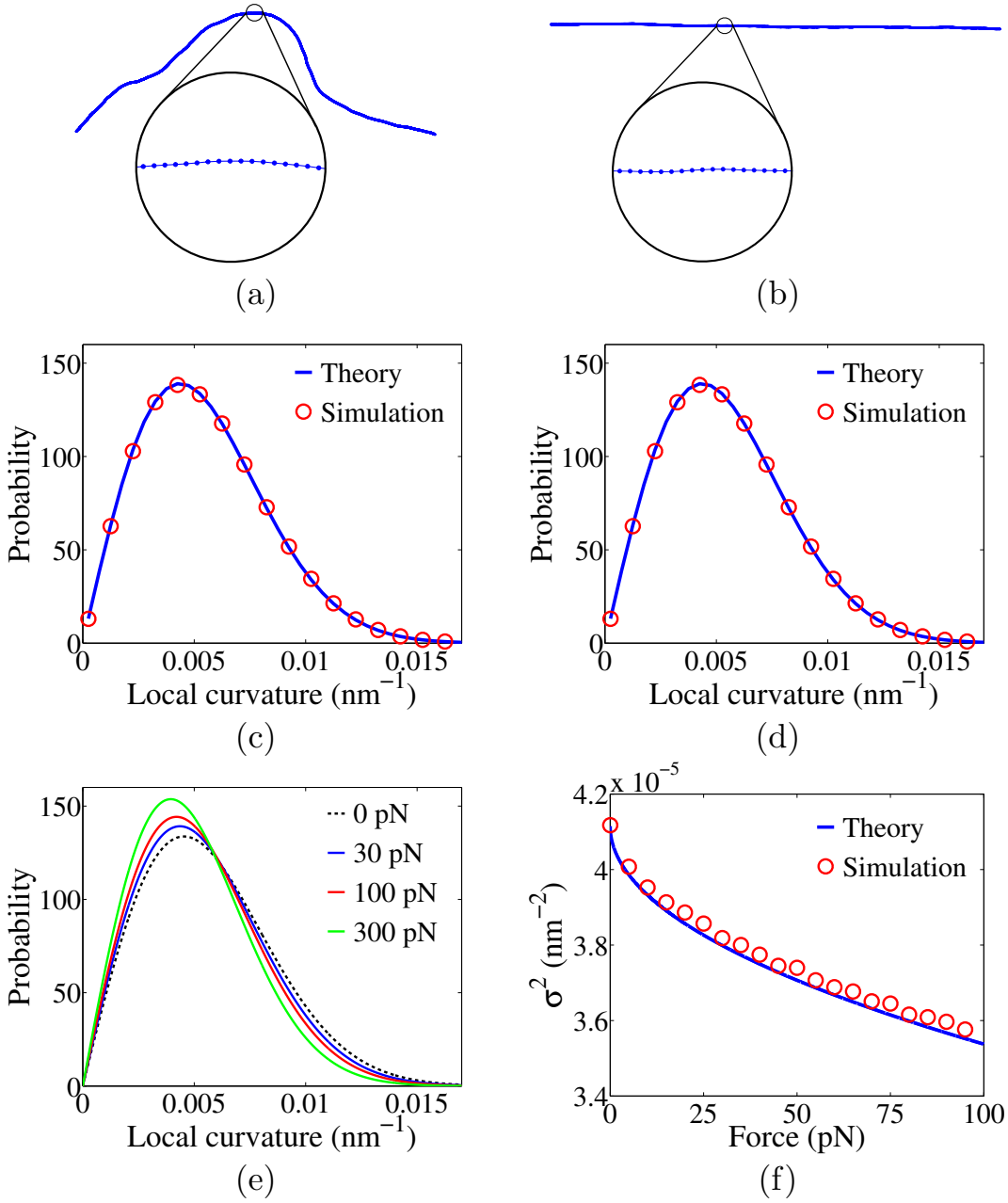

Figure 4.1: **Worm-like chain under tension.** Snapshots of a WLC simulation corresponding to a chain with contour length $L_c = 9$ μm and persistence length $L_p = 9$ μm (zoomed-in section $\sim$0.09 μm) under (a) 0 pN and (b) 30 pN of tension from simulation. Comparisons of analytical theory and WLC simulation corresponding to a chain with $L_c = 0.5$ μm and $L_p = 9$ μm. Curvature distribution under (c) 30 pN and (d) 100 pN of tension obtained using both the theoretical prediction and simulation. (e) Curvature distribution of a simulated WLC under a range of tensile forces ranging from 0 to 300 pN. (f) Variance of the total curvature under tension.

$\mathbf{r} \equiv (x, y)$ of size L^2. Additionally using a small gradient approximation (i.e. $|\nabla h| \ll 1$), the membrane energy can be written as,

$$E = \int_{L^2} d^2x \left[\frac{k_c}{2} \left(\nabla^2 h \right)^2 + \frac{\gamma}{2} \left(\nabla h \right)^2 \right], \tag{4.18}$$

with bending modulus k_c and surface tension γ. The mean curvature distribution is Gaussian,

$$P\left(\nabla^2 h\right) d\nabla^2 h \propto e^{-\frac{(\nabla^2 h)^2}{2\sigma^2}} d\nabla^2 h. \tag{4.19}$$

For a large tensionless membrane ($\gamma = 0$), the variance of this distribution is,

$$\sigma^2 = \langle \left(\nabla^2 h \right)^2 \rangle = \frac{k_B T}{k_c \delta x^2}, \tag{4.20}$$

where the length δx indicates some finite discretization in x, y. To derive the width of the distribution for the general case ($\gamma \geq 0$), we start with the Fourier transform of the energy. Using the definition of the Fourier transform of the membrane height h,

$$h(\mathbf{r}) = \frac{1}{L^2} \sum_{\mathbf{q}} \hat{h}(\mathbf{q}) \, e^{i\mathbf{q}\mathbf{r}} \approx \int \frac{d\mathbf{q}}{(2\pi)^2} \, \hat{h}(\mathbf{q}) \, e^{i\mathbf{q}\mathbf{r}} \tag{4.21}$$

$$\nabla h(\mathbf{r}) = \frac{1}{L^2} \sum_{\mathbf{q}} \hat{h}(\mathbf{q}) \, (i\mathbf{q}) \, e^{i\mathbf{q}\mathbf{r}} \approx \int \frac{d\mathbf{q}}{(2\pi)^2} \, \hat{h}(\mathbf{q}) \, (i\mathbf{q}) \, e^{i\mathbf{q}\mathbf{r}} \tag{4.22}$$

$$\nabla^2 h(\mathbf{r}) = \frac{1}{L^2} \sum_{\mathbf{q}} \hat{h}(\mathbf{q}) \, (i\mathbf{q})^2 \, e^{i\mathbf{q}\mathbf{r}} \approx \int \frac{d\mathbf{q}}{(2\pi)^2} \, \hat{h}(\mathbf{q}) \, (i\mathbf{q})^2 \, e^{i\mathbf{q}\mathbf{r}} \tag{4.23}$$

$$\tag{4.24}$$

in Eq. 4.18 leads to,

$$\beta E = \frac{1}{2L^2} \sum_{\mathbf{q}} \left(k_c \mathbf{q}^4 + \gamma \mathbf{q}^2 \right) |\hat{h}(\mathbf{q})|^2, \tag{4.25}$$

which directly indicates,

$$\langle |\hat{h}(\mathbf{q})|^2 \rangle = \frac{k_B T L^2}{k_c \mathbf{q}^4 + \gamma \mathbf{q}^2}, \tag{4.26}$$

due to equipartition. The variance of the mean curvature distribution is therefore given by,

$$\sigma^2 = \langle \left(\nabla^2 h\right)^2 \rangle = \langle \int \frac{\hat{h}(\mathbf{q})}{(2\pi)^2} (i\mathbf{q})^2 e^{i\mathbf{qr}} d\mathbf{q} \int \frac{\hat{h}(\mathbf{q}')}{(2\pi)^2} (i\mathbf{q}')^2 e^{i\mathbf{q}'\mathbf{r}} d\mathbf{q}' \rangle \tag{4.27}$$

$$= \frac{1}{L^2} \int dx^2 \int \frac{\hat{h}(\mathbf{q})}{(2\pi)^2} (i\mathbf{q})^2 e^{i\mathbf{qr}} d\mathbf{q} \int \frac{\hat{h}(\mathbf{q}')}{(2\pi)^2} (i\mathbf{q}')^2 e^{i\mathbf{q}'\mathbf{r}} d\mathbf{q}' \tag{4.28}$$

$$= \frac{1}{L^2} \int \frac{d\mathbf{q}}{(2\pi)^2} \mathbf{q}^4 \langle |\hat{h}(\mathbf{q})|^2 \rangle \tag{4.29}$$

$$= \frac{k_B T}{(2\pi)^2} \int \mathrm{d}^2\mathbf{q} \frac{\mathbf{q}^4}{k_c \mathbf{q}^4 + \gamma \mathbf{q}^2} \tag{4.30}$$

$$= \frac{k_B T}{(2\pi)^2 k_c} \left(\int \mathrm{d}^2\mathbf{q} - \int \mathrm{d}^2\mathbf{q} \frac{\gamma}{k_c \mathbf{q}^2 + \gamma} \right) . \tag{4.31}$$

Here we have approximated the two sums (each with discretization $\Delta q_{x,y} = 2\pi/L$) by integrals in the first step and used $\int \mathrm{d}^2x\, e^{i\vec{r}(\vec{q}+\vec{q}')} = (2\pi)^2 \delta(\vec{q}+\vec{q}')$ and Eq. 4.26 subsequently. In the last step, the integral was additionally separated into tension-independent and -dependent parts. The limits for the integrations are determined by the minimum and maximum wave vector cutoffs q_{min} and q_{max}. For a periodic membrane sheet of finite linear extension L, the smallest possible mode is $q_{min} = 2\pi/L$. This is negligible at sufficiently large L (i.e. $q_{min} \simeq 0$). The maximum mode is determined by the discretization of the membrane (i.e. in the extreme case by the size of a single lipid), $q_{max} = \pi/\delta x$. Using these limits, the tension-independent part of Eq. 4.31 can be readily integrated in Cartesian coordinates, while we will approximate the integration of the tension-dependent term in polar coordinates (i.e. $\mathrm{d}^2q \approx 2\pi q \mathrm{d}q$). The variance of the curvature distribution is thus given by,

$$\sigma^2 \approx k_B T \left[\frac{1}{k_c \delta x^2} - \frac{\gamma}{4\pi k_c^2} \ln \left(\frac{\pi^2 k_c}{\delta x^2 \gamma} + 1 \right) \right] \quad \text{for large } L\,. \tag{4.32}$$

Note that Eq. 4.32 also includes the limiting case $\gamma \to 0$,

$$\lim_{\gamma \to 0} \sigma^2 = \frac{k_B T}{k_c \delta x^2}\,. \tag{4.33}$$

Fig. 4.2 shows comparisons of the mean curvature distribution from simulation to analytical theory. The results are in good agreement for curvature distributions (Fig. 4.2 c and d) at fixed surface tensions and for the variance of the distributions (Fig. 4.2f).

4.3 Computational methods

4.3.1 Worm-like chain

To test and verify the analytical results, we performed Monte Carlo simulations of a discretized WLC under tension and compression. We start with a model of a free WLC whose

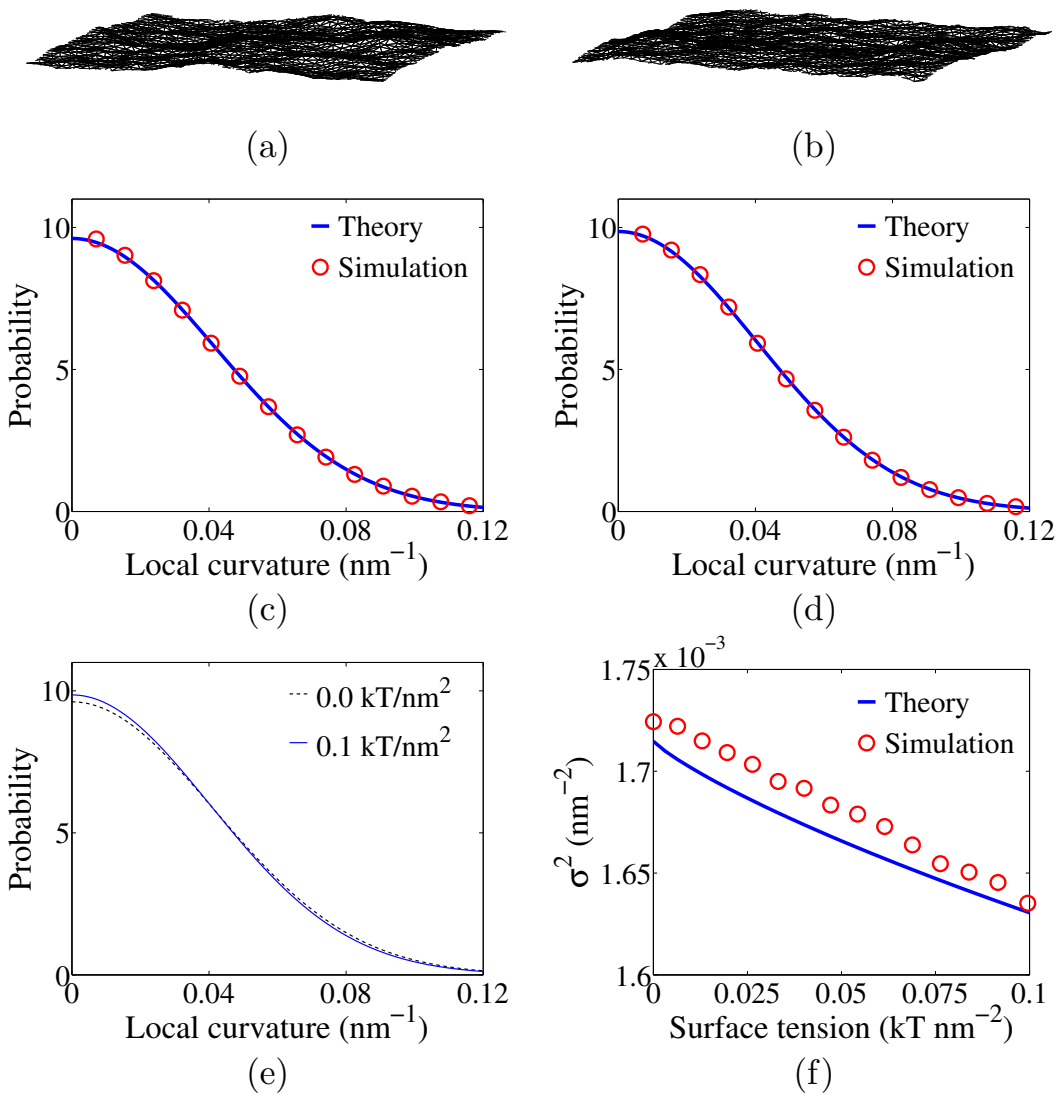

Figure 4.2: **Membrane sheet under tension.** Representative snapshots of a triangulated membrane sheet under (a) 0 and (b) 0.1 k_BT/nm^2 surface tension. Comparisons of analytical theory and simulation corresponding to a membrane with bending modulus $k_c = 20\ k_BT$. Curvature distribution under (c) 0 and (d) 0.1 k_BT/nm^2 of surface tension obtained using both the theoretical prediction and simulation. (e) Comparison of the curvature distribution for surface tensions 0 and 0.1 k_BT/nm^2. (f) Variance of the total curvature under surface tension.

coarse-graining resolution and energetics are detailed in 2. We then apply a force to the end-to-end vector $\mathbf{R}$ of the WLC. If we align the end-to-end vector of the chain on the z-axis, the energy attributed to the force f can be written as

$$\beta E_{force} = \beta f z. \tag{4.34}$$

The total energy of our WLC under force is then simply the sum of the bending energies and the applied force

$$\beta E_{total} = \beta E_{bend} + \beta E_{force} = \frac{1}{2}\sum_{i}^{N} l_p |\kappa_i|^2 \Delta s + \beta f z. \tag{4.35}$$

Conformational fluctuations are sampled using the standard Metropolis Monte Carlo algorithm.

4.3.2 Triangulated membrane sheet

In order to test our analytical approximation for the curvature distribution of a membrane under tension, we rely on a widely used dynamically triangulated surface model for fluctuating fluid membranes [52, 47]. We are simulating a quasi-flat periodically continued membrane interface employing a Metropolis Monte Carlo method. The bending energy as well as the local curvature of the membrane is evaluated using a discretized version of the Laplacian on the triangulated lattice as described in [47]. A constant surface tension is prescribed by allowing the simulation box to fluctuate and biasing the acceptance of these moves accordingly [112].

4.4 Biological implications

These results can be interpreted in the context of protein binding to semiflexible filaments like actin or membranes such as the plasma membrane. In a simple model of binding, we assume that nanometer- and angstrom-scale conformation in the filament correlates with its local curvature as it undergoes Brownian fluctuations [105]. In the simplest case, only a window of permissive local curvature allows for protein binding (Fig. 4.3). The window is defined by a threshold curvature κ_{th}. Only sections of the filament or membrane whose instantaneous curvature is in the permissive window take on a conformation that allows binding, while other sections with non-permissive curvature do not result in productive collisions. This model is conceptually similar to the gated ligand binding model developed by McCammon and Northurp [74]. By integrating the area under the curvature probability distribution Eqs. (4.5) and (4.19) within the binding window (in this case, above the threshold curvature), we can calculate the fraction of the filament or membrane that adopts permissive curvature at any time, or, equivalently, the fraction of the time that any section of filament or membrane adopts permissive curvature for binding.

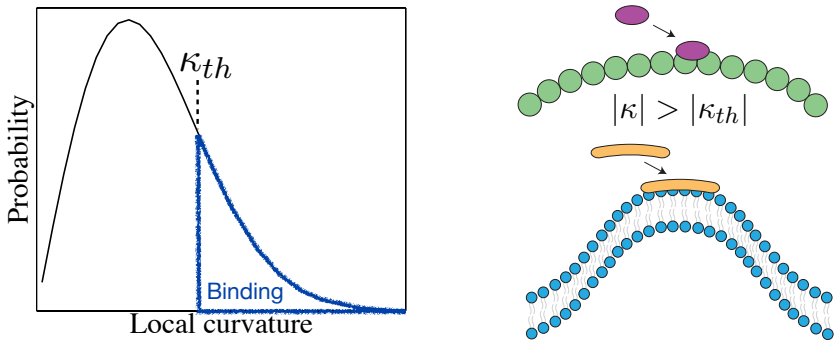

(a) (b)

Figure 4.3: **Biological implications.** Possible application of our analytical expressions for the curvature distribution of WLCs and membranes under tension to the interaction with proteins. (a) A window of permissive values of the transient local curvature of the filament or membrane allows for protein binding. The window is defined by a threshold curvature κ_{th}. The area under the curve above κ_{th} represents the probability of protein binding or activity. (b) Only sections of the filament or membrane whose instantaneous curvature is in the permissive window take on a conformation that allows binding, while other sections with non-permissive curvature do not result in productive collisions.

4.5 Conclusions

Here, we have derived simple analytical expressions for the curvature distribution of WLCs and membranes as a function of tensile forces. Tension on actin filaments and membranes is not only common in the cellular environment, but is also likely to give rise to significant changes in curvature fluctuations. Our model, coupled with emerging models of how proteins interact with filaments and membranes, may provide a useful bridge between the micron-scale network mechanical processes and nanometer-scale protein-protein interactions. Our result, combined with more specific models describing the interaction between the proteins and filament or membrane, can potentially be used to explain specific mechanisms by which tension regulates protein binding affinity. Furthermore, our results can motivate new experiments in this context, seeking to identify proteins that interact with cytoskeletal filaments or membranes in a mechanosensitive curvature sensing way.

Part II

Network level

Chapter 5

Simulating soft materials under stress

The work described in this chapter was performed in collaboration with Sander Pronk.

Thus far, we have examined how forces affect actin at the single filament level. In this and the next chapter, we shift to a larger length scale and investigate how actin networks respond to large external stresses. In particular, because actin networks exhibit a very nonlinear elastic response, our goal is to better understand the properties and structures that give rise to the bulk properties responsible for maintaining the structural integrity of cells in a mechanically stressed environment. Although there exist computational methods for probing the properties of linearly elastic materials [86], there is currently no computational method to accurately apply stress to nonlinearly elastic materials. Therefore, before we can investigate the behavior of an actin network under stress, we need to develop a framework to do so. In this chapter, we present a constant stress method to accurately apply stress to nonlinearly elastic materials. Additionally, we develop a toy model of a soft elastic solid with a nonlinear elastic response to test our method.

5.1 Introduction

Many interesting biologically important materials are soft. They exhibit substantial deformations as a result of moderate stresses, despite consisting of particles that interact through strong repulsions or attractions, for instance, hard-sphere repulsions and short-range attractions in colloidal systems [100, 27], and strongly cross-linked stiff polymers in many mechanically active biological systems [11].

In order to measure elastic properties in these systems, it can be numerically infeasible to calculate the stress directly using the virial stress equation, which depends on the derivative of the interaction potential [33]. Instead, the strain can be allowed to fluctuate by sampling the simulation box shape.

Such strain fluctuation methods, as first described by Parrinello and Rahman [86], are among the earliest uses of fluctuations as measure for thermodynamic quantities in computer

simulations: the fluctuations of the matrix that determines the simulation box shape are inversely proportional to the elastic constants obtained from a single simulation. This method was later made rigorously correct in the case of large imposed stress [102, 103] by applying finite-deformation elasticity theory [131, 132]. By 'large stress' we mean a stress that leads to a non-negligible strain, including isotropic pressures that lead to compression of an otherwise non-interacting gas.

In this chapter we describe Monte Carlo methods to sample an ensemble close in spirit to the common laboratory scenario for constant stress. The underlying transition probability for these methods does not obey detailed balance, and we cannot offer closed forms for their stationary distributions. Thus, the simulations should not be regarded as mathematically well-controlled approximations to real equilibrium states, even for the model system we consider for illustration. However, using the constant-stress framework, we are able to accurately apply large stresses to a nonlinearly elastic system, as evidence by the small difference between the imposed stress and the measured (virial) stress. For the model system, we show that our method can be used to probe very nonlinear stress-strain behavior and elastic phase transitions.

5.2 The reference state of strain

Subtleties associated with sampling an ensemble of elastic deformation arise with the very definition of stress and strain. We therefore begin by discussing these basic quantities, adopting the notation introduced by Wallace [131, 132] in his description of finite-strain elasticity theory.

Strain quantifies the amount and type of deformation of an object. It can be specified through a set of internal coordinates in the undeformed state, X_i, and their transformed counterparts x_i in the deformed state. Limiting our attention to affine deformations, strain can be compactly described through a matrix α_{ij},

$$x_i = \alpha_{ij} X_j = (u_{ij} + \delta_{ij})\, X_j, \tag{5.1}$$

where u_{ij} is the conventional displacement matrix and δ_{ij} is the Kronecker delta. Einstein notation is implied by repeated subscripts, which refer to projections onto Cartesian axes. In principle, the reference state X is artificial, and need not correspond to an undeformed configuration. In practice, many computational methods presume knowledge of such a state, and are most easily described with X chosen accordingly.

Systems of statistical-mechanical interest typically comprise many interacting particles. As a material property, strain should arise only when their coordinates change relative to each other – as a pure rotation, for example, should not register as a strain. The Lagrangian strain η_{ij} provides such a measure of internal deformation [132]:

$$\eta_{ij} = \frac{1}{2}\left(\alpha_{ki}\alpha_{kj} - \delta_{ij}\right) = \frac{1}{2}\left(u_{ij} + u_{ji} + u_{ki}u_{kj}\right). \tag{5.2}$$

Stress is a directional force per unit area, i.e., a tensorial generalization of pressure. In terms of the force f_i acting on an infinitesimal surface element with normal vector $\mathrm{d}s_j$:

$$T_{ij}\mathrm{d}s_j = f_i. \tag{5.3}$$

We can calculate the work required for an infinitesimal deformation,

$$\delta W = \int_S \mathrm{d}s_i T_{ij} \delta x_j, \tag{5.4}$$

For a system that has volume V_0 at zero strain [132],

$$\delta W = T_{ij}\alpha_{ij}^{-1}\delta\eta_{mn}\alpha_{ni}^{-1}\left|\alpha\right| V_0 \tag{5.5}$$

Stress can therefore be obtained from the thermodynamics of small displacements as the derivative of free energy F with respect to the Lagrangian strain

$$T_{ij} = V_0^{-1}\alpha_{ik}\alpha_{jl}\left(\frac{\partial F}{\partial \eta_{kl}}\right)_T. \tag{5.6}$$

Equations 5.5 and 5.6 manifest a close connection between stress and strain, but they also make clear that these quantities are not simply conjugate to one another in the same sens as, e.g., pressure and volume. Their somewhat more complicated relationship in fact precludes a well-defined ensemble of strain fluctuations at constant stress.

Under a set of fixed external forces, a very stiff system executes only very small fluctuations about its equilibrium shape. To a good approximation in this case,

$$\delta W_{\text{stiff}} \approx T_{ij}\delta\eta_{ji}V_0, \tag{5.7}$$

where we have neglected all terms of higher order in η. Because of this simplification, it is straightforward to consider strain variations at fixed stress T as being governed by a simple external potential

$$V_{\text{stiff}}(\eta) = V_0 T_{ij}\eta_{ji}. \tag{5.8}$$

Eq. 5.8 has formed the basis of many simulations of elastic solids [86]. The approximation underlying Eq. 5.8 are well-founded, however, only when (*a*) the reference state X corresponds to the equilibrium shape, and (*b*) spontaneous excursions away from X are severely limited by internal forces. The former condition complicates applications to cases of high stress, even for stiff systems, since the system's shape is generally unknown *a priori* outside the regime of linear response. For soft materials, inevitable violation of condition *b* necessitates a different approach.

Problems arise when strain fluctuations are sufficiently large such that δW_{stiff} is a poor approximation to δW. If the external forces acting on a material are held constant, i.e. fixing T_{ij}, then δW is not an exact differential. There exists in general no external potential $V(\eta_{ij})$ which regulates strain fluctuations in the same way as fixing T_{ij}. Though computationally inconvenient, this fact does not of course negate the possibility of stable equilibrium states at fixed T_{ij}. It instead means that the probability distribution functions governing their microscopic fluctuations cannot be deduced from the standard partitioning of a conserved quantity.

5.3 The work of a finite deformation

In order to formulate an ensemble with constant stress tensor, we will first calculate the work associated with a finite deformation under constant stress. From this work function we can define a pseudo-Hamiltonian: a function that gives correct energy differences for single strain component deformations around the current state, but is not a state function in itself. We will then use this work to define a pseudo-Hamiltonian based on the elastic state, and use that as the basis for the approximate constant stress ensemble.

Starting with the stress as defined through Eq. 5.3 and an infinitesimally small deformation around the arbitrary state $x_i \to x_i'$, we can define a relative deformation $\delta\alpha_{ij}$

$$x_i' - x_i = \delta x_i = \left(\alpha_{ij}' - \alpha_{ij}\right) X_j = \delta\alpha_{ij} X_j, \tag{5.9}$$

Now the work of such a deformation is the force on the boundaries of the system times δx_i

$$\begin{aligned} \delta W &= \int_S \mathrm{d}s_i \; T_{ij}\delta x_j \\ &= \int_S \mathrm{d}s_i \; T_{ij}\delta\alpha_{jk} X_k, \end{aligned} \tag{5.10}$$

which, through the divergence theorem, becomes

$$\begin{aligned} \delta W &= \int_V \mathrm{d}x \; \partial_i \left(T_{ij}\delta\alpha_{jk} X_k\right) \\ &= \int_V \mathrm{d}x \; \partial_i \left(T_{ij}\delta\alpha_{jk}\alpha_{kl}^{-1} x_l\right) \\ &= T_{ij}\delta\alpha_{jk}\alpha_{ki}^{-1} V(x) \\ &= T_{ij}\delta\alpha_{jk}\alpha_{ki}^{-1} \left|\alpha\right| V_0. \end{aligned} \tag{5.11}$$

where V_0 is the volume of the system at $\alpha_{ij} = \delta_{ij}$. We can derive the work associated with a finite deformation of the form

$$\alpha_{ij}(\lambda) = \alpha_{ij}^o + \lambda \; \Delta\alpha_{ij} \tag{5.12}$$

where λ goes from 0 to 1 as the system goes from α^o to α^n, and $\Delta\alpha_{ij} = \alpha_{ij}^n - \alpha_{ij}^o$, the total amount of finite work $\Delta W^{o\to n}$ is

$$\begin{aligned} \Delta W^{o\to n} &= \int_0^1 \mathrm{d}\lambda \; \frac{\partial W(\lambda)}{\partial\lambda} \\ &= \int_0^1 \mathrm{d}\lambda \; \lim_{\epsilon\to 0} \epsilon^{-1} V_0 T_{ij}\alpha_{ki}^{-1}(\lambda) \left|\alpha(\lambda)\right| \\ &\qquad\qquad \times \left[\alpha_{jk}(\lambda+\epsilon) - \alpha_{jk}(\lambda)\right] \\ &= V_0 T_{ij}\Delta\alpha_{jk} \int_0^1 \mathrm{d}\lambda \; \alpha_{ki}^{-1}(\lambda) \left|\alpha(\lambda)\right| \\ &= V_0 T_{ij}\Delta\alpha_{jk} \int_0^1 \mathrm{d}\lambda \; C[\alpha(\lambda)]_{ik} \end{aligned} \tag{5.13}$$

where $C[\alpha(\lambda)]_{ij}$ is the cofactor of $\alpha(\lambda)$. This cofactor is

$$C(\alpha)_{ji} = |\alpha|\,\alpha^{-1}_{ij}. \tag{5.14}$$

Because we're dealing with explicit determinants, we need to tackle the 2D and 3D case separately. In 2D the work becomes

$$\begin{aligned}
\Delta W^{o\to n} &= V_0 T_{ij}\Delta\alpha_{jk}\int_0^1 \mathrm{d}\lambda \\
&\quad \times \begin{pmatrix} \alpha^o_{yy}+\lambda\Delta\alpha_{yy} & -\alpha^o_{xy}-\lambda\Delta\alpha_{xy} \\ -\alpha^o_{yx}-\lambda\Delta\alpha_{yx} & \alpha^o_{xx}+\lambda\Delta\alpha_{xx} \end{pmatrix}_{ki} \\
&= V_0 T_{ij}\Delta\alpha_{jk}\Bigg[\begin{pmatrix} \alpha^o_{yy} & -\alpha^o_{xy} \\ -\alpha^o_{yx} & \alpha^o_{xx} \end{pmatrix}_{ki} \\
&\qquad\qquad + \frac{1}{2}\begin{pmatrix} \Delta\alpha_{yy} & -\Delta\alpha_{xy} \\ -\Delta\alpha_{yx} & \Delta\alpha_{xx} \end{pmatrix}_{ki}\Bigg] \\
&= V_0 T_{ij}\Delta\alpha_{jk}\left(C(\alpha^o)_{ik} + \frac{1}{2}C(\Delta\alpha)_{ik}\right) \\
&= V_0 T_{ij}\Delta\alpha_{jk}\left(|\alpha^o|\,(\alpha^o)^{-1}_{ki} + \frac{1}{2}|\Delta\alpha|\,(\Delta\alpha)^{-1}_{ki}\right) \\
&= V_0\,|\alpha^o|\,T_{ij}\Delta\alpha_{jk}(\alpha^o)^{-1}_{ki} + V_0\frac{1}{2}T_{ii}\,|\Delta\alpha|
\end{aligned} \tag{5.15}$$

and in 3D, it is

$$\begin{aligned}
\Delta W^{o\to n} &= V_0 T_{ij}\Delta\alpha_{jk}\int_0^1 \mathrm{d}\lambda \\
&\quad \times \begin{pmatrix} \left|\begin{matrix} \alpha^o_{yy}+\lambda\Delta\alpha_{yy} & \alpha^o_{zy}+\lambda\Delta\alpha_{zy} \\ \alpha^o_{yz}+\lambda\Delta\alpha_{yz} & \alpha^o_{zz}+\lambda\Delta\alpha_{zz} \end{matrix}\right| & \cdots \\ \vdots & \ddots \end{pmatrix}_{ki} \\
&= V_0 T_{ij}\Delta\alpha_{jk}\int_0^1 \mathrm{d}\lambda\; C(\alpha^o)_{ik} + \lambda^2 C(\Delta\alpha)_{ik} + \lambda\Gamma_{ki} \\
&= V_0 T_{ij}\Delta\alpha_{jk}\left[C(\alpha^o)_{ik} + \frac{1}{3}C(\Delta\alpha)_{ik} + \frac{1}{2}\Gamma_{ki}\right] \\
&= V_0\Bigg(|\alpha^o|\,T_{ij}\Delta\alpha_{jk}(\alpha^o)^{-1}_{ki} + \frac{1}{2}T_{ij}\Delta\alpha_{jk}\Gamma_{ki} \\
&\qquad + \frac{1}{3}|\Delta\alpha|\,T_{ii}\Bigg)
\end{aligned} \tag{5.16}$$

Here Γ_{ij} is a cofactor-like matrix that holds cross terms from α^o and $\Delta\alpha$. Its full form is

$$\Gamma_{ij} = \left(\begin{array}{ccc} \alpha^o_{yy}\Delta\alpha_{zz} & -\alpha^o_{xy}\Delta\alpha_{zz} & \alpha^o_{xy}\Delta\alpha_{yz} \\ +\alpha^o_{zz}\Delta\alpha_{yy} & -\alpha^o_{zz}\Delta\alpha_{xy} & +\alpha^o_{yz}\Delta\alpha_{xy} \\ -\alpha^o_{yz}\Delta\alpha_{zy} & +\alpha^o_{xz}\Delta\alpha_{zy} & -\alpha^o_{xz}\Delta\alpha_{yy} \\ -\alpha^o_{zy}\Delta\alpha_{yz} & +\alpha^o_{zy}\Delta\alpha_{xz} & -\alpha^o_{yy}\Delta\alpha_{xz} \\ \\ -\alpha^o_{yx}\Delta\alpha_{zz} & \alpha^o_{xx}\Delta\alpha_{zz} & -\alpha^o_{xx}\Delta\alpha_{yz} \\ -\alpha^o_{zz}\Delta\alpha_{yx} & +\alpha^o_{zz}\Delta\alpha_{xx} & -\alpha^o_{yz}\Delta\alpha_{xx} \\ +\alpha^o_{yz}\Delta\alpha_{zx} & -\alpha^o_{xz}\Delta\alpha_{zx} & +\alpha^o_{xz}\Delta\alpha_{yx} \\ +\alpha^o_{zx}\Delta\alpha_{yz} & -\alpha^o_{zx}\Delta\alpha_{xz} & +\alpha^o_{yx}\Delta\alpha_{xz} \\ \\ \alpha^o_{yx}\Delta\alpha_{zy} & -\alpha^o_{xx}\Delta\alpha_{zy} & \alpha^o_{xx}\Delta\alpha_{yy} \\ +\alpha^o_{zy}\Delta\alpha_{yx} & -\alpha^o_{zy}\Delta\alpha_{xx} & +\alpha^o_{yy}\Delta\alpha_{xx} \\ -\alpha^o_{yy}\Delta\alpha_{zx} & +\alpha^o_{xy}\Delta\alpha_{zx} & -\alpha^o_{xy}\Delta\alpha_{yx} \\ -\alpha^o_{zx}\Delta\alpha_{yy} & +\alpha^o_{zx}\Delta\alpha_{xy} & -\alpha^o_{yx}\Delta\alpha_{xy} \end{array} \right) \tag{5.17}$$

Note that both in 2D and 3D, for an isotropic expansion under isotropic pressure $T_{ij} = \delta_{ij}P$, the following relation holds:

$$\Delta W^{o\to n} = PV_0\left(|\alpha^n| - |\alpha^o|\right) = P\Delta V \tag{5.18}$$

5.4 The constant-stress pseudo-ensemble

It is important to note that Eqs. 5.15 and 5.16 are not state functions: the work is path-dependent. This can easily be shown by example: consider the case where the pressure tensor is

$$T_{ij} = \left(\begin{array}{cc} P_x & 0 \\ 0 & P_y \end{array} \right). \tag{5.19}$$

Comparing the energies associated with deformations between strain states

$$\alpha^o = \left(\begin{array}{cc} 1 & 0 \\ 0 & 1 \end{array} \right), \quad \alpha^{n'} = \left(\begin{array}{cc} c & 0 \\ 0 & 1 \end{array} \right), \quad \alpha^n = \left(\begin{array}{cc} c & 0 \\ 0 & c \end{array} \right) \tag{5.20}$$

we arrive at energy differences

$$\begin{aligned} \Delta W^{o\to n'} &= V_0(c-1)P_x \\ \Delta W^{n'\to n} &= V_0(c-1)P_y \end{aligned} \tag{5.21}$$

while a direct transformation between $o \to n$ leads to

$$\Delta W^{o\to n} = V_0(P_x + P_y)\left[(c-1) + \frac{1}{2}(c-1)^2\right]. \tag{5.22}$$

This discrepancy is unsurprising: it is a result of the thermodynamic tension being the conjugate to the stress tensor. The work functions of Eqs. 5.15 and 5.16 do allow us to construct a pseudo-Hamiltonian that is *locally* valid for changes in individual strain (α) matrix components.

This means that we can construct a pseudo-ensemble that is locally valid around any average; giving us the correct thermodynamic ground state for any pressure tensor. Because the pressure tensor is the experimentally most readily available form of stress, and we do not rely on the starting state as a reference state, this ensemble can be used to quickly explore elastic behavior.

In order to arrive at the pseudo-ensemble, we start with Eqs. 5.15 and 5.16, giving us an energy difference between two different strain states given a constant stress. To formulate the ensemble, we need a Hamiltonian-like function: we start with a state with zero 'energy', and an associated (but otherwise completely arbitrary) reference state. We can take

$$\alpha_{ij}^{o} = \delta_{ij}, \tag{5.23}$$

so the deformation change becomes

$$\Delta\alpha_{ij} = \alpha_{ij} - \delta_{ij} = u_{ij}. \tag{5.24}$$

where u_{ij} is the displacement matrix of the state for which the energy is calculated. Given this 'zero state', the 2D case of Eq. 5.15 reduces to

$$E_2(\alpha) = V_0 \left(T_{ij} u_{ji} + \frac{1}{2} T_{ii} \left| u \right| \right). \tag{5.25}$$

With this, we can formulate a constant tension ensemble with a partition sum

$$\begin{aligned} \Xi_2(N, T_{ij}, T) &= \int \mathrm{d}\alpha \mathrm{d}\nu \ \exp\left[-\beta E_2(\alpha) - \beta \mathcal{H}(\nu) \right] \\ &= \int \mathrm{d}\alpha \mathrm{d}\nu \ \exp\Bigg[-\beta V_0 \left(T_{kl} u_{lk} + \frac{1}{2} \left| u \right| T_{ll} \right) \\ &\qquad\qquad -\beta \mathcal{H}(\nu) \Bigg] \end{aligned} \tag{5.26}$$

where ν is the collection of microstates within the space spanned by α. In 3D, we use the same procedure and take the same zero state for the energy as for 2D. The energy with respect to $\alpha_{ij}^{o} = \delta_{ij}$ is, according to Eq. 5.16,

$$E_3(\alpha) = V_0 \left[T_{ij} \Delta\alpha_{jk} \delta_{ki} + \frac{1}{2} T_{ij} \Delta\alpha_{jk} \Gamma_{ki} + \frac{1}{3} \left| \Delta\alpha \right| T_{ii} \right] \tag{5.27}$$

where Γ_{ij} simplifies to

$$\Gamma_{ij} = \delta_{ij} u_{kk} - u_{ij} \tag{5.28}$$

which makes

$$\begin{aligned} E_3(\alpha) &= V_0 \left(T_{ij} u_{ji} + \frac{1}{2} T_{ij} u_{ji} u_{mm} - \frac{1}{2} T_{ij} u_{jk} u_{ki} + \frac{1}{3} T_{ii} |u| \right) \\ &\equiv V_0 \left[T_{ij} \omega_{ji} + \frac{1}{3} T_{ii} |u| \right], \end{aligned} \tag{5.29}$$

where, for notational convenience, we introduce the matrix

$$\omega_{ji} \equiv u_{ji} + \frac{1}{2} u_{ji} u_{kk} - \frac{1}{2} u_{jk} u_{ki}. \tag{5.30}$$

With this, we can write a constant stress partition function as

$$\Xi_3(N, T_{ij}, T) = \int \mathrm{d}\alpha \mathrm{d}\nu \ \exp\left(-\beta \left[E_3(\alpha) + \mathcal{H}(\nu)\right]\right) \tag{5.31}$$

5.5 A test system

As an example application of the constant stress ensemble, we have performed simulations of a two-dimensional system of point particles interacting in a pairwise fashion through a purely repulsive Gaussian shaped potential, known as the Gaussian core model:

$$U_{\mathrm{GC}}(r) = \epsilon \exp\left(-\frac{r^2}{\sigma^2}\right) \tag{5.32}$$

where r is the interparticle distance, and ϵ and σ are tunable parameters, modulating the interaction strength and the range, respectively.

The soft interactions of the model result in significant nonlinear elastic response, while its simplicity allows for direct comparison between constant-stress and constant strain methods. At a temperature of $T = 0.0005\ \epsilon/k_B$ and a number density of $\rho = 0.4/\sigma^2$ (corresponding to imposed stress of $T_{xx} = 0.195105\ \epsilon/\sigma^2$, $T_{yy} = 0.195114\ \epsilon/\sigma^2$, and T_{xy}, $T_{yx} = 0$), the system is stable as a hexagonal crystal.

With only the pairwise Gaussian core potential, plastic flow was observed under high strain. Since there is no potential enforcing a certain coordination between particles, slippage occurs and the system is able to access a lower stress state (Fig. 5.1). To prevent plastic flow, we added an additional neighboring potential between each particle and its six nearest neighbors:

$$U_{\mathrm{nb}}(r) = \begin{cases} 0 & \text{if } r < r_c, \\ \epsilon \left(\dfrac{r - r_c}{\sigma} \right)^6 & \text{otherwise,} \end{cases} \tag{5.33}$$

where we set the cut-off distance $r_c = 1.03\langle \Delta r \rangle \approx 1.80\ \sigma$, and $\langle \Delta r \rangle$ is the average distance between neighboring particles in the undeformed crystal at $\rho = 0.4/\sigma^2$. At small strain

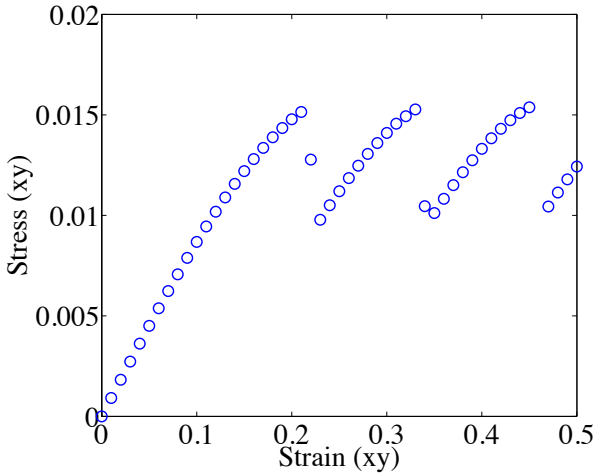

Figure 5.1: **Plastic flow stress-strain curve.** Plastic flow was observed under high strain. Since there is no potential enforcing a certain coordination between particles, slippage occurs and the system is able to access a lower stress state. This occurs several times as the simple shear is applied to the system.

values, when no plastic behavior is observed, the typical distance between an atom and its six nearest neighbors is less than r_c. Therefore, the neighboring potential contributes negligibly to the internal energy of the undeformed (or weakly deformed) system and linear elastic response is dictated by the Gaussian core potential. However, at larger strain values when slippage would be favored by the Gaussian core potential, typical neighbor distances will tend to exceed r_c, activating the neighboring potential. The rapid increase of $U_{\mathrm{nb}}(r)$ once $r > r_c$ effectively enforces a topological constraint that prohibits changes in particle coordination that would accompany plastic flow. Thus, introducing $U_{\mathrm{nb}}(r)$ allows us to assess highly nonlinear yet elastic stress-strain behavior. It is important to note that this behavior is reversible; the same curve is produced by gradually increasing strain from 0 to 0.5 and by subsequently decreasing the strain back to 0.

Fig. 5.2 shows the nonlinear stress-strain response of this system. Simple shear strain deformation (volume-conserving, 0% to 50% strain) was imposed on the rectangular solid, and the corresponding stress was measured using the virial stress equation,

$$T_{\alpha,\beta} = \langle \sum_{ij} F_{ij,\alpha} \cdot r_{ij,\beta} \rangle / V, \tag{5.34}$$

where T is the stress tensor, i, j are interacting particles, and α, β are Cartesian indices.

As an illustration of the nonlinear stress-strain response of this system, Fig. 5.3a shows shear (xy) stress as a response to imposed shear strain for this system, where two strain components are free to fluctuate (xx and xy): the strain response is single-valued and clearly nonlinear: it shows a softening (large strain response to small stress change) around $T_{xy} \approx$

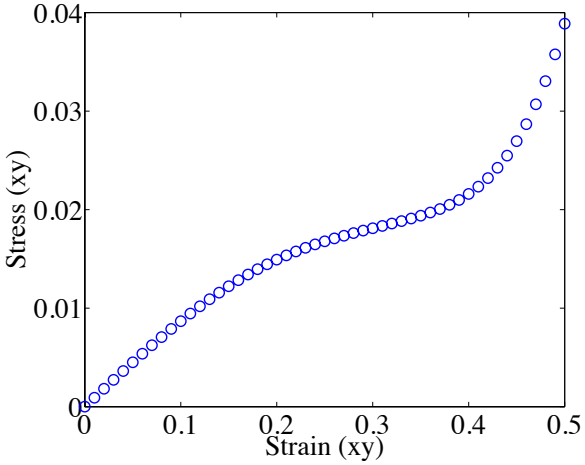

Figure 5.2: **Constant strain (benchmark) simulation.** Nonlinear response of shear (xy) stress to imposed shear strain of the Gaussian core model. Simple shear strain deformation (volume-conserving, 0% to 50% strain) was imposed on the rectangular solid, and the corresponding stress was measured using the virial stress equation (Eq. 5.34).

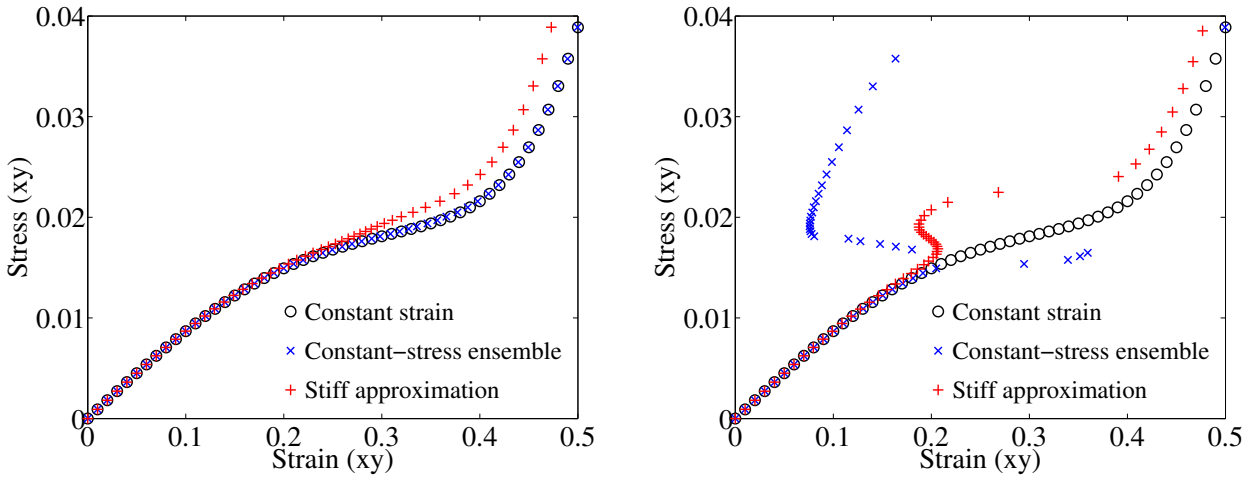

Figure 5.3: **Stress-strain response under shear.** Nonlinear response of shear (xy) stress to imposed shear strain of the Gaussian core model. (a) For the strain fluctuation methods, only the xx and xy components of the deformation matrix are free to fluctuate. (b) All independent strain components (xx, xy, yy) are free to fluctuate.

0.015 ϵ/σ^2, and stiffening at $T_{xy} \approx 0.020\epsilon/\sigma^2$. Note that here, while the the constant-stress method of Section 5.4 reproduces the strains (and stresses) of the constant strain method, the stiff approximation deviates from the two other methods at high stress, where the difference between the stress and thermodynamic tension is large.

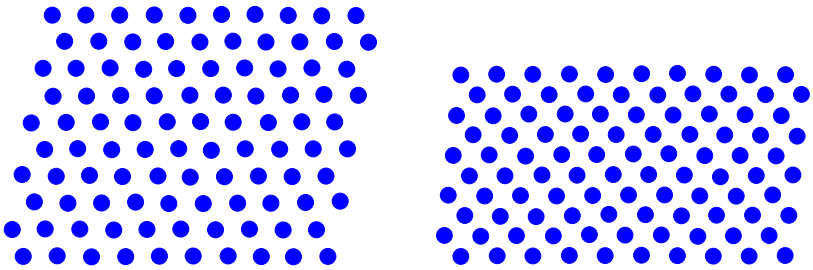

(a) (b)

Figure 5.4: **Sheared configurations.** Configurations near the elastic phase transition, at $T_{xy} = 0.02006\ \epsilon/\sigma^2$ (and diagonal components as in Fig. 5.3b). Configuration (a) shows a the strain state adopted by the stiff approximation, and (b) shows the compressed state adopted by the constant-stress method of Section 5.4

When all three independent elements of the strain matrix are allowed to fluctuate, the picture becomes more complex: Fig. 5.3b shows that while the constant strain measurements show, by definition, no change in behavior, the strain fluctuation methods now show markedly different behavior.

This divergence is caused by an elastic transition around $T_{xy} \approx 0.015\ \epsilon/\sigma^2$: the constant-stress method of Section 5.4 converges towards a new crystalline state with compressed yy strain. Fig. 5.4 shows crystalline configurations from both the stiff approximation and the constant-stress method. The situation is more clearly illustrated by the strain distributions close to the phase transition, as shown in Fig. 5.5. Here, the constant-stress method shows a bimodal distribution while the stiff approximation only identifies a single peak.

In fact, the difference between imposed stress and resulting virial stress, as shown in Fig. 5.7, highlights the difference between the two methods: while the constant-stress method maintains the imposed stress, the stiff approximation shows large deviations from the imposed stress at the phase transition. While this strictly speaking is not erroneous – the difference between stress and thermodynamic tension is large when strains are far away from the zero strain state – it is clearly not a desirable feature for a strain fluctuation method.

More fundamental, however, is the failure of the stiff approximation to identify multiple coexisting states at the same stress: no amount of zero-strain-state correction could improve that, because multiple states with the same stress each have their own, not *a priori* identifiable, zero strain state.

It should to noted that the strain distributions of Fig. 5.5 are not necessarily the probability distributions of the underlying system, because the method of Section 5.4 does not rely

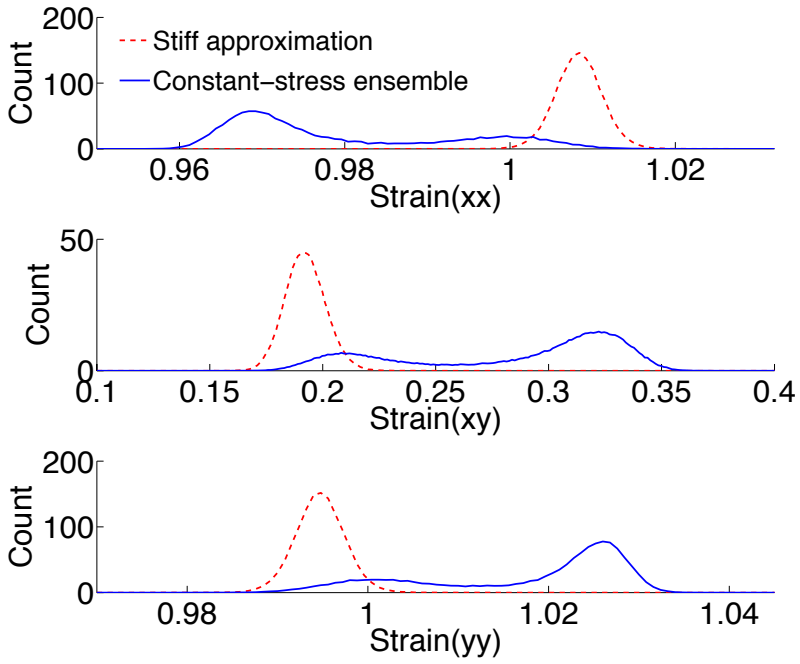

Figure 5.5: **Strain distributions.** Strain distributions around $T_{xy} = 0.01536\ \epsilon/\sigma^2$, for the two strain fluctuation methods.

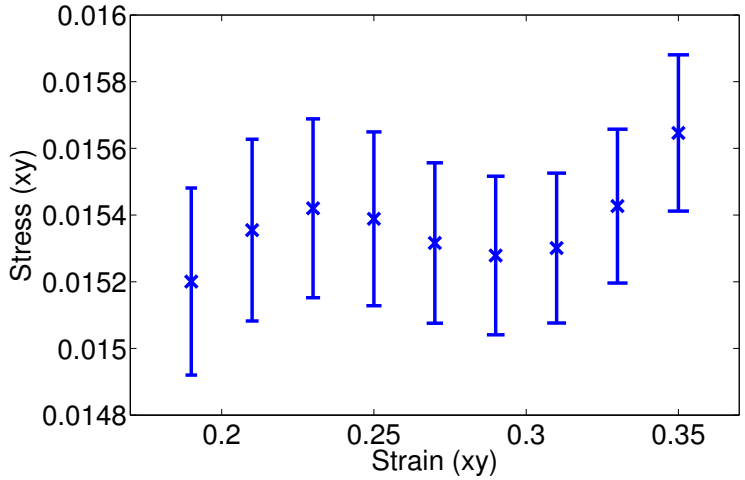

Figure 5.6: **Stress distributions.** Stress distribution around $T_{xy} = 0.01536\ \epsilon/\sigma^2$: measured shear virial stresses over the full range of shear strains for the constant-stress method of Section 5.4.

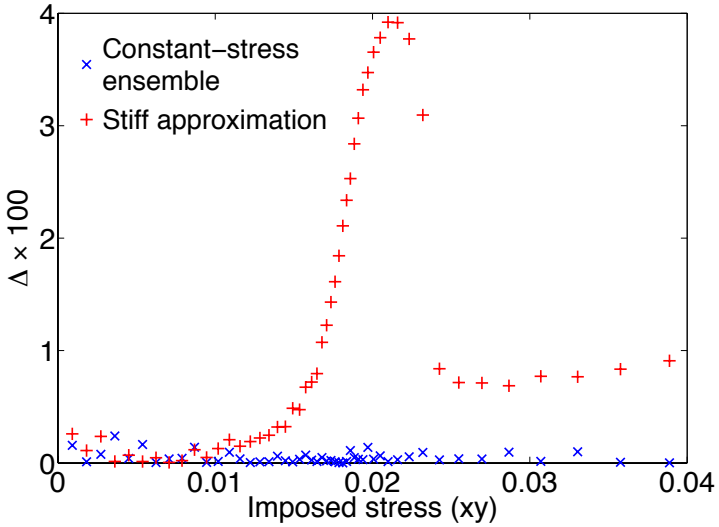

Figure 5.7: **Comparison of errors.** Relative difference between the imposed and the measured (virial) stress for T_{xy}: $\Delta = (T_{xy}^{\text{virial}} - T_{xy})/T_{xy}$, for varying imposed stress.

on a valid statistical mechanical ensemble. The fact that all strains generated by this method have the same average stress does mean that the strain states in both peaks of Fig. 5.5 are compatible with this stress and are therefore likely to be present in any experiment with similar conditions.

5.6 Conclusions

We have introduced a pseudo-ensemble, based on an imposed stress tensor. By using a stress tensor instead of a thermodynamic tension, application of this ensemble in simulations allows the exploration of large excursions in strain and the sampling of elastic phase transitions where multiple values of strain may be stable at once.

As a test for this ensemble, we have explored the elastic behavior of a simple model system that shows nonlinear elasticity and an elastic phase transition at moderate shear stresses. This phase transition clearly shows the limitations of classical constant strain methods and the stiff approximation: neither shows the presence of two stable elastic states.

While the amplitudes of the strain distributions using the constant-stress method may not be representative of the true underlying probability distribution of strain given an imposed stress, the method does sample states that share the same stress tensor. Thus, we have shown that the constant-stress method is an effective method to quickly explore the full range of nonlinear elastic (phase) behavior, which can then be used as an input for more quantitative methods.

Chapter 6

Toward an understanding of actin network elasticity

Biopolymer networks which make up the cytoskeleton tend to exhibit stiffening at low to intermediate strains, a property that is essential in maintaining the structural integrity of cells under external force. While there are many experimental and theoretical studies probing the elasticity of actin networks under shear, there are far fewer studies on the behavior of such networks under compression, a biologically significant case. In this work, we explore actin network elasticity under compression. Using our previously developed constant-stress method and a coarse-grained model for short, semiflexible chains, we investigate the elastic response of actin networks as a function of the network architecture as well as single filament configurations that give rise to the bulk mechanical properties. We observed that under compression, networks consistently exhibited a linearly elastic response followed by stress softening. Additionally, at the single filament length scale, increasing compression resulted in a bimodal distribution of segment lengths composed of bent and unbent filaments, with no evidence for filament stretching. Using a normal mode analysis, we are further able to identify soft regions in the networks and obtain a rough estimate of the relative linear elastic modulus among various networks. Our findings shed light on the elastic behavior of actin networks under compression and can be used to motivate new experiments in this area.

6.1 Introduction

A material's elasticity refers to its tendency to resist deformation under external force. More quantitatively, this tendency is measured by the relationship between stress (average force per unit area) and strain (deformation). Linearly elastic materials will deform twice as much when the external force is doubled (Fig. 6.1a). The corresponding elastic modulus, which is the slope of the stress–strain curve, will be constant, independent of the strain or stress state of the material. For a nonlinearly elastic material, how much the material deforms per unit stress depends on the stress state of the material (Fig. 6.1 b and c). The corresponding

elastic modulus will not be constant, but rather a function of the stress or strain.

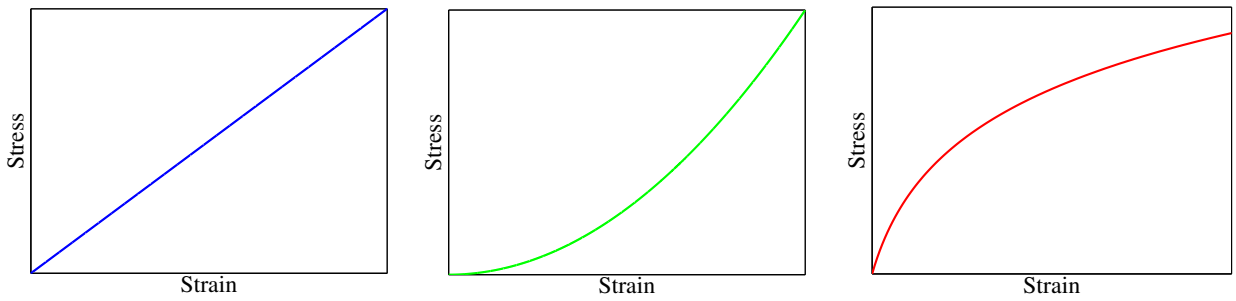

Figure 6.1: **Linear and nonlinear elasticity.** An elastic material can exhibit (a) linear elasticity or nonlinear elasticity in the form of (b) stiffening or (c) softening. For linearly elastic materials, the elastic modulus, which is the slope of the stress-strain curve, is constant. For nonlinearly elastic materials, the elastic modulus changes as a function of stress or strain.

Many biological gels such as actin gels display very nonlinear elastic properties, which is intimately related to their functions in the cell [116]. Both experimental and theoretical studies have found that these biological gels tend to stiffen under applied stress or strain [41, 59, 12, 61, 54]. This behavior is functionally very useful because by stiffening, actin and other filament networks that make up the cellular cytoskeleton help to preserve the structural integrity of the cell, allowing the cell to properly do its job.

There have been many studies probing the elastic properties of actin networks, many of which involve applying simple shear to the networks and measuring the corresponding stress or strain in the system. Nonlinear stress or strain stiffening has been observed at low to moderate strains in several experiments involving crosslinked actin networks formed *in vitro* [41, 116]. Although this general behavior has been observed across a variety of experiments, the magnitude of the elastic modulus can be tuned by the crosslink density, actin concentration [41], and the type of crosslinking protein [40]. A common feature of these experiments is that the filaments in these networks are isotropically (randomly) oriented. One model that has been proposed to explain the stiffening behavior is based on the interplay between bending and stretching forces at the single filament level. Filament bending is much less costly than filament stretching. Therefore initially, the constituent filaments remain oriented in their reference configuration and are able to accommodate the network deformation through bending. However, as the network becomes more deformed, the filaments reorient themselves in the direction of the shear. At this point, they are forced to stretch. Since filament stretching is much more costly than bending, strain or stress stiffening is observed [59].

Compared to experiments involving shear, experiments in which actin networks are subjected to uniaxial compression are far less common. However, the biological relevance and significance of such forces cannot be understated. The growing dentritic actin network near the cell membrane, responsible for cell movement, is subjected to the compressive forces of

the membrane and extracellular environment. This complex mix of actin growth and compression ultimately results in cell motility. In a seminal experiment performed by Chaudhuri and coworkers [16], compressional force (using a AFM cantilever) was applied to a dendritic actin network reconstituted *in vitro* (Fig. 6.2a). A linearly elastic regime was initially observed at low stress, followed by stress stiffening, and finally stress softening at high stress (Fig. 6.2b). This behavior was shown to be reversible, demonstrating that the softening was not caused by network fracture or unbinding of the crosslinkers. Although stiffening behavior has been previously measured in other experiments, reversible softening was a novel observation. To explain this behavior, they proposed a model in which the initial stress stiffening arises from filaments resisting compression and extension. But at some point, the applied force is so large that filaments begin to buckle reversibly, resulting in a softening regime.

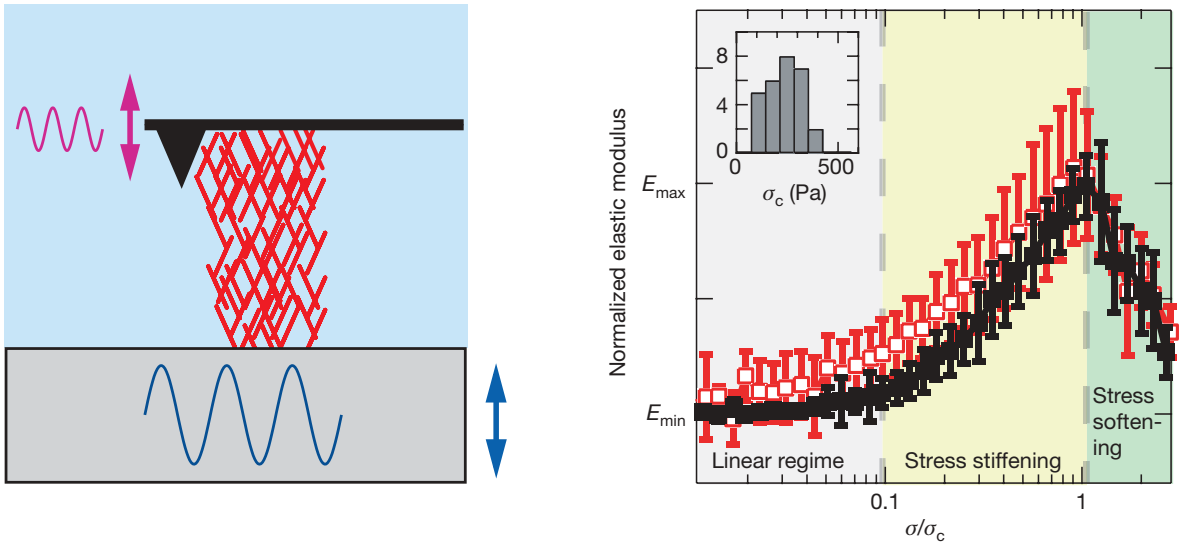

Figure 6.2: **Reversible stress stiffening and softening.** (a) An AFM cantilever was used to apply compressional force to actin networks reconstituted *in vitro*. (b) Reversible stress stiffening and softening of actin networks under compression. Figure adapted from [16].

The aim of this work is to understand what underlies these elastic properties. The bulk elastic properties can be ultimately attributed to the configurations of single filaments and whether they are predominantly bent or stretched. The transition from bending to stretching modes often leads to drastic changes in the material properties. However, it is unclear what parameter or property of the network connects the behavior at the single filament level to the elastic quantities we measure at the network level. Experimental evidence points to the hypothesis that the architecture of the gel might serve as a bridge connecting the two length scales. We aim to better understand whether the network architecture or other parameters

are the fundamental link between bulk elastic properties and behavior at the single filament level.

6.2 Simulation model, methods, and parameters

6.2.1 Model for single segments

Using the discretized worm-like chain model (Ch. 2), we specify a single configuration of a chain with contour length L and a discretization length Δs by enumerating the positions of all $L/\Delta s + 1$ points along the chain,

$$\{\mathbf{r}_1, \mathbf{r}_2, ..., \mathbf{r}_{L/\Delta s+1}\}. \tag{6.1}$$

Despite the relative simplicity of the WLC model, it is still too computationally costly to use for modeling sizable actin networks.

To approximate short, semiflexible segments within a filament network, we build upon the work of Pronk and Geissler and utilize their coarse-grained model for single chains and segments [97, 136]. Instead of keeping track of all the monomers in a filament, the model integrates out the positions and orientations of all intermediate monomers, which is possible by making a small curvature approximation (Eq. 4.8). Thus, we only keep track of the positions and orientations of the endpoints, or where the filaments are crosslinked (Fig. 6.3). The reduction in the degrees of freedoms allows us to model much bigger systems than previously.

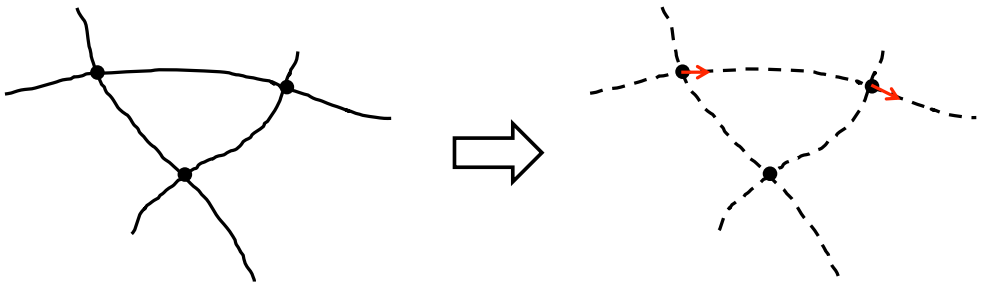

Figure 6.3: **Coarse-grained representation of crosslinked filaments.** Instead of having to represent all the monomer positions between crosslinks, we only keep track of the positions of the crosslinks and the orientations of the filaments at the crosslinks. Figure adapted from [136].

Using the model, a single segment within a filament network is described by its contour length L, positions at its endpoints $\{\mathbf{r}(0), \mathbf{r}(L)\}$, and orientations at its endpoints $\{\hat{\mathbf{t}}(0), \hat{\mathbf{t}}(L)\}$. It is important to note that each microstate in the model represents not a

single chain configuration but rather an ensemble of configurations satisfying the constraints

$$\{\mathbf{r}(0), \mathbf{r}(L), \hat{\mathbf{t}}(0), \hat{\mathbf{t}}(L), L\}. \tag{6.2}$$

If we translate and rotate the chain in a way such that one of the endpoints $\mathbf{r}(0)$ is at the origin and its orientation vector $\hat{\mathbf{t}}(0)$ points in the z direction, we can eliminate the degrees of freedoms corresponding to the chain position and orientation at one end and represent a microstate as

$$\{\mathbf{r}(L), \hat{\mathbf{t}}(L), L\}. \tag{6.3}$$

A representation of a microstate of the coarse-grained model is shown in Fig. 6.4.

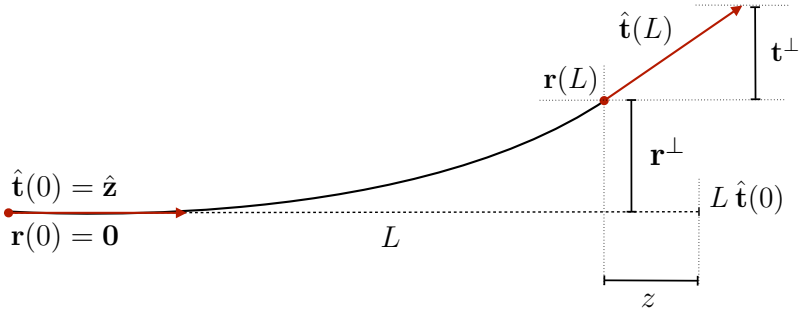

Figure 6.4: **Variables denoting a microstate in the coarse-grained model.** Given that $\mathbf{r}(0)$ is at the origin and $\hat{\mathbf{t}}(0)$ is a unit vector point in the $\hat{\mathbf{z}}$ direction, the pertinent degrees of freedom are $\mathbf{r}(L)$, $\hat{\mathbf{t}}(L)$, and L. Each microstate in the model represents not a single chain configuration but rather an ensemble of configurations satisfying the constraints listed above. Figure adapted from [97].

Using a combination of analytical results and fits based on simulation data, the full free energy was calculated to be

$$F(\mathbf{R}, \mathbf{T}, z) = 2\mathbf{T}^2 + 6\mathbf{R}^2 - 6\mathbf{R}\cdot\mathbf{T} - a + b^2\left((z-c) + \frac{d}{z-c}\right), \tag{6.4}$$

where $\mathbf{R} = \mathbf{r}^{\perp}/L^{3/2}$, $\mathbf{T} = \mathbf{t}^{\perp}/L^{1/2}$, $z = L - \mathbf{r}(L)\cdot\hat{\mathbf{t}}(0)$, and a, b, c, d (detailed in Appendix, Sec. A.1) are functions of $\mathbf{R}$ and $\mathbf{T}$.

We tested our approximate coarse-grained model against the more detailed WLC model by comparing the free energy as a function of the end-to-end distance/contour length ratio. As seen in Fig. 6.5, the two models agree very well.

6.2.2 Construction of network

In order for our results to be biologically relevant, it is important to create realistic actin network architectures using experimental measurements. One such parameter is the mesh

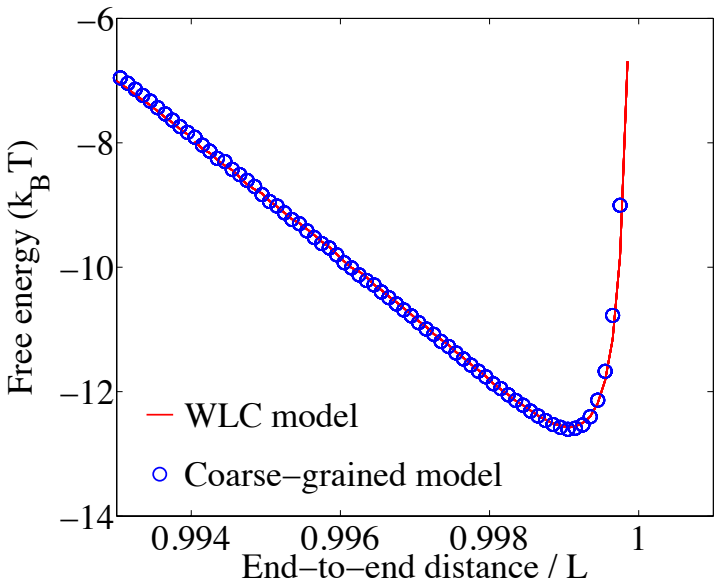

Figure 6.5: **Comparison with the WLC model.** Comparison of the free energy as a function of the end-to-end distance/contour length ratio using the WLC and coarse-grained models. The contour length of the simulated filaments is 1% of its persistence length.

size, or the average distance between adjacent crosslinks. The mesh size for cortical actin has been measured to be approximately 100–200 nm [81, 15]. An additional measure is the minimum length between two adjacent crosslinkers. One of the essential crosslinking proteins in the cell cortex is Filamin A, made up of two 280 kDa subunits [82]. When Filamin A crosslinks actin filaments, each of the two subunits (hinges) extends out approximately 60 nm into the filaments [49], shown in Fig. 6.6. We reason that these measurements effectively impose a minimum segment length constraint on our network geometry.

With the constraints and parameters defined, we use the following procedure to generate two-dimensional networks. We model actin networks in two dimensions as a good approximation for the sheet-like structures of actin networks within the lamellipodia [2]. We iteratively place linear line segments of length L representing filaments into a square, periodically replicated simulation box. Wherever the filaments cross is designated a crosslink. The center of mass for each filament is chosen at random from a uniform distribution inside the box. The orientation of each individual filament, however, is a tunable parameter which we vary. More specifically, the orientation can be drawn from one of two distributions, a uniform or Gaussian distribution from 0° to 180°. The choice of using two distributions is an approximation for the structural differences of actin networks in different parts of the cell, from the orientationally biased branched network to the isotropically oriented random networks (Ch. 1, Sec. 1.3). The percentage of filament orientations drawn from each distribution is the architectural parameter we tune (Fig. 6.7). The filaments whose orientations are drawn from a Gaussian distribution are more likely to be aligned in a similar direction

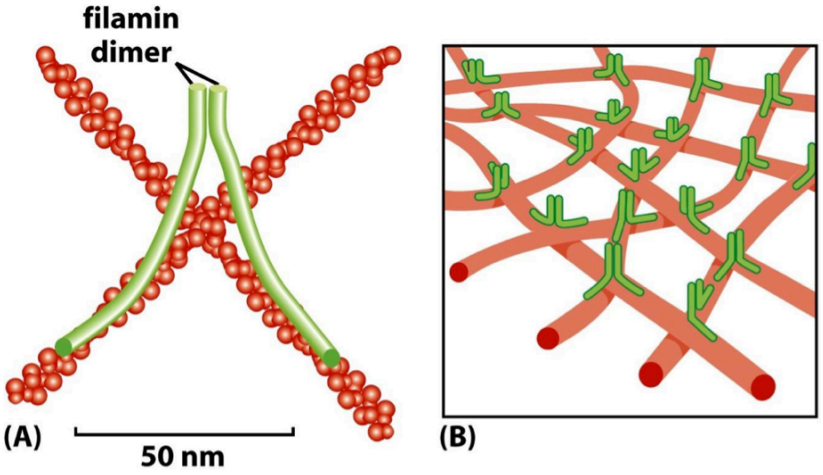

Figure 6.6: **Structure and function of filamin.** (a) Each filamin is made up of two subunits, or hinges, that extends out on each actin filament approximately 60 nm. (b) Filamin proteins crosslink adjacent actin filaments into a network. Figure adapted from [2].

as the direction of the applied stress.

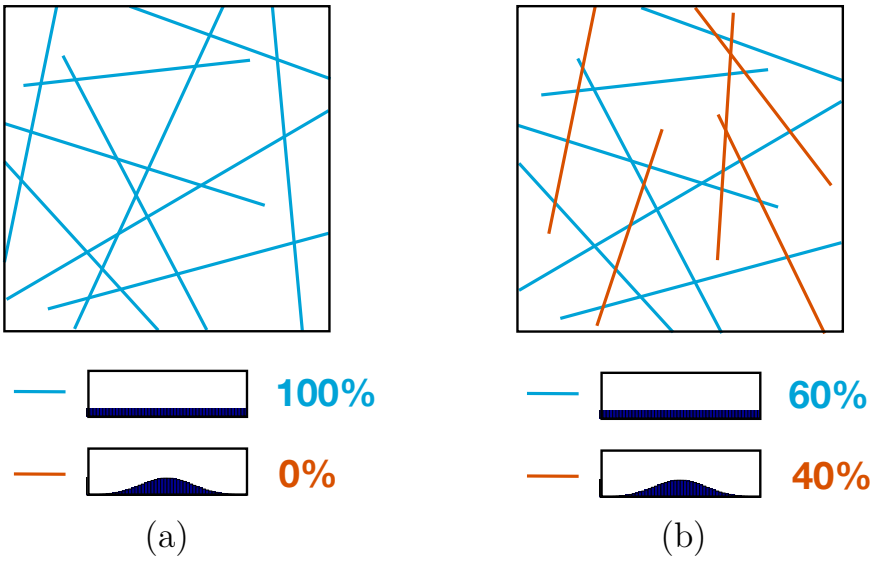

Figure 6.7: **Orientation bias.** Implementation of an orientation bias in the networks. (a) All the filament orientations are drawn from a uniform distribution from 0° to 180°. (b) 60% of the filament orientations are drawn from a uniform distribution while 40% of the orientations are drawn from a Gaussian distribution.

After each filament placement, we calculate the minimum segment length of the network.

If a placement results in a new segment shorter than the minimum segment length, we take out that filament and try again. We stop adding more filaments when the mesh size (average segment length) falls within the accepted range. The segment lengths are the end-to-end distances between adjacent crosslinks. The actual contour length of a segment is slightly greater than its end-to-end length, set such that the end-to-end length correspond to a free energy minimum. Typical geometries generated from this protocol are shown in Fig. 6.8. The lines are only meant to convey the positions of crosslinks and network connectivity. Given the positions of the crosslinks (shown) and the filament orientations at those crosslinks (not shown), each microstate in the model represents an ensemble of configurations satisfying the positional and orientational constraints.

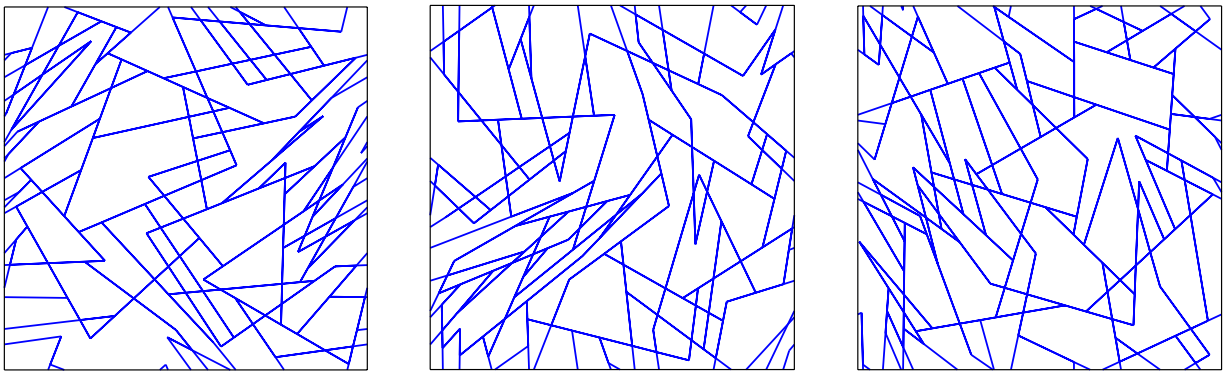

(a) (b) (c)

Figure 6.8: **Typical network structures.** Percentage of filament orientations drawn from a Gaussian distribution: (a) 0% (b) 40% (c) 80%. The size of the system is $0.15\,l_p \times 0.15\,l_p \approx 0.15 \times 0.15\ \mu m^2$. The lines shown are only mean to convey crosslink positions and network connectivity. Each microstate in the model represents an ensemble of configurations satisfying the positional and orientational constraints.

For an efficient and ergodic sampling, we use a combination of crosslink translation, orientation vector rotation, and strain deformation trial moves (Fig. 6.9).

6.2.3 Slice moves

Biological materials such as actin gels are often very inhomogeneous in their spatial organization. For example, one part of an actin network might be dense with filaments and crosslinks while another part might be much more sparse. Naturally, the dense parts of the network are much more stiff than the sparse parts. While this feature poses no problems for nature, it does pose a special problem for simulating such materials. Specifically, dense and stiff parts of a network resist changes in strain very strongly. Therefore, to achieve reasonable

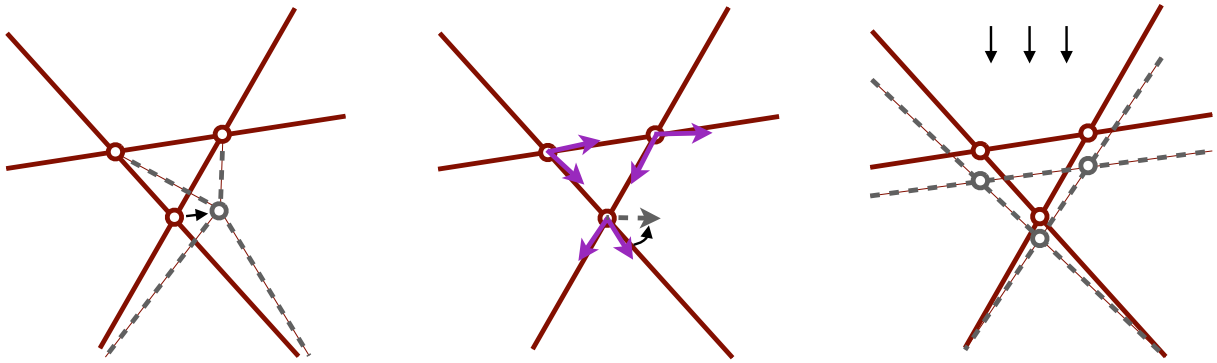

(a) (b) (c)

Figure 6.9: **Monte Carlo moves.** We use a combination of (a) crosslink translation, (b) orientation vector rotation, and (c) strain deformation Monte Carlo trial moves.

acceptance rates for global deformations, the magnitude for strain deformation trial moves must be very small, resulting in very long simulation times.

To circumvent this problem, we make use of partial volume updates (also known as slice) moves (Fig. 6.10) developed by Pronk and Geissler [98]. Instead of rescaling the entire system, we make deformations in randomly selected slices of the system. Since the networks themselves are inhomogeneous, we likewise make box shape changes that are also inhomogeneous. Changes in strain that have a very small probability of being accepted when applied globally now have a greater acceptance probability when applied to a smaller subvolume, greatly speeding up network relaxation and equilibration.

Ultimately, we make use of the slice moves in order to speed up network relaxation and equilibration. To quantify the magnitude of the speed-up, we constructed a simple periodically replicated random network (Fig. 6.11a) and ran constant stress simulations in which we applied stress in the vertical direction and monitored the height fluctuations of the system. The results (Fig. 6.11b) show an approximate 4 fold decrease in equilibration time using slice moves.

6.3 Results

6.3.1 Elastic response of networks under tension

We first evaluate the network elastic response under tension. We hypothesize that these networks will exhibit stress stiffening. As previously mentioned, stretching a filament beyond its equilibrium length distribution is very costly [59]. This observation is illustrated in Fig. 6.5b, where the free energy curve rises rapidly to the right of the free energy minimum. When we put a network under tension, the filaments that are closer in alignment to the direction

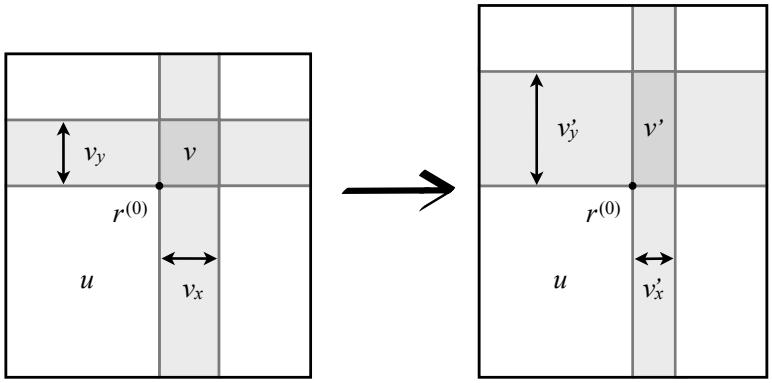

Figure 6.10: **Speeding up simulation using slice moves.** In performing a slice move, we do not rescale the entire system. Rather, we deform a randomly selected vertical or horizontal slice of the network, greatly speeding up the relaxation and equilibration of a system with dense or stiff parts. Figure adapted from [98].

of the applied stress will likely be stretched beyond their equilibrium length, resulting in stiffening behavior.

Indeed, in the simulations, networks stiffened under tension. Since the elasticity of the crosslinkers (tested in Sec. 6.3.3) or entanglement effects are not included in the model, the stiffening behavior is solely attributed to the elasticity of single filaments.

6.3.2 Elastic response of the network under compression

Next, we characterized the mechanical behavior of networks under compression. In the introduction of this chapter, we briefly described the work of Chaudhuri and coworkers [16], who observed reversible stress stiffening followed by softening under compressional stress (Fig. 6.2). In their experiments, the controlled input was the amount of stress as applied by the AFM cantilever and the observable was the deformation (change in height) of the network. Our simulation method mirrors this setup. Using the constant-stress framework discussed in chapter 5, we control the amount of stress applied and measure the corresponding strain in the system.

In Fig. 6.12, we plotted the applied stress against the measured strain for several network realizations. For each of the networks, the number of input filaments remained constant at 60. The parameter we tuned was the percentage of filaments with orientation drawn from an uniform or orientationally biased Gaussian distribution (detailed in Sec. 6.2.2). For the results shown, the percentage of filament orientation drawn from a Gaussian distribution was set at 0%, 40%, and 80%. Five different statistical realizations of each case were examined.

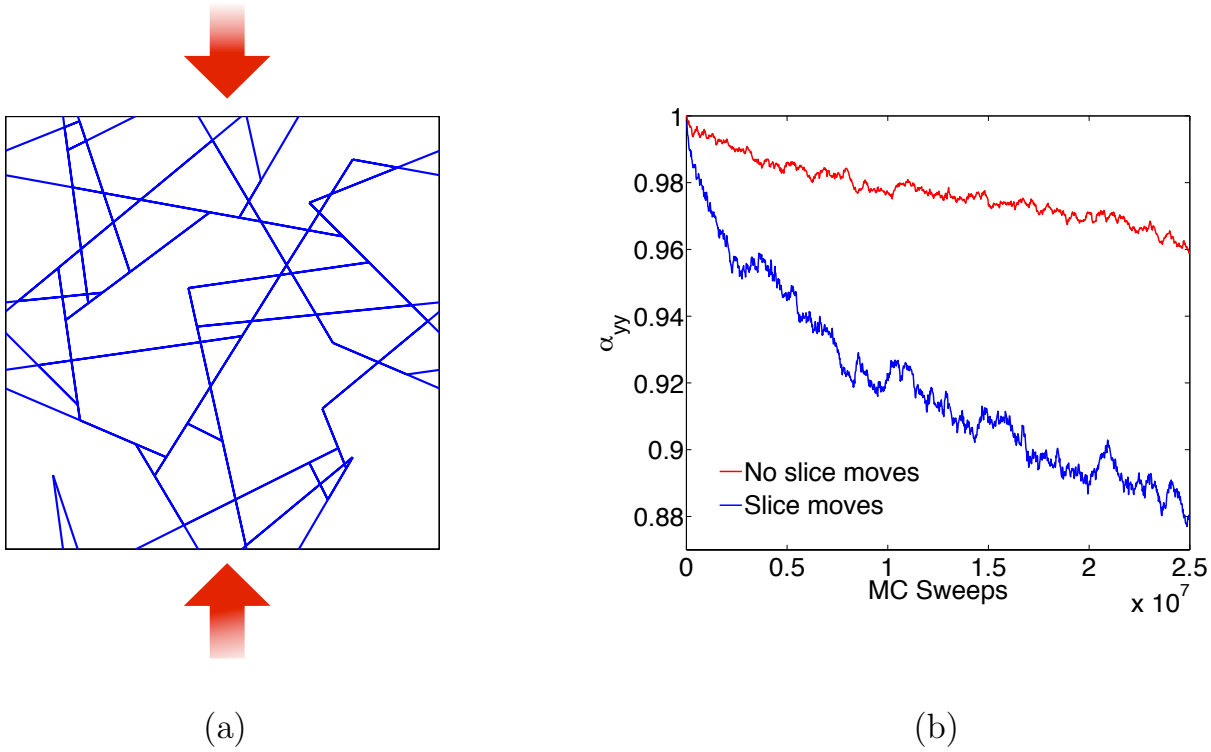

(a) (b)

Figure 6.11: **Application of slice moves.** (a) The simulated network, in which compressive stress was applied in the vertical (y) direction. (b) Comparison of strain component α_{yy} under applied stress in the y direction, with and without slice moves.

Across all network parameter regimes, we observed a linearly elastic regime followed by stress softening (Fig. 6.12). At a certain point after the softening starts to occur, the network collapses due to filament buckling. In general, network softening occurs at 5–10% network strain, although it can occur as low as 2.5% strain. In addition, for each group of similarly oriented networks, we observed a wide range of linear elastic modulus as well as applied stress values where the network softens and ultimately collapses.

6.3.3 Crosslinking potential

The elasticity of the constituent filaments are not the only contributors to the mechanical properties of an actin network. Studies of actin networks with a single type of crosslinker have found that both the type as well as the concentration of the crosslinker can dramatically affect the rheological properties and stiffness of the network. For example, actin networks with a very strong crosslinker (biotin/avidin) behave like a solid while networks with a weak crosslinker (amoeba α-actinin) exhibit viscoelastic properties [130]. Additionally, varying the crosslinker concentration can change the elastic modulus up to 1000–fold [41].

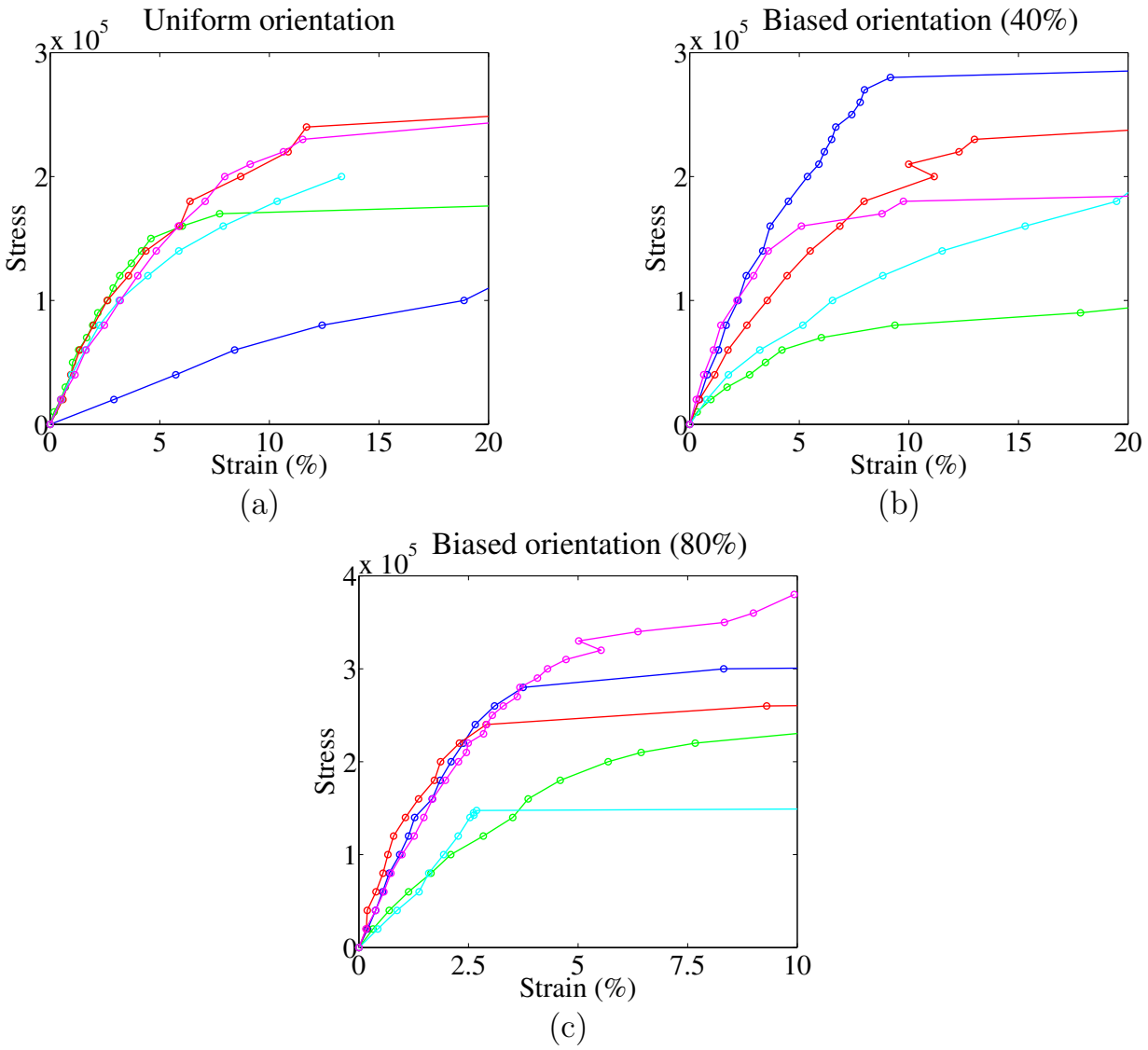

Figure 6.12: **Stress softening under compression.** Under network compression, we observed a linear regime followed by stress softening. The varied parameter was the percentage of filament orientation drawn from a orientationally biased Gaussian distribution. This parameter was set at (a) 0%, (b) 40%, and (c) 80%. The rest of the filament orientations were drawn from a uniform distribution. Five different statistical realizations (differently colored curves) of each case were examined.

Filamin, the cytoskeletal crosslinker whose steric effects have been included in the model, possesses elastic properties of its own. It can be modeled as a WLC, with a persistence length of 14 nm ($l_p = 22$ nm for each subunit) [49]. Using the variance in the angle between crosslinked actin filaments, found to be $(15.5°)^2$, Hartemink calculated the rotational stiffness of filamin to be 0.6×10^{-19} N·m [49].

However, in our network model, filaments are able to freely rotate around a crosslink. The only constraint is that filaments are attached at the point of the crosslink. To approximate the effects of filamin's rotational stiffness, we added a harmonic potential at each crosslink,

$$U_c(\theta) = k_c(\theta - \theta_{eq})^2, \tag{6.5}$$

where θ_{eq} is the junction angle in the network without stress (reference configuration). The total system energy is then composed of the filament energy and crosslinking potential.

A variety of spring constants for the harmonic potential were tested and the results are shown in Fig. 6.13. Although the linear elastic modulus increased as a function of increasing spring constant, the overall stress-strain behavior of the networks did not qualitatively change. They still exhibit the softening behavior observed without the added harmonic potential. The increase in the elastic modulus for the linear regime with an increasing spring constant is expected. As force is applied to the networks, the filaments are strained from their original positions. During this process, some junction angles shift away from their reference configuration angle distribution in order to accommodate the new positions. The higher the spring constant associated with the junction angle, the more a network is able to resist the applied stress, resulting in a higher compression modulus in the linear region. The strain values at which softening and network collapse occurs remain similar for varying values of the spring constant.

6.3.4 A single filament perspective on compressed actin networks

One advantage of modeling and simulation is that we are often able to probe small length scale properties and distributions that are very difficult to access experimentally. Thus far, we have been subjecting networks to compressional stress and measuring the corresponding bulk compressional modulus. We aim to understand how stress changes properties at the single filament level and correspondingly, whether we can utilize the single filament behavior to explain the bulk elastic response.

Fig. 6.14 shows a single filament view into networks under compression. A network was subjected to increasing compression. For each stress, the fluctuations of segment lengths were recorded. Those lengths were then divided by the corresponding segment lengths in the reference configuration and the resulting scaled distributions were plotted. In the figure, three such strain/stress states are shown. The blue line represents the filament length distribution in the reference configuration ($\gamma_{network} = 0\%$). Under moderate stress (red curve, $\gamma_{network} = 7\%$), the majority of segments still fluctuated around their non-stress equilibrium states. However, a small crop of segments were significantly bent, resulting in a bimodal

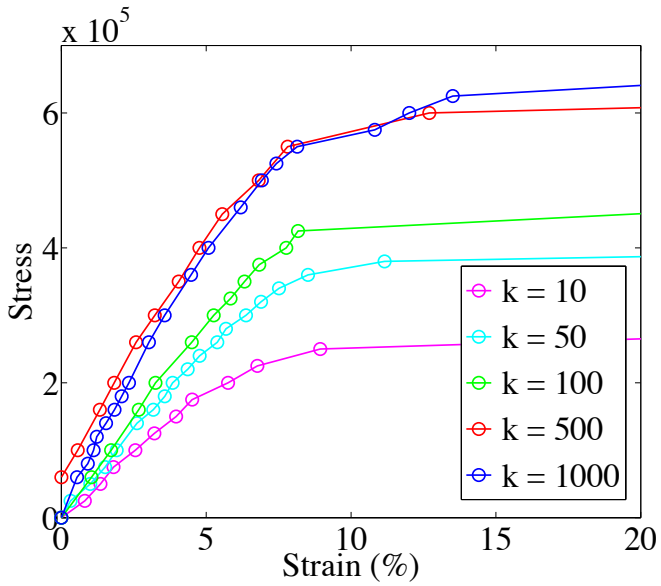

Figure 6.13: **Crosslinking potential.** In order to approximate the effects of a crosslinker with a rotational stiffness, we added a harmonic potential at each crosslink (Eq. 6.5). Various spring constants (k) were tested. Although the linear elastic modulus increased as a function of increasing spring constant, stress softening was observed in all cases.

distribution. Under high stress (green curve, $\gamma_{network} = 29\%$), this crop of bent segments grew. But surprisingly, the majority of segments still fluctuated around their unstressed length distributions. This qualitative picture was seen with all the networks tested.

In general, an increasing proportion of bent segments was observed with greater network compression. However, there is little evidence of stretched filaments, supporting the observation of stress softening at the network level.

6.3.5 Normal mode analysis

Even for the same set of input parameters (number of filaments, box size, filament length, percentage of orientationally biased filaments), the elastic moduli in the linear region varied significantly (Fig. 6.12). In some cases, the linear elastic modulus for the stiffest network in the group is approximately 5 times higher than that of the softest network (Fig. 6.15).

We examined the reasons for such large variations in the network elasticity using normal mode analysis. The normal modes reveal the collective motions of the network constituents. Thus, we hypothesize that the relative number or proportion of low frequency (soft) modes may potentially provide insights into the network elasticity in the linear region.

To calculate the normal modes, it is necessary to obtain a network structure corresponding to a local energy minimum because fundamentally, normal modes describe harmonic motions about an energy minimum [51]. Although the potential dictating the chain configurations

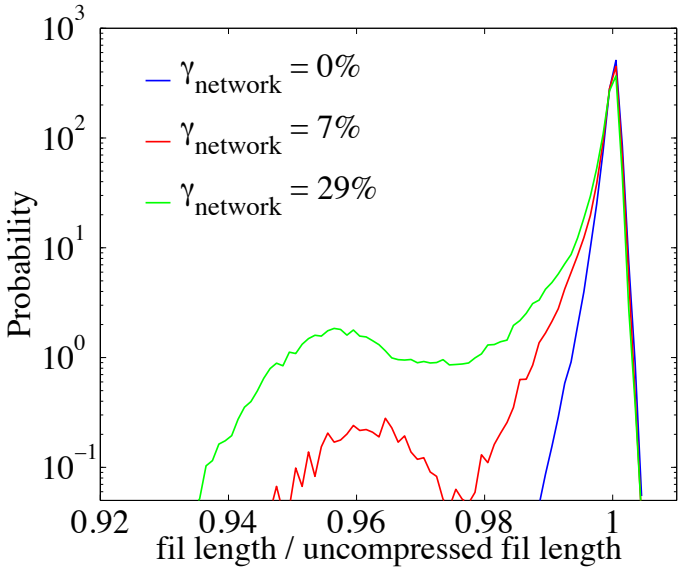

Figure 6.14: **Single filament length distributions.** As more stress was applied to a network, the corresponding changes in the distributions of single segment lengths were monitored. In general, with greater network deformation, the majority of segments stilled fluctuated around their non-stress equilibrium lengths while a small proportion of filaments were significantly bent, resulting in a bimodal distribution.

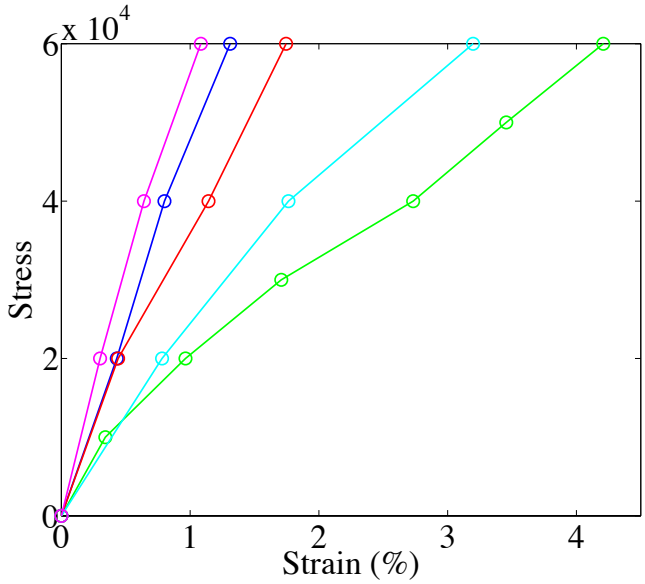

Figure 6.15: **Elasticity in the linear regime.** The results shown are for the linearly elastic region of Fig. 6.12b. For the same set of input parameters, there is a large variation in the linear elastic modulus.

is anharmonic (Fig. 6.5b), its behavior about a minimum can be approximated using a harmonic potential. To find a conformation corresponding to such an energetic state, a Monte Carlo simulated annealing procedure was used to slowly cool the network into a local minimum. This was followed by the calculation of the Hessian matrix H, a matrix of mixed second derivatives of the energy with respect to the particle coordinates,

$$H = \begin{pmatrix} \dfrac{\partial^2 f}{\partial x_1^2} & \dfrac{\partial^2 f}{\partial x_1\,\partial x_2} & \cdots & \dfrac{\partial^2 f}{\partial x_1\,\partial y_N} \\ \dfrac{\partial^2 f}{\partial x_2\,\partial x_1} & \dfrac{\partial^2 f}{x_1^2} & \cdots & \dfrac{\partial^2 f}{\partial x_2\,\partial y_N} \\ \vdots & \vdots & \ddots & \vdots \\ \dfrac{\partial^2 f}{\partial y_N\,\partial x_1} & \dfrac{\partial^2 f}{\partial y_N\,\partial x_2} & \cdots & \dfrac{\partial^2 f}{\partial y_N^2} \end{pmatrix}. \tag{6.6}$$

Differentiation was performed using finite differences, since the model potential is not easily differentiable.

Finally, the Hessian was diagonalized to obtain a list of eigenvectors and eigenvalues that defines the normal modes. Since the actin networks are two-dimensional, there are $2N$ eigenvectors and eigenvalues, where N is the number of crosslinks in our network. By definition,

$$H\eta_i = \omega_i^2 \eta_i \tag{6.7}$$

where η_i is the i^{th} eigenvector and ω_i^2 is the i^{th} eigenvalue. In this equation, ω is also the angular frequency [51]. Each eigenvector represents the magnitudes and directions for all particle motions and the corresponding eigenvalues are their frequencies.

Identifying network soft regions

In general, the low-frequency modes describe collective system motions while the higher frequency modes describe more localized motion. By visualizing the low-frequency normal modes, we can gain insights into the soft regions in the networks. Fig. 6.16 shows a reference configuration network structure and the first four non-translational normal mode displacements corresponding to the network. It is apparent from visualizing the displacement vectors that most of the motion corresponds to the region on the right side of the network. Compared to other network regions, this region is relatively soft and susceptible to deformation.

Comparing network normal modes

Although visualizing normal mode displacement vectors can be useful for identifying soft regions in the networks, we aim to predict relative network stiffness from the normal modes.

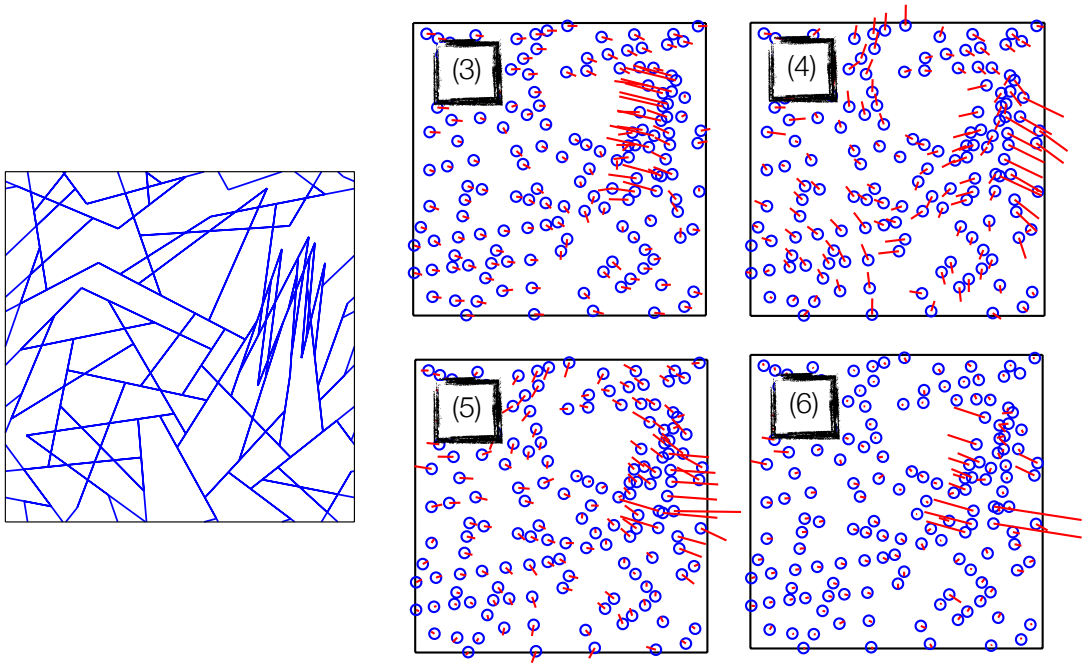

Figure 6.16: **Visualizing low-frequency normal modes.** Network structure (left) and the first four non-translational normal mode displacements corresponding to the network (right). The index starts at four because first two modes are translational modes.

And since low-frequency modes correspond to collective motions which are ultimately responsible for the network conformational changes under stress, we hypothesize that directly comparing these soft modes might provide insights into relative network stiffnesses. Fig. 6.17 shows the square of the angular frequencies (ω^2) for the first 50 normal modes corresponding to the 5 networks in Fig. 6.15 (using the same color scheme). Previously, it has been shown that the networks in cyan and green are the softest networks, followed by red, and the blue and magenta networks are the stiffest in the group. In Fig. 6.17, the frequencies for the green network are consistently lower than those of other networks for the corresponding index. The network denoted by the color cyan shows similar normal mode frequencies for approximately the first 20 normal modes. Frequencies for networks corresponding to magenta, blue, and red are distinguishable from green and cyan (the softest networks), but are more difficult to distinguish from each other. Therefore, although it is possible to loosely correlate the relative frequencies of the low-frequency normal modes to the network strength, the ability to make accurate predictions for networks with similar linear elastic moduli is not yet achieved.

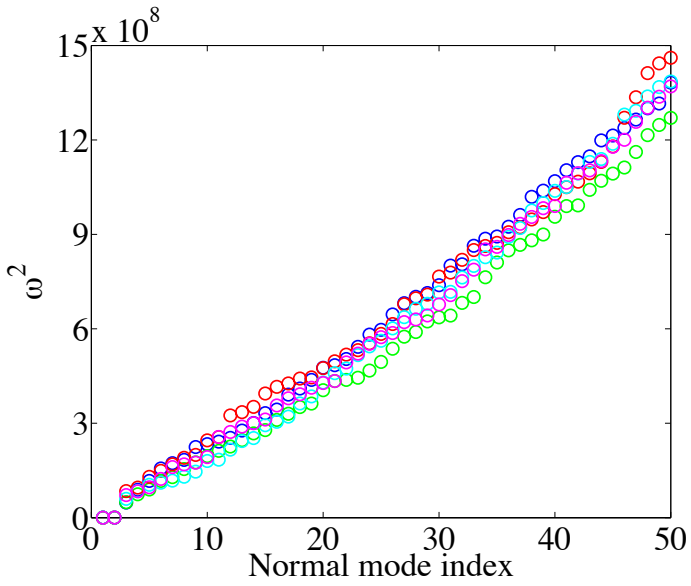

Figure 6.17: **Comparison of normal mode frequencies in different networks.** Square of the angular frequencies (ω^2) against the normal mode index for the first 50 normal modes corresponding to the networks in Fig. 6.15 (using the same color scheme).

6.4 Conclusions

In this work, we utilized our previously developed constant stress method and a coarse-grained model for short, semiflexible chains to gain insight into the elastic properties of actin networks under compression. Under compressional stress, we consistently observed a linearly elastic regime followed by stress softening in the networks, without any evidence of stiffening. We analyzed the softening response using a single filament perspective, in which we detected more filament bending as a function of increasing compressional stress, resulting in a bimodal distribution of filament lengths. Our results suggest the possibility that the reversible stress stiffening and softening seen by Chaudhuri et al. [16] might arise from the interaction of actin with a host of other ABPs, and thus the elastic responses are not directly comparable. We also analyzed the elastic responses using normal mode analysis, from which we can identify network soft regions and obtain a rough estimate of the relative elastic moduli among different networks in the linearly elastic regime. Our findings can motivate and aid the interpretation of new experiments using a minimal set of proteins to further shed light on the elastic behavior of actin networks under compression.

Bibliography

[1] V. Abraham, V. Krishnamurthi, D. Taylor, and F. Lanni. The actin-based nanomachine at the leading edge of migrating cells. *Biophys. J.*, 77:1721–1732, 1999.

[2] B. Alberts, A. Johnson, J. Lewis, M. Raff, K. Roberts, and P. Walter. *Molecular Biology of the Cell, Fifth Edition.* Garland Science, New York, 2008.

[3] B. Antonny. Mechaisms of membrane curvature sensing. *Annu. Rev. Biochem.*, 80:101–123, 2011.

[4] N. Balaban, U. Schwarz, D. Riveline, P. Goichberg, G. Tzur, I. Sabanay, D. Mahalu, S. Safran, A. Bershadsky, L. Addadi, and B. Geiger. Force and focal adhesion assembly: a close relationship studied using elastic micropatterned substrates. *Nat. Cell Biol.*, 3:466–472, 2001.

[5] E. Batchelder, G. Hollopeter, C. Campillo, X. Mezanges, E. Jorgensen, P. Nassoy, P. Sens, and J. Plastino. Membrane tension regulates motility by controlling lamellipodium organization. *Proc. Natl. Acad. Sci.*, 108:11429–11434, 2011.

[6] T. Baumgart, B. Capraro, C. Zhu, and S. Das. Thermodynamics and mechanics of membrane curvature generation and sensing by proteins and lipids. *Annu. Rev. Phys. Chem.*, 62:483–506, 2011.

[7] T. Belendez, C. Neipp, and A. Belendez. Large and small deflections of a cantilever beam. *Eur. J. Phys.*, 23:371–379, 2002.

[8] C. Beltzner and T. Pollard. Pathway of actin filament branch formation by Arp2/3 complex. *J. Biol. Chem.*, 283:7135–7144, 2008.

[9] A. Bicek, E. Tuzel, D. Kroll, and D. Odde. Analysis of microtubule curvature. *Methods Cell Biol.*, 83:237–268, 2007.

[10] J. Bigay, P. Gounon, S. Robineau, and B. Antonny. Lipid packing sensed by ArfGAP1 couples COPI coat disassembly to membrane bilayer curvature. *Nature*, 426:563–566, 2003.

[11] D. Boal. *Mechanics of the Cell.* Cambridge University Press, Cambridge, 2002.

[12] C. Broedersz, C. Storm, and F. MacKintosh. Nonlinear elasticity of composite networks of stiff biopolymers with flexible linkers. *Phys. Rev. Lett.*, 101:118103, 2008.

[13] C. Bustamante, S. Smith, J. Liphardt, and D. Smith. Single-molecule studies of DNA mechanics. *Curr. Opin. Struct. Biol.*, 10:279–285, 2000.

[14] A. Carlsson. Growth velocities of branched actin networks. *Biophys. J.*, 84:2907–2918, 2003.

[15] G. Charras. A short history of blebbing. *J. Microsc.*, 231:466–478, 2008.

[16] O. Chaudhuri, S. Parekh, and D. Fletcher. Reversible stress softening of actin networks. *Nature*, 445:295–298, 2007.

[17] J.-W. Chu and G. Voth. Coarse-Grained Modeling of the Actin Filament Derived from Atomistic-Scale Simulations. *Biophys. J.*, 90:1572–1582, 2006.

[18] E. Conti and F. MacKintosh. Cross-linked networks of stiff filaments exhibit negative normal stress. *Phys. Rev. Lett.*, 102:088102, 2009.

[19] L. Cramer, M. Siebert, and T. Mitchison. Identification of novel graded polarity actin filament bundles in locomoting heart fibroblasts: implications for the generation of motile force. *J. Cell Biol.*, 136:1287–1305, 1997.

[20] E. De La Cruz. Cofilin binding to muscle and non-muscle actin filaments: Isoform-dependent cooperative interactions. *J. Mol. Biol.*, 346:557–564, 2005.

[21] M. Deriu, A. Shkurti, G. Paciello, T. Bidone, U. Morbiducci, E. Ficarra, A. Audenino, and A. Acquaviva. Multiscale modeling of cellular actin filaments: From atomistic molecular to coarse-grained dynamics. *Proteins: Structure, Function, and Bioinformatics*, 80:1598–1609, 2012.

[22] A. Verkhovsky et al. Orientational order of the lamellipodial actin network as demonstrated in living motile cells. *Mol. Biol. Cell*, 14:4667–4675, 2003.

[23] I. Rouiller et al. The structural basis of actin filament branching by the Arp2/3 complex. *J. Cell Biol.*, 180:887–895, 2008.

[24] L. Blanchoin et al. Direct observation of dendritic actin filament networks nucleated by Arp2/3 complex and WASP/Scar proteins. *Nature*, 404:1007–1011, 2000.

[25] X. Xu et al. Three-dimensional reconstructions of Arp2/3 complex with bound nucleation promoting factors. *EMBO J.*, 31:236–247, 2011.

[26] Y. Arai et al. Tying a molecular knot with optical tweezers. *Nature*, 399:446–448, 1999.

[27] D. F. Evans and H. Wennerström. *The Colloidal Domain: Where Physics, Chemistry, Biology, and Technology Meet*. Wiley-VCH, New York, 2 edition, 1999.

[28] J. Fan, M. Saunders, and G. Voth. Coarse-Graining Provides Insights on the Essential Nature of Heterogeneity in Actin Filaments. *Biophys. J.*, 103:1334–1342, 2012.

[29] D. Farge. Mechanotransduction in development. *Curr. Top. Dev. Biol.*, 95:243–265, 2011.

[30] J. Finer, R. Simmons, and J. Spudich. Single myosin molecule mechanics: piconewton forces and nanometre steps. *Nature*, 368:113–119, 2004.

[31] E. Firat-Karalar and M. Welch. New mechanisms and functions of actin nucleation. *Curr. Opin. Cell Biol.*, 23:4–13, 2011.

[32] D. Fletcher and R. Mullins. Cell mechanics and the cytoskeleton. *Nature*, 463:485–492, 2010.

[33] Daan Frenkel and Berend Smit. *Understanding Molecular Simulation*. Academic Press, London, second edition, 2002.

[34] E. Frey, J. Wilhelm K. Kroy, and E. Sackmann. Statistical mechanics of semiflexible polymers: theory and experiment. In G. Forgacs and D. Beysens, editors, *Dynamical Networks in Physics and Biology*. Springer Verlag, Berlin, 1998.

[35] E. Galkin, A. Orlova, N. Lukoyanova, W. Wriggers, and E. Egelman. Actin depolymerizing factor stabilizes an existing state of F-actin and can change the tilt of F-actin subunits. *J. Cell Biol.*, 153:75–86, 2001.

[36] V. Galkin, A. Orlova, and E. Egelman. Actin Filaments as Tension Sensors. *Current Biology*, 22:R96–R101, 2012.

[37] V. Galkin, A. Orlova, G. Schröder, and E. Egelman. Structural polymorphism in F-actin. *Nat. Struct. Mol. Biol.*, 17:1318–1323, 2010.

[38] V. Galkin, A. Orlova, D. Solodukhin, E. Reisler, G. Schröder, and E. Egelman. Remodeling of Actin Filaments by ADF/Cofilin Proteins. *Proc. Natl. Acad. Sci.*, 108:20568–20572, 2011.

[39] G. Gallo and P. Letourneau. Regulation of growth cone actin filaments by guidance cues. *J. Neurobio.*, 58:92–102, 2004.

[40] M. Gardel, K. Kasza, C. Brangwynne, J. Liu, and D. Weitz. "Response of Cytoskeletal Networks. Response of Cytoskeletal Networks. *Methods in Cell Biology*, 89:487–519, 2008.

[41] M. Gardel, J. Shin, F. MacKintosh, L. Mahadevan, P. Matsudaira, and D. Weitz. Elastic behavior of cross-linked and bundled actin networks. *Science*, 304:1301–1305, 2004.

[42] P. Giardini, D. Fletcher, and J. Theriot. Compression forces generated by actin comet tails on lipid vesicles. *PNAS*, 100:6493–6498, 2003.

[43] F. Gittes, B. Mickey, J. Nettleton, and J. Howard. Flexural rigidity of microtubules and actin filaments measured from thermal fluctuations in shape. *J. Cell Biol.*, 210:923–934, 1993.

[44] E. Goley, A. Rammonhan, E. Znameroski, E. Firat-Karalar, D. Sept, and M. Welch. An actin-filament-binding interface on the Arp2/3 complex is critical for nucleation and branch stability. *PNAS*, 107:8159–8164, 2009.

[45] E. Goley, S. Rodenbusch, A. Martin, and M. Welch. Critical conformational changes in the Arp2/3 complex are induced by nucleotide and nucleation promoting factor. *Mol. Cell*, 16:269–279, 2004.

[46] E. Goley and M. Welch. The Arp2/3 complex: an actin nucleator comes of age. *Nature Reviews Molec. Cell. Bio.*, 7:713–726, 2006.

[47] G. Gompper and D. Kroll. Random surface discretizations and the renormalization of the bending rigidity. *J. Phys. I France*, 6:1305–1320, 1996.

[48] E. Gouin, M. Welch, and P. Cossart. Actin-based motility of intracellular pathogens. *Curr. Opin. Microbiol*, 8:35–45, 2005.

[49] C. Hartemink. *The Cross-linking Mechanism of Filamin A in the Actin Cytoskeleton*. PhD thesis, MIT, 2005.

[50] K. Hayakawa, H. Tatsumi, and M. Sokabe. Actin filaments function as a tension sensor by tension-dependent binding of cofilin to the filament. *J. Cell Biol.*, 195:721–727, 2011.

[51] S. Hayward and B. de Groot. Normal modes and essential dynamics. In A. Kukol, editor, *Molecular Modeling of Proteins*, pages 89–106. Humana Press, 2008.

[52] J.-S. Ho and A. Baumbärtner. Simulations of fluid self-avoiding membranes. *Europhys. Lett.*, 12:295–300, 1990.

[53] B. Hoffman, C. Grashoff, and M. Schwartz. Dynamic molecular processes mediate cellular mechanotransduction. *Nature*, 475:316–323, 2011.

[54] E. Huisman, C. Storm, and G. Barkema. Monte Carlo study of multiply crosslinked semiflexible polymer networks. *Phys. Rev. E*, 78:051801, 2008.

[55] A. Huok, A. Jilkine, C. Mejean, R. Boltyanskiy, E. Dufresne, S. Angenent, S. Altschuler, L. Wu, and O. Weiner. Membrane Tension Maintains Cell Polarity by Confining Signals to the Leading Edge during Neutrophil Migration. *Cell*, 148:175–188, 2012.

[56] I. Ichetovkin, W. Grant, and J. Condeelis. Cofilin produces newly polymerized actin filaments that are preferred for dendritic nucleation by the Arp2/3 complex. *Curr. Biol.*, 12:79–84, 2002.

[57] H. Isambert, P. Venier, A. Maggs, A. Fattoum, R. Kassab, D. Pantaloni, and M. Carlier. Flexibility of actin filaments derived from thermal fluctuations. Effect of bound nucleotide, phalloidin, and muscle regulatory proteins. *J. Biol. Chem.*, 270:11437–11444, 1995.

[58] P. Janmey and C. McCulloch. Cell mechanics: Integrating cell responses to mechanical stimuli. *Annu. Rev. Biomed. Eng.*, 9:1–34, 2007.

[59] H. Kang, Q. Wen, P. Janmey, J. Tang, E. Conti, and F. MacKintosh. Nonlinear elasticity of stiff filament networks: strain stiffening, negative normal stress, and filament alignment in fibrin gels. *J. Phys. Chem. B*, 113:3799–3805, 2009.

[60] J. Kas, H. Strey, J. Tang, D. Finger, R. Ezzell, E. Sackman, , and P. Janmey. F-Actin, a Model Polymer for Semiflexible Chains in Dilute, Semidilute, and Liquid Crystalline Solutions. *Biophys. J.*, 70:609–625, 1996.

[61] K. Kasza, G. Koenderink, Y. Lin, C. Broedersz, W. Messner, F. Nakamura, T. Stossel, F. MacKintosh, and D. Weitz. Nonlinear elasticity of stiff biopolymers connected by flexible linkers. *Phys. Rev. E*, 79:041928, 2009.

[62] T. Kim, W. Hwang, H. Lee, and R. Kamm. Computational analysis of viscoelastic properties of crosslinked actin networks. *PLoS Comput. Biol.*, 5:e1000439, 2009.

[63] H. Kojima, A. Ishijima, and T. Yanagida. Direct measurement of stiffness of single actin filaments with and without tropomyosin by in vitro nanomanipulation. *PNAS*, 91:12962–12966, 1994.

[64] O. Kratky and G. Porod. Röntgenuntersuchung gelöster fadenmoleküle. *Rec. Trav. Chim.*, 68:1106–1122, 1949.

[65] H. Kueh and T. Mitchison. Structural plasticity in actin and tubulin polymer dynamics. *Science*, 325:960–963, 2009.

[66] O. Lieleg, J. Kayser, G. Brambilla, L. Cipelletti, and A. Bausch. Slow dynamics and internal stress relaxation in bundled cytoskeletal networks. *Nat. Mater.*, 10:236–242, 2011.

[67] H. Lodish, A. Berk, S.L. Zipursky, P. Matsudaira, D. Baltimore, and J. Darnell. *Molecular Cell Biology*. W.H. Freeman Co., New York, 1999.

[68] S. Maciver, H. Zot, and T. Pollard. Characterization of actin filament severing by actophorin from Acanthamoeba castellani. *J. Cell Biol.*, 115:1611–1620, 1991.

[69] R. Mahaffy and T. Pollard. Kinetics of the formation and dissociation of actin filament branches mediated by Arp2/3 complex. *Biophys. J.*, 91:3519–3528, 2006.

[70] R. Mahaffy and T. Pollard. Influence of phalloidin on the formation of actin filament branches by Arp2/3 complex. *Biochemistry*, 47:6460–6467, 2008.

[71] Y. Marcy, J. Prost, M. Carlier, and C. Sykes. Forces generated during actin-based propulsion: A direct measurement by micromanipulation. *PNAS*, 101:5992–5997, 2004.

[72] J. Marko and E. Siggia. Stretching DNA. *Macromolecules*, 28:8759–8770, 1995.

[73] P. Mattila and P. Lappalainen. Filopodia: molecular architecture and cellular functions. *Nature Reviews Molec. Cell. Bio.*, 9:446–454, 2008.

[74] J. McCammon and S. Northrup. Gated binding of ligands to proteins. *Nature*, 293:316–317, 1981.

[75] B. McCullough, L. Blanchoin, J. Martiel, and E. Dela Cruz. Cofilin increases the bending flexibility of actin filaments: Implications for severing and cell mechanics. *J. Mol. Biol.*, 381:550–558, 2008.

[76] B. McCullough, E. Grintsevich, C. Chen, H. Kang, A. Hutchison, A. Henn, W. Cao, C. Suarez, J. Martiel, L. Blanchoin, E. Reisler, and E. De La Cruz. Cofilin-linked changes in actin filament flexibility promote severing. *Biophys. J.*, 101:151–159, 2011.

[77] A. McGough. F-actin-binding proteins. *Curr. Opin. Struct. Biol.*, 8:166–176, 1998.

[78] A. McGough, B. Pope, W. Chiu, and A. Weeds. Cofilin Changes the Twist of F-Action: Implications for Actin Filament Dynamics and Cellular Function. *J. Cell. Bio.*, 138:771–781, 1997.

[79] N. Metropolis, A. Rosenbluth, M. Rosenbluth, A. Teller, and E. Teller. Equation of state calculations by fast computing machines. *J. Chem. Phys.*, 21:1087–1092, 1953.

[80] A. Mogilner and L. Edelstein-Keshet. Regulation of actin dynamics in rapidly moving cells: A quantitative analysis. *Biophys. J.*, 83:1237–1258, 2002.

[81] N. Morone, T. Fujiwara, K. Murase, R. Kasai, H. Ike, S. Yuasa, J. Usukura, and A. Kusumi. Three-dimensional reconstruction of the membrane skeleton at the plasma membrane interface by electron tomography. *J. Cell Biol.*, 174:851–862, 2006.

[82] F. Nakamura, T. Stossel, and J. Hartwig. The filamins. *Cell Adh. Migr.*, 5:160–169, 2011.

[83] V. Okreglak and D. Drubin. Cofilin recruitment and function during actin-mediated endocytosis dictated by actin nucleotide state. *J. Cell Biol.*, 178:1251–1264, 2007.

[84] S. Padrick, L. Doolittle, C. Brautigam, D. King, and M. Rosen. Arp2/3 complex is bound and activated by two WASP proteins. *PNAS*, 108:E472–E479, 2011.

[85] S. Parekh, O. Chaudhuri, J. Theriot, and D. Fletcher. Loading history determines the velocity of actin-network growth. *Nat. Cell Biol.*, 7:1219–1223, 2005.

[86] M. Parrinello and A. Rahman. Crystal structure and pair potentials: a molecular dynamics study. *Phys. Rev. Lett.*, 45:1196–1199, 1980.

[87] M. Parrinello and A. Rahman. Strain fluctuations and elastic constants. *J. Chem. Phys.*, 76:2662–2666, 1982.

[88] B. Peter, H. Kent, I. Mills, Y. Vallis, P. Butler, P. Evans, and H. McMahon. BAR domains as sensors of membrane curvature: the amphiphysin BAR structure. *Science*, 303:495–499, 2004.

[89] J. Pfaendtner, E. Lyman, T. Pollard, and G. Voth. Structure and dynamics of the actin filament. *J. Mol. Biol.*, 396:252–263, 2010.

[90] J. Podolski and T. Steck. Length distribution of F-actin in Dictyostelium discoideum. *J. Biol. Chem.*, 265:1312–1318, 1990.

[91] T. Pollard. Rate Constants for the Reactions of ATP- and ADP-Actin with the Ends of Actin Filaments. *J. Cell. Bio.*, 103:2747–2754, 1986.

[92] T. Pollard. Regulation of actin filament assembly by Arp2/3 complex and formins. *Annu. Rev. Biophys. Biomol. Struct.*, 36:451–477, 2007.

[93] T. Pollard and G. Borisy. Cellular Motility Driven by Assembly and Disassembly of Actin Filaments. *Cell*, 112:453–465, 2003.

[94] T. Pollard and J. Cooper. Actin, a central player in cell shape and movement. *Science*, 326:1208–1212, 2009.

[95] M. Prass, K. Jacobson, A. Mogilner, and M. Radmacher. Direct measurement of the lamellipodial protrusive force in a migrating cell. *J. Cell Biol.*, 174:767–772, 2006.

[96] E. Prochniewicz, N. Janson, D. Thomas, and E. De La Cruz. Cofilin Increases the Torsional Flexibility and Dynamics of Actin Filaments. *J. Mol. Bio.*, 353:990–1000, 2005.

[97] S. Pronk and P. Geissler. Approximation for short semiflexible chains. Unpublished.

[98] S. Pronk and P. Geissler. Faster strain fluctuation methods through partial volume updates. *J. Chem. Phys.*, 130:194706 1–8, 2009.

[99] T. Pujol, O. du Roure, M. Fermigier, and J. Heuvingh. Impact of branching on the elasticity of actin networks. *PNAS*, 109:10364–10369, 2012.

[100] P. N. Pusey. Colloidal suspensions. In J.-P. Hansen, D. Levesque, and J. Zinn-Justin, editors, *Liquids, freezing and glass transition*, pages 763–942. Elsevier, Amsterdam, 1991.

[101] S. Rappaport, S. Medalion, and Y. Rabin. Curvature distribution of worm-like chains in two and three dimensions. *arXiv*, page 08013183, 2008.

[102] J. Ray and A. Rahman. Statistical ensembles and molecular dynamics studies of anisotropic solids. *J. Chem. Phys.*, 80:4423–4428, 1984.

[103] J. Ray and A. Rahman. Statistical ensembles and molecular dynamics studies of anisotropic solids. ii. *J. Chem. Phys.*, 82:4243–4247, 1985.

[104] E. Reisler and E. Egelman. Actin structure and function: What we still do not understand. *J. Biol. Chem.*, 282:36133–36137, 2007.

[105] V. Risca, E. Wang, O. Chaudhuri, J. Chia, P. Geissler, and D. Fletcher. Actin Filament Curvature Biases Branching Direction. *PNAS*, 109:2913–2918, 2012.

[106] M. Rubinstein and R. Colby. *Polymer Physics*. Oxford University Press, Oxford, 2003.

[107] G. Salbreux, G. Charras, and E. Paluch. Actin cortex mechanics and cellular morphogenesis. *Trends in Cell Biology*, 22:536–545, 2012.

[108] M. Saunders and G. Voth. Comparison between actin filament models: coarse-graining reveals essential differences. *Structure*, 20:641–653, 2012.

[109] S. Sharma, E. Grintsevich, M. Phillips, E. Reisler, and J. Gimzewski. Atomic force microscopy reveals drebrin induced remodeling of F-actin with subnanometer resolution. *Nano Lett.*, 11:825–827, 2011.

[110] T. Shimozawa and S. Ishiwata. Mechanical Distortion of Single Actin Filaments Induced by External Force: Detection by Fluorescence Imaging. *Biophys. J.*, 96:1036–1044, 2009.

[111] J. Small, C. Winkler, M. Vinzenz, and C. Schmeiser. Reply: Visualizing branched actin filaments in lamellipodia by electron tomography. *Nat. Cell Biol.*, 13:1013–1014, 2011.

[112] B. Smit, M. Kranenburg, M. Sperotto, and M. Venturoli. Mesoscopic simulations of biological membranes. In Ciccotti M. Ferrario, Giovanni and K. Binder, editors, *Computer Simulations in Condensed Matter Systems: From Materials to Chemical Biology Volume 2, Lecture Notes in Physics*, pages 259–286. Springer-Verlag Berlin Heidelberg, 2006.

[113] F. Soo and J. Theriot. Large-scale quantitative analysis of sources of variation in the actin polymerization-based movement of Listeria monocytogenes. *Biophys. J.*, 89:703–723, 2005.

[114] J. Stachowiak, E. Schmid, C. Ryan, H. Ann, D. Sasaki, M. Sherman, P. Geissler, D. Fletcher, and C. Hayden. Membrane bending by protein-protein crowding. *Nat. Cell. Bio.*, 14:944–949, 2012.

[115] D. Stokes and D. DeRosier. The Variable Twist of Actin and Its Modulation by Actin-binding Proteins. *J. Cell. Bio.*, 104:1005–1017, 1987.

[116] C. Storm, J. Pastore, F. MacKintosh, T. Lubensky, and P. Janmey. Nonlinear elasticity in biological gels. *Nature*, 435:191–194, 2005.

[117] F. Straub. Actin. *Stud. Inst. Med. Chem. Univ. Szeged. II*, pages 3–15, 1942.

[118] F. Straub. Actin, II. *Stud. Inst. Med. Chem. Univ. Szeged. II*, pages 23–37, 1943.

[119] T. Svitkina and G. Borisy. Arp2/3 complex and actin depolymerizing factor/cofilin in dendritic organization and treadmilling of actin filament array in lamellipodia. *J. Cell Biol.*, 145:1009–1026, 1999.

[120] A. Szent-Györgyi. The contraction of myosin threads. *Stud. Inst. Med. Chem. Univ. Szeged. I*, pages 17–26, 1943.

[121] J. Tan, J. Tien, D. Pirone, D. Gray, K. Bhadriraju, and C. Chen. Cells lying on a bed of microneedles: An approach to isolate mechanical force. *Proc. Natl. Acad. Sci.*, 100:1484–1489, 2003.

[122] S. Ti, C. Jurgenson, B. Nolen, and T. Pollard. Structural and biochemical characterization of two binding sites for nucleation-promoting factor WASp-VCA on Arp2/3 complex. *PNAS*, 108:E463–E471, 2011.

[123] S. Tojkander, G. Gateva, and P. Lappalainen. Actin stress fibers - assembly, dynamics and biological roles. *J. Cell Science*, 125:1855–1864, 2012.

[124] K. Tretiakov and K. Wojciechowski. Orientational phase transition between hexagonal solids in planar systems of hard cyclic pentamers and heptamers. *J. Phys. Cond. Matt.*, 14:1261–1273, 2002.

[125] Y. Tsuda, H. Yasutake, A. Ishijima, and T. Yanagida. Torsional rigidity of single actin filaments and actin-actin bond breaking force under torsion measured directly by in vitro micromanipulation. *PNAS*, 93:12937–12942, 1996.

[126] M. Ullner, G. Staikos, and D. Theodorou. Monte Carlo Simulations of a Single Polyelectrolyte in Solution: Activity Coefficients of the Simple Ions and Application to Viscosity Measurements. *Macromolecules*, 31:7921–7933, 1998.

[127] E. Urban, S. Jacob, M. Nemethova, G. Resch, and J. Small. Electron tomography reveals unbranched networks of actin filaments in lamellipodia. *Nat. Cell Biol.*, 12:429–435, 2010.

[128] T. Uyeda, Y. Iwadate, N. Umeki, A. Nagasaki, and S. Yumura. Stretching actin filaments within cells enhances their affinity for the myosin II motor domain. *PLoS One*, 6:1–12, 2011.

[129] V. Vogel and M. Sheetz. Local force and geometry sensing regulate cell functions. *Nat. Rev. Mol. Cell Biol.*, 7:265–275, 2006.

[130] D. Wachsstock, W. Schwarz, and T. Pollard. Cross-Linker Dynamics Determine the Mechanical Properties of Actin Gels. *Biophys. J.*, 66:801–809, 1994.

[131] D. Wallace. Thermoelasticity of stressed materials and comparison of various elastic constants. *Phys. Rev.*, 162:776–789, 1967.

[132] D. Wallace. Thermoelastic theory of stressed crystals and higher-order elastic constants. In H. Ehrenreich, F. Seitz, and D. Turnbull, editors, *Solid State Physics: Advances in Research and Applications*, pages 301–404. Academic Press, New York, 1970.

[133] M. Welch and R. Mullins. Cellular control of actin nucleation. *Annu. Rev. Cell Dev. Biol.*, 18:247–288, 2002.

[134] K. Wojciechowski and K. Tretiakov. Computer simulation of elastic properties of solids under pressure. *Comp. Phys. Comm.*, 121:528–530, 1999.

[135] M. Worring and A. Smeulders. Digital curvature estimation. *CVGIP Imag. Understan.*, 58:366–382, 1993.

[136] W. Zhang. If Actin only had a Brain: Developing Monte Carlo Simulations for Simple Actin Network Dynamics to Explore Complex Cell Motility. Master's thesis, University of California, Berkeley, 2008.

Appendix A

Appendix

A.1 Variables used in approximation for short semiflexible chains

The variables a, b, c, d previously used in Ch. 6, Eq. 6.4 are defined as follows:

$$a = -\ln\left[2\sqrt{d}K_1\left(2b^2\sqrt{d}\right)\right] \tag{A.1}$$

$$b = \left[\frac{1}{2\sqrt{d}}G\left(\frac{\sqrt{d}}{\langle z-c\rangle}\right)\right]^{1/2} \tag{A.2}$$

$$c = L^2\left(6.0\cdot 10^{-3} + 0.497432\,|\mathbf{R}|^2\right) \tag{A.3}$$

$$d = (c - z_{\max}). \tag{A.4}$$

In a, $K_1(x)$ is a modified Bessel function of the second kind.

In b,

$$G(k) \approx \frac{2}{3}(k-1) - \frac{1}{9}(k-1)^2 + \frac{1}{9}(k-1)^3 - \frac{23}{162}(k-1)^4 + \mathcal{O}[(k-1)^5] \tag{A.5}$$

and

$$\frac{1}{\langle z-c\rangle} = \frac{1}{\sqrt{d}}\frac{K_1\left(2b^2\sqrt{d}\right)}{K_2\left(2b^2\sqrt{d}\right)}, \tag{A.6}$$

where

$$\frac{K_2(x)}{K_1(x)} \approx 1 + \frac{3}{2}x^{-1} + \frac{3}{8}x^{-2} - \frac{3}{8}x^{-3} + \frac{63}{128}x^{-4} + \mathcal{O}(x^{-5}). \tag{A.7}$$

In d,

$$
\begin{aligned}
z_{\max} \;= \langle z \rangle - L^2 \Big[\;& 0.017980 && && +0.0013970 && |\mathbf{R}| && \\
& +0.010447 && |\mathbf{T}| && -0.0018700 && |\mathbf{T}|^2 && \\
& +0.00011252 && |\mathbf{T}|^3 && -0.0039224 && |\mathbf{R}|\,|\mathbf{T}| && \\
& +0.00070242 && |\mathbf{R}|^2\,|\mathbf{T}| && +0.00074855 && |\mathbf{R}|\,|\mathbf{T}|^2 && \\
& -1.4741 \cdot 10^{-4} && |\mathbf{R}|^2\,|\mathbf{T}|^2 && +0.0031051 && (\mathbf{R}\cdot\mathbf{T}) && \\
& -9.3484 \cdot 10^{-4} && |\mathbf{R}|\,(\mathbf{R}\cdot\mathbf{T}) && -5.1088 \cdot 10^{-4} && |\mathbf{T}|\,(\mathbf{R}\cdot\mathbf{T}) && \\
& +0.00016520 && |\mathbf{R}|\,|\mathbf{T}|\,(\mathbf{R}\cdot\mathbf{T}) \Big], &&
\end{aligned}
\tag{A.8}
$$

where

$$
\begin{aligned}
\langle z \rangle \;= L^2 \Big[\;& 0.063774 && && +0.0020034 && |\mathbf{R}| && \\
& +0.60537 && |\mathbf{R}|^2 && +0.0075152 && |\mathbf{R}|^3 && \\
& +0.0055939 && |\mathbf{T}| && +0.062203 && |\mathbf{T}|^2 && \\
& +0.0028756 && |\mathbf{T}|^3 && -0.012364 && |\mathbf{R}|\,|\mathbf{T}| && \\
& +0.0092160 && |\mathbf{R}|^2\,|\mathbf{T}| && +0.00090847 && |\mathbf{R}|\,|\mathbf{T}|^2 && \\
& -7.2895 \cdot 10^{-4} && |\mathbf{R}|^2\,|\mathbf{T}|^2 && -0.10962 && (\mathbf{R}\cdot\mathbf{T}) && \\
& -0.0030577 && |\mathbf{R}|\,(\mathbf{R}\cdot\mathbf{T}) && -1.5964 \cdot 10^{-4} && |\mathbf{R}|\,|\mathbf{T}|\,(\mathbf{R}\cdot\mathbf{T}) && \\
& -1.2347 \cdot 10^{-4} && (\mathbf{R}\cdot\mathbf{T})^2 \Big]. &&
\end{aligned}
\tag{A.9}
$$